Toyama Prefectural University

Department of Intelligent Systems Design Engineering

Fabrication of Grain-oriented Lead-free Piezoceramics

Yao Lu

September 2017

ABSTRACT

Potassium sodium niobate (KNN) based piezoelectric materials system is deemed as one of the most promising candidates for substitution of lead-based piezoelectric materials due to the high piezoelectric coefficient and high Curie temperature. However, their piezoelectric properties are still lower than the lead-based piezoelectric materials. Improving the performance of KNN-based piezoelectric ceramics has become a need for development.

The main research in this thesis can be divided into three parts. First of all, BZ–KNLN–BNT tertiary system piezoceramic with high performance-temperature stability was developed by adjusting the MPB slope (chapter 3). Moreover, $NaNbO_3$ template particles using for preparing the oriented ceramics were synthesized by the hydrothermal method instead of the traditional high temperature molten salt method (chapter 4, 5). Finally, oriented KNLN–BZ–BNT ceramics were fabricated by using the Reactive Templated Grain Growth (RTGG) method (chapter 6).

For the study of KNN-based ceramics component, rhombohedral perovskite component BNT was employed as the third component to adjust the MPB slope of BZ-KNN system. MPB slope of KNLN–BZ system was adjusted from negative to positive by adding a small amount of the third component-BNT. A vertical MPB was formed when the addition amount of BNT was 1%. The vertical MPB composition, 0.075BZ–0.915KNLN–0.01BNT, with temperature-independent behavior has important practical value. The research method, using a stable rhombohedral perovskite component to adjust the negative MPB slope, indicates the possibility that the positive slope of MPBs could be made perpendicular to the composition axis by adding a stable tetragonal perovskite component as the third component in lead-free piezoceramic systems. The method provides a route for improving the performance with temperature stability of lead-free piezoceramics.

In the synthesis of template particles by hydrothermal method, $NaNbO_3$ particles

with different morphology were synthesized. Plate-like morphology particles with a width of 35 μm and a thickness of 3 μm and fibrous morphology particles with an aspect ratio were obtained as expected morphology. Through investigating the hydrothermal conditions such as reaction time, temperature and NaOH concentration on the phase and morphology of the particles, process of crystal growth was conjectured. The plate-like $NaNbO_3$ particles were grown form the strip-like $Na_8Nb_6O_{19} \cdot 13H_2O$ through dehydration and rearrangement with the increase of temperature. The optimal hydrothermal conditions for preparing plate-like morphology were confirmed as 140 ^oC, 3 h and 12 mol/L of NaOH. Fibers NN particles with an aspect ratio could be obtained with further increase of temperature to 180^oC. After annealing treatment at 600^oC, the plate-like NN and fiber NN both turned into perovskite structure without morphology change. However, the melting point of the plate-like particles confirmed by TG-DTA analysis was around 1000 ^oC, therefore the particles could only be used in low temperature sintering below 1000 ^oC.

To improve the application temperature of template particles, hexagonal $NaNbO_3$ particles with plate-like morphology were synthesized by hydrothermal method. The morphological evolution of the solid products in the reaction with the increase of mineralizer concentration is monitored via SEM: the initial plate-like particles grew rapidly and finally transformed into cubic morphology. The mineralizer concentration for synthesis of hexagonal $NaNbO_3$ particles was confirmed by XRD. Under such concentration, the size of particles can be controlled. The particles were transformed from ilmenite structure to perovskite structure after annealing. The plate-like morphology was kept with a little crack on the surface. Therefore, the surface orientation of the perovskite particles was microcosmically and macroscopically characterized by EBSD and XRD analysis respectively. The results indicate that thinner particles tend to have higher orientation in (00l) crystal planes.

In the fabrication of oriented KNLN–BZ–BNT ceramics by tape-casting method, slurry formulations suitable for this system was studied, and high quality tape-casting thick films were obtained. The process of the preparation of oriented ceramics was optimized. On this basis, oriented KNLN–BZ–BNT ceramics with an orientation of 49%

were fabricated. The d_{33} of oriented ceramics improved 22% compared with non-oriented ceramics. The principle of orient development process was also investigated and it can be divided into 3 stages: (1) ceramics densification followed with in situ reaction between template particles and matrix particles; (2) rapid growth of individual oriented grain; (3) slow growth of oriented grain. The results showed that the oriented grain growth follow the principle of 2-D nucleation and growth.

Contents

Chapter 1

Introduction

1.1 Principles of Piezoelectricity

1.1.1 The Direct and the Converse Piezoelectric Effect

Piezoelectricity is linear interaction between mechanical and electrical systems in non-centric crystals or similar structures. The direct piezoelectric effect may be defined as the change of electric polarization proportional to the strain. A material is said to be piezoelectric if the application of an external mechanical stress gives rise to dielectric displacement in this material. This displacement manifests itself as internal electric polarization. It should be noted that the piezoelectric effect strongly depends on the symmetry of the crystal. A crystal having sufficiently low symmetry produces electric polarization under the influence of external mechanical force. Crystals belonging to the 11 point groups having central symmetry are unable to produce piezoelectric effect. With one exception, all classes devoid of a centre of symmetry are piezoelectric. The single exception is the Class 29 (enantiomorphous hemihedral), which, although without a centre of symmetry, nevertheless has other symmetry elements that combine to exclude the piezoelectric property. Closely related is the converse (reciprocal, inverse) effect, whereby a piezoelectric crystal becomes strained if an external electric field is applied [1].

We subject a plate to a pressure parallel with the thickness. If a compressional force (size) F is used, the polarization P_1 parallel to the thickness is proportional to the stress $T_{11} = F/A$. Hence the piezoelectric polarization charge on electrodes covering the major faces A is proportional to the force causing the strain. If we apply tension, the sign of pressure is reversed and the sign of the electric polarization reverses too. When an electric field E is applied along the thickness, the plate is deformed. The deformation (the strain S_{11}) changes sign when the polarity of the field is reversed (Fig. 1-1).
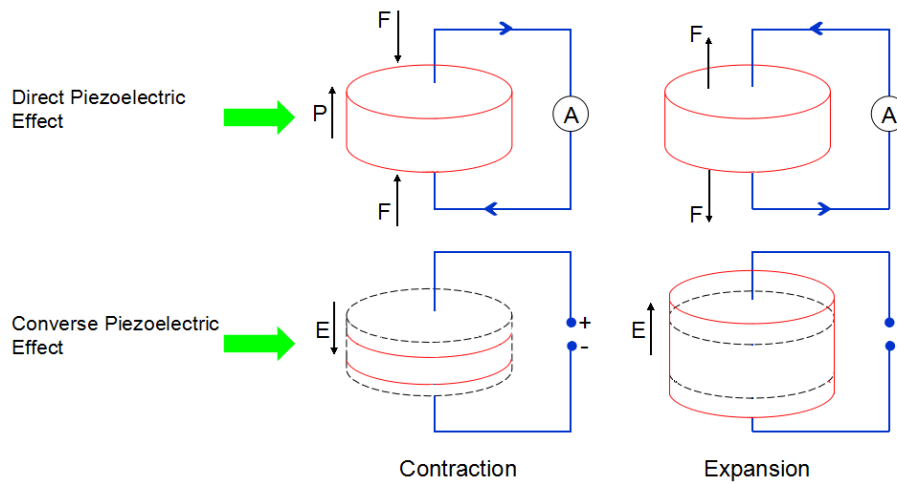
Fig. 1-1 Direct and converse piezoelectric effect

The direct piezoelectric effect is described by

$$P_1 = d_{111}T_{11}, \tag{1.1}$$

where P_1 is the component of the polarization vector and T_{11} is the component of the stress tensor. The coefficient d_{111} is called the piezoelectric coefficient. Conversely, if an external electric field E_1 is applied, a strain S_{11} is produced

$$S_{11} = d_{111}E_1. \tag{1.2}$$

1.1.2 History of the Theory of Piezoelectricity

The direct piezoelectric effect was first discovered by the brothers Pierre Curie and Jacques Curie more than a century ago [2]. They found out that when a mechanical stress was applied to crystals such as tourmaline, topaz, quartz, Rochelle salt and cane sugar, electrical charges appeared, and this voltage was proportional to the stress.

The Curies did not, however, predict that crystals exhibiting the direct piezoelectric effect would also exhibit the converse piezoelectric effect. One year later that property was theoretically predicted on the basis of thermodynamic consideration by Lippmann [3], who proposed that converse effects must exist for piezoelectricity, pyroelectricity, *etc*.

Subsequently, the inverse piezoelectric effect was confirmed experimentally by

2

Curies [4], who proceeded to obtain quantitative proof of the complete reversibility of electromechanical deformations in piezoelectric crystals. These events above can be viewed as the beginning of the history of piezoelectricity.

Based on them, Woldemar Voigt [5] developed the first complete and rigorous formulation of piezoelectricity in 1890. Since then several books on the phenomenon and theory of piezoelectricity have been published. Cady [6] treated the physical properties of piezoelectric crystals as well as their practical applications, Tiersten [7] dealt with the linear equations of vibrations in piezoelectric materials, and Kudryavtsev [8], Ikeda [9] , gave a more detailed description of the physical properties of piezoelectricity. Rogacheva [10] presented general theories of piezoelectric shells. Qin [11,12] discussed Green's functions and fracture mechanics of piezoelectric materials. Micromechanics of piezoelectricity were discussed in references [13].

1.2 Applications of Piezoelectricity

Piezoelectric materials are used in sensors, transducer, resonators, filters, generator, underwater acoustic devices, fish-finders and diagnostic acoustic devices. Figure 1-2 shows a summarized outline of technical applications of piezoelectricity.
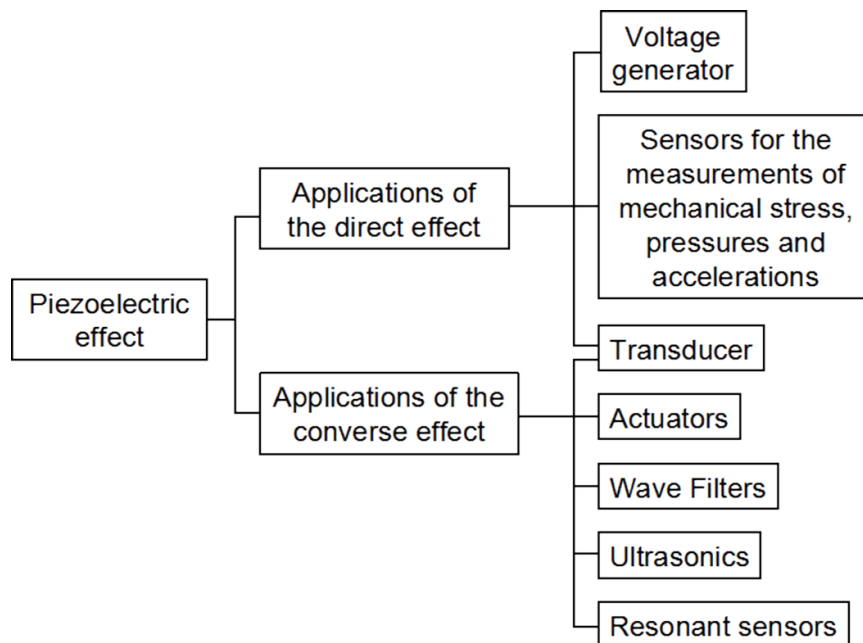
Fig. 1-2 Technical applications of piezoelectricity

In particular, piezoelectric films have been used as sensors [14,15], speakers for audio equipment [16-18], and printing [19,20] applications. Piezoelectric ceramic transducers have been applied to adaptive structures for vibration control [21], ultrasonic flaw detection [22] and military systems, such as launch vehicles, aircraft, and submarines. The piezoelectric single crystal material such as quartz could be made in to quartz crystal resonators [23] and applied to communication equipment and timer. Lead magnesium niobate-lead titanate (PMNT) [24,25] could be used as medical ultrasound imaging probe in medical fields.

It is noteworthy that most of widely used piezoelectric materials are lead-based materials. However, due to toxicity and pollution of Pb element, the Restriction of hazardous substances directive (RoHS) [26] which was adopted in February 2003 by the European Union greatly limited the application of lead-based piezoelectric ceramics. Therefore, it is necessary to develop the lead-free based piezoelectric materials.

1.3 Classification of Lead-free Piezoelectric Ceramics by Structure

1.3.1 Perovskite structure

The perovskite structure is adopted by many oxides that have the chemical formula ABO_3. The structure of an ideal cubic perovskite is shown in Fig. 1-3, where the A cation are shown at the corners of the cube, and the B cation in the centre with oxygen ions in the face-centred positions.
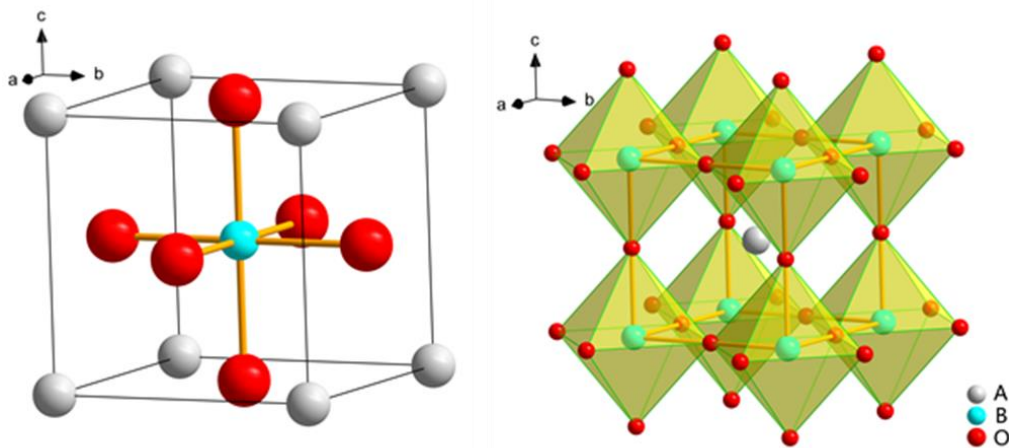
Fig. 1-3 Cubic perovskite unit cell. Blue spheres represent the A cations, white spheres represent the B cations, and red spheres represent oxygen anions forming an octahedra.

There are many perovskite structure-based piezoelectric ceramics, such as $BaTiO_3$ (BT), $Na_{0.5}Bi_{0.5}TiO_3$ (BNT) and $K_xNa_{1-x}NbO_3$ (KNN), each of them has its unique properties. Although their performance are still lower than PZT as shown in Fig. 1-4, they are still the most promising lead-free piezoelectric ceramics.
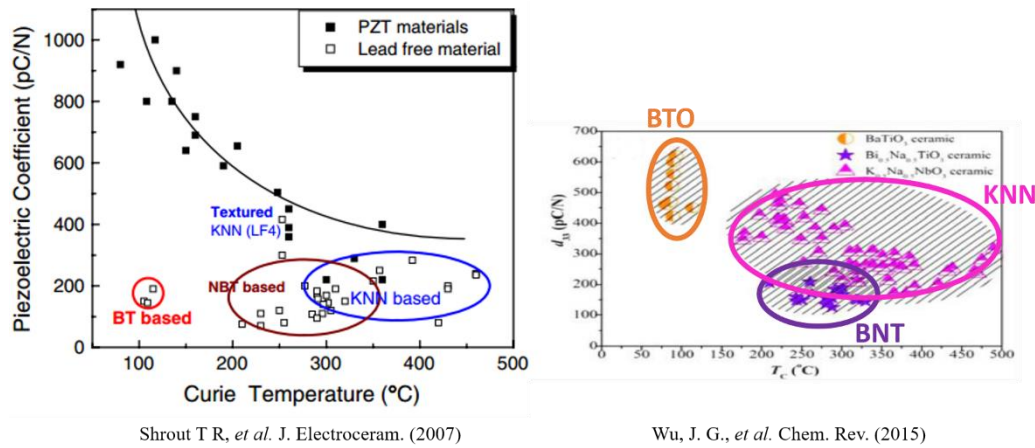
Fig. 1-4 Room temperature values of d_{33} as a function of T_c for various piezoceramics with perovskite structure and PZT.

1.3.1.1 Barium titanate

Barium titanate is the first discovered ferroelectric perovskite. Its ferroelectric properties are connected with a series of three structural phase transitions. The Curie point T_c, of barium titanate is 120 °C. Above 120 °C the original cubic cell is stable up to 1460 °C. Above this temperature a hexagonal structure is stable. When the temperature is below the Curie point, crystallographic changes in BaTiO$_3$ occur, first at about 120 °C a ferroelectric transition between the cubic, paraelectric and ferroelectric phase of tetragonal structure takes place. At 5 °C, the transition to a phase of the orthorhombic structure goes on and at -90 °C to the low temperature phase having a trigonal structure [27].

1.3.1.2 Sodium bismuth titanate

Sodium bismuth titanate, Na$_{0.5}$Bi$_{0.5}$TiO$_3$ (BNT), as rhombohedral symmetry (R3C) at room temperature (RT) and their phase transitions are complicated. The phase transition temperature, T_{R-T}, from rhombohedral to tetragonal and T_{T-C}, from tetragonal to cubic, are approximately 340 and 540 °C on heating, respectively, for BNT single crystals.

The BNT ceramic shows the strong ferroelectric properties of a large remanent polarization and relatively high piezoelectric properties compared with other lead-free piezoelectric ceramics. However, data on piezoelectric properties of the BNT ceramic are scarce because it is difficult to pole this ceramic due to a large coercive field, Ec (=

73kV/cm) except in specialized work. On the other hand the BNT ceramic need a high sintering temperature of more than 1200 °C to obtain a dense body. It is thought that the vaporization of Bi ions occurred during the sintering process at temperature higher than 1200 °C, resulting in the poor poling treatments because of low resistivities. From the thermograph measurement, the weight loss caused by the Bi vaporization was carried out at over 1130 °C. Various processes and method are thought to prevent the vaporization and to obtain the stoichiometric BNT ceramic. Thus, the BNT ceramic should be sintered at 1100 °C and lower [28].

1.3.1.3 Alkaline niobate-based ceramics

KNN is a solid solution of ferroelectric $KNbO_3$ and antiferroelectric $NaNbO_3$ [29]. Both end members of the solid solution are orthorhombic at room temperature. Pure KNN ceramics sintered by the conventional solid-state reaction in air exhibit a high Curie temperature ($T_c = 420$ °C), a good ferroelectricity ($P_r = 33$ $\mu C/cm^2$), while poor piezoelectricity ($d_{33} = 80$ pC/N) and bulk density [30]. The obstacles of the processing for KNN-based ceramics is largely due to the instability of the KNN phase and volatility of the alkali oxides sintering at high temperatures, which make it difficult to obtain high density [31].

To improve the sinterability and piezoelectric properties of KNN ceramics, a lot of different materials have been used to either dope it or to substitute the main elements. Some of these combinations include: KNN–Ba [32], KNN–SrTiO$_3$ [33], KNN–LiNbO$_3$ [34], KNN–LiTaO$_3$, KNN–LiSbO$_3$, (K,Na,Li)(Nb,Ta,Sb)O$_3$ [35] and pure KNN with sintering aids like CuO, ZnO, MnO$_2$and Bi$_2$O$_3$. The KNN–LiTaO$_3$–LiSbO$_3$ composition which was reported by Saito [35] remains one of the best so far in terms of piezoelectric properties. This was initially attributed to the existence of a morphotropic phase boundary (MPB) at the proposed composition. Later reports show however that the addition of dopants lowers the tetragonal to orthorhombic phase transition in the KNN system to room temperature and is therefore rather considered as a polymorphic phase transition. Efforts are still being made to see if and how the system can be further improved [36].

1.3.2 Tungsten-bronze structure

Figure 1-5 shows a cross-section of the structure normal to the fourfold axis. The corner linking of octahedral leading to five-, four-, and threefold tunnels for the A-sites running parallel to the fourfold symmetry axis. The general chemical formula is of the from $(A_1)_4(A_2)_2C_4B_{10}O_{30}$, where A_1 are 15-fold coordinated sites in the fivefold tunnels, A_2 are 12-fold coordinated sites in the fourfold tunnels, C are ninefold coordinated sites in the threefold tunnels, and B are the sixfold coordinated B-sites cation as in the perovskite [37].
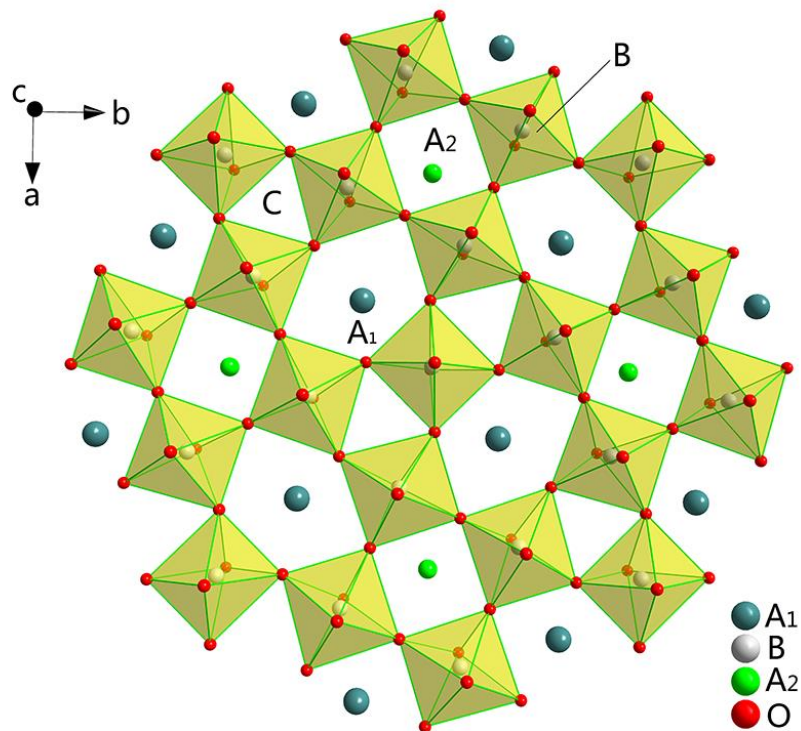
Fig. 1-5 Cross-section of a ferroelectric tetragonal tungsten bronze taken normal to the fourfold axis.

Currently, most of piezoelectric ceramics with the tungsten-bronze structure are niobate, mainly including: [38-40] $(Sr_{1-x}Ba_x)Nb_2O_6$, $(A_xSr_{1-x})_2NaNb_5O_{15}$ (A=Ba, Ca, Mg…) and $(K_xNa_{1-x})_2(Sr_yBa_{1-y})Nb_{10}O_{30}$.

1.3.3 Bismuth layer structure

Bismuth-layer-structured ferroelectrics (BLSFs) have a crystal structure in which

8

bismuth oxide layers ($(Bi_2O_2)^{2+}$ layers) are interleaved with pseudo-perovskite blocks along the crystallographic c-axis, as shown in Fig. 1-6. The pseudo-perovskite blocks have a formula of $(M_{m-1}R_mO_{3m+1})^{2-}$, where M is mono-, di-, or trivalent ions; R is tetra-, penta-, or hexavalent ions such as Ti^{4+} and Nb^{5+}; and m is the number of RO_6 octahedra in the pseudo-perovskite block (m = 1, 2, 3, 4, and 5) [41]. With the increase of m, the piezoelectricity is improved, however the cure temperature is reduced.
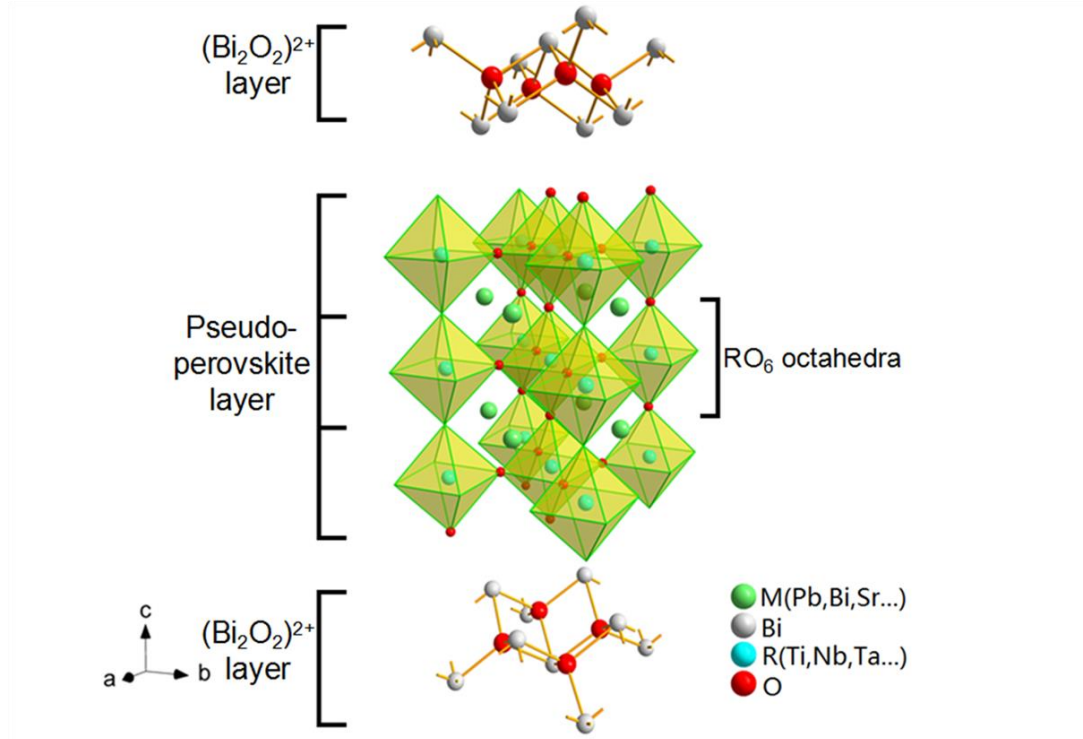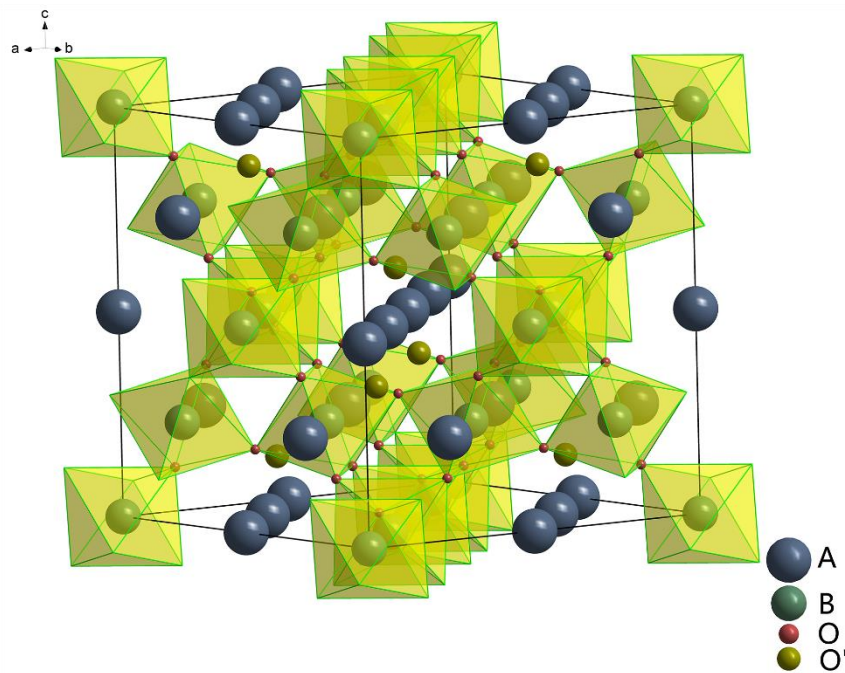

Fig. 1-6 Schematic drawing showing the crystal structure of BLSF (m = 3) of one half of the pseudo-tetragonal unit cell.

This system can be summarized as follows [42-44] :

(1) $Bi_4Ti_3O_{12}$;

(2) $MBi_4Ti_4O_{15}$ (M = Sr, Ba, Ca) ;

(3) $MBi_2R_2O_9$ (M = Sr, Ba, Ca, R = Nb, Ta) ;

(4) $BiTiRO_9$ (R = Nb, Ta).

1.3.4 Pyrochlore structure

Fig. 1-7 Pyrochlore lattice

The pyrochlore structure which shows in Fig. 1-7 is a common vertex (of NbO_6 or TaO_6) octahedra, while the gap between the larger of Cd^{2+} (or of Pb^{2+}) ions located in the oxygen octahedron. The more general crystal structure describes materials of the type $A_2B_2O_6$ and $A_2B_2O_7$ where the A and B species are generally rare-earth or transition metal species. Ferroelectrics of this structure appears only in a limited number of compounds $Cd_2Nb_2O_2$ [45], $Pb_2Nb_2O_7$ and $Cd_2Ta_2O_7$ [46].

1.4 Main Performance Parameter of Piezoelectric Ceramics

Because a piezoelectric ceramic is anisotropic, physical constants relate to both the direction of the applied mechanical or electric force and the directions perpendicular to the applied force. Consequently, each constant generally has two subscripts that indicate the directions of the two related quantities, such as stress and strain for elasticity [47]. Three orthogonal axes are represented by subscript 1-3. By convention, axis 3 is the direction of polarization of piezoelectric ceramics. Subscripts 4-6 indicate stress or strain in shear form about axes 1-3, respectively. This is illustrated in Figure 1-8.
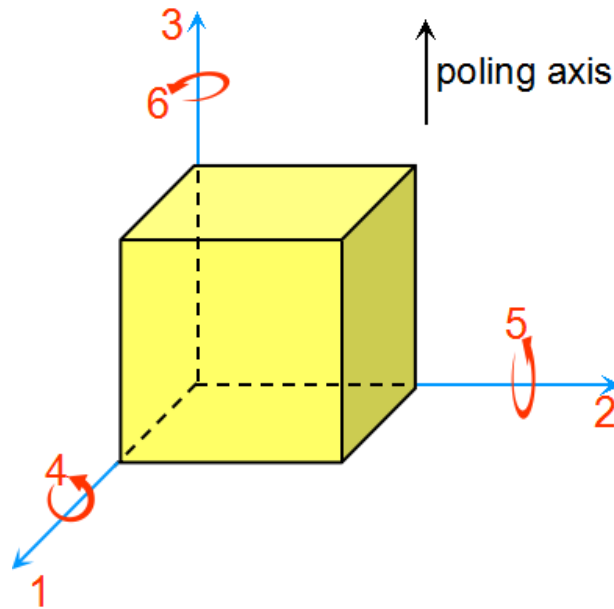
Fig. 1-8 Reference axes

Piezoelectric Constant

Piezoelectric constant quantifies the volume change when a piezoelectric material is subject to an electric field, or the polarization on application of a stress. The piezoelectric constants are defined as follows:

Piezoelectric Charge Constant: $d = \dfrac{\text{charge density developed}}{\text{applied mechanical stress}}$ CN^{-1}

Piezoelectric Voltage Constant: $g = \dfrac{\text{electric field developed}}{\text{applied mechanical stress}}$ VmN^{-1}

Because the strain induced in a piezoelectric material by an applied electric field is the product of the value for the electric field and the value for d, d is an important indicator of a material's suitability for strain-dependent (actuator) applications. Due to the strength of the induced electric field produced by a piezoelectric material in response to an applied physical stress is the product of the value for the applied stress and the value for g, g is important for assessing a material's suitability for sensing (sensor) applications [47].

Curie Temperature

Most piezoelectric materials have a Curie Temperature (T_c). Above T_c the materials are not polar indicate that they lost the piezoelectricity. T_c decide the ceiling temperature for the use of piezoelectric materials.

Permittivity

The permittivity, or dielectric constant, ε, for a piezoelectric ceramic material is the dielectric displacement per unit electric field. ε^T is the permittivity at constant stress, ε^S is the permittivity at constant strain.

E.g. ε^T_{11} is the permittivity for dielectric displacement and electric field in direction 1, under constant stress. The first superscript to ε indicates the direction of the dielectric displacement, and the second subscript is the direction of the electric field.

Dielectric Dissipation Factor

The loss tangent, tanδ, is defined as the ratio of resistance to reactance in the parallel equivalent circuit of Fig. 1-9 (a). It is a measure of the dielectric losses in the material and therefore also a measure of the heat generation capacity of the ceramic when operated under dynamic conditions. This is a direct measurement and is usually formed at the same conditions as the capacitance measurement [48].
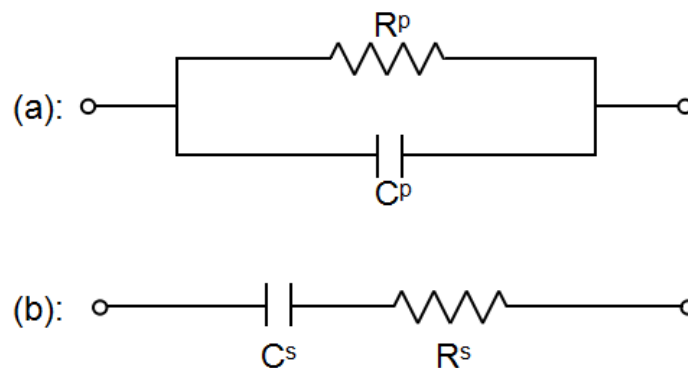

Fig. 1-9 Non-resonant (a) parallel and (b) series equivalent circuit

Electromechanical Coupling Factor

The electromechanical coupling factor, k, a numerical measure of the conversion

efficiency between electrical and acoustic energy in piezoelectric materials. It is an indicator of the effectiveness with which a piezoelectric material converts electrical energy into mechanical energy, or converts mechanical energy into electrical energy.

Mechanical Quality Factor

Mechanical quality factor, Q_M, the ratio of reactance to resistance in the series equivalent circuit of Fig. 1-9(a) is given by:

$$Q_M = \frac{f_a^2}{2\pi f_r Z_m C(f_a^2 - f_r^2)}$$

(1.3)

where C is the low frequency (1 kHz) capacitance; Z_m is the minimum impedance; f_r is resonant frequency, and f_a is anti-resonant frequency.

1.5 How to Improve the Performance of Piezoelectric Ceramics

1.5.1 Composite modification

Piezoelectric ceramics materials compared with piezoelectric monocrystal materials have advantages as follow:
(1) The preparation process is easy.
(2) The ceramics materials could be made into different shapes of components, and its polaxis direction could be chosen for different purpose.
(3) By changing composition, the performance could be changed easily and purposively.

The last point is particularly important in industrial application. Taking a basic component as the main body, by adding additives, the component trace changed, and a lot of derivative systems with various properties could be obtained. The composite modification mainly including:
(a) Addition of oxide.

Almost all of oxides are used to modified the properties of piezoelectric ceramics.

Oxides with characteristic mainly include Nb_2O_5, Ta_2O_5, Nd_2O_3, Bi_2O_3, La_2O_3, Sn_2O_3, WO_3, *etc.* Through adding above oxides, coercive field decrease, resistivity increase, cause polarization easily, and piezoelectricity increased. But electrical quality factor (Q_E) and mechanical quality factor (Q_M) could decline, "soft" materials could be obtained. On the other hand, adding Fe_2O_3, Cr_2O_3, MnO_2, *etc.* could make coercive field increase, cause polarization difficulty. However, the value of Q_E and Q_M could increase, "hard" materials could be obtained.

(b) Substitution of element and composite oxides.

For better dielectricity and piezoelectric properties, initially Ca, Sr, Ba elements are used to substitute Pb; Sn, Hf elements are used to substitute Zr, Ti. Later $A^{1+}B^{5+}O_3$ and $A^{3+}B^{3+}O_3$ systems are studied detailedly. Among them the using of $BiFeO_3$ [49,50] and $LiNbO_3$[51] obtained remarkable results. All these case above have wider solution range than (a), thus the degree of variability in the properties is lager.

(c) Composite substitution with chemical valence compensation.

For example, $[Na_{1/2}^{1+}Bi_{1/2}^{3+}]$ is used to substitute Pb [52]; and $[Fe_{1/2}^{3+}Nb_{1/2}^{5+}]$ is used to substitute [Zr, Ti] [53]. This substitution characterized by various ionic combination and wider solution range.

1.5.2 Morphotropic phase boundary

Morphotropic phase boundary (MPB) is defined as an abrupt structural change within a solid solution with composition. As an example, lead zirconate titanate (PZT) is used widely mainly due to its unique properties at the MPB, at a composition where the PZ : PT ratio is almost 1 : 1, as shown in Fig. 1-10(a) [54]. PZT compositions near the MPB have both high ε_r and high k_p as shown in Fig. 1-10(b) [54]. Nowadays, the term "MPB" is used to refer to the phase transition between the tetragonal and the rhombohedral ferroelectric phases as a result of varying the composition or as a result of mechanical pressure. In the vicinity of the MPB, the crystal structure changes abruptly and the dielectric properties in ferroelectric materials and the electromechanical properties in piezoelectric materials become maximum [55].
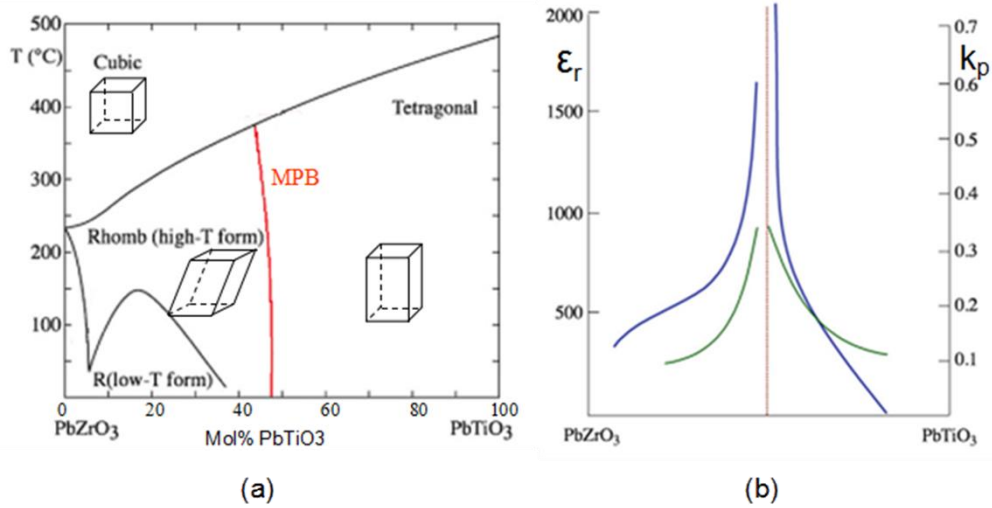
Fig. 1-10 (a) PZT phase diagram and (b) dielectric constants and coupling
coefficients for PZT composition near the MPB

Not only used in lead-based materials, the characteristics of MPB in lead free are also used in many lead-free materials to improve their performance. $xNa_{1/2}Bi_{1/2}TiO_3$–$(1-x)BaTiO_3$ (BNT–BT) or $xNa_{1/2}Bi_{1/2}TiO_3$–$(1-x)K_{1/2}Bi_{1/2}TiO_3$ (BNT–KBT) have enhanced piezoelectric properties due to MPB between rhombohedral (R) and tetragonal (T) phase. Figure 1-11(a) [56] shows the phase diagram of $xNa_{1/2}Bi_{1/2}TiO_3$–$(1-x)BaTiO_3$ system. Near the MPB its delectric and pizeoelectric properties are enhanced , as shown in Fig. 1-11(b) [57]. For the KNN system, the enhanced dielectric and piezoelectric properties were attributed to a MPB which separating orthorhombic and tetragonal phases[58-60]. This MPB is actually a polymorphic phase transition, where the increased polarizability associated with a temperature transition leads to increased dielectric and piezoelectric properties [61]. The dielectric and piezoelectric properties of KNN systems are enhanced by additives such as $LiNbO_3$, $LiSbO_3$ modified [62,63].
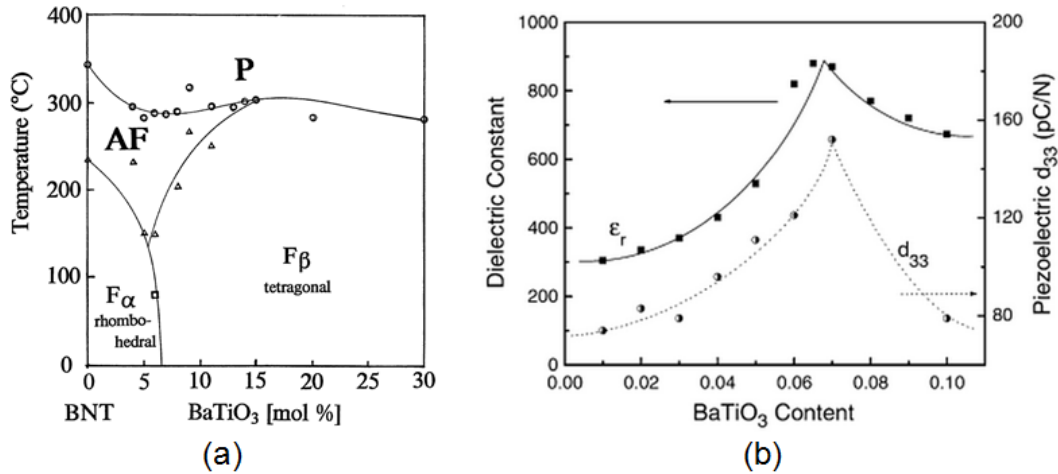
Fig. 1-11 (a) phase diagram of $xNa_{1/2}Bi_{1/2}TiO_3$–$(1-x)BaTiO_3$ system and
(b) delectric and pizeoelectric properties in BNT–BT.

1.5.3 Texture techniques

Using texture techniques to control the grain orientation of polycrystalline ceramics is an effective approach to improve the piezoelectric properties. Figure 1-12 shows the two-dimensional diagram of grain orientation.
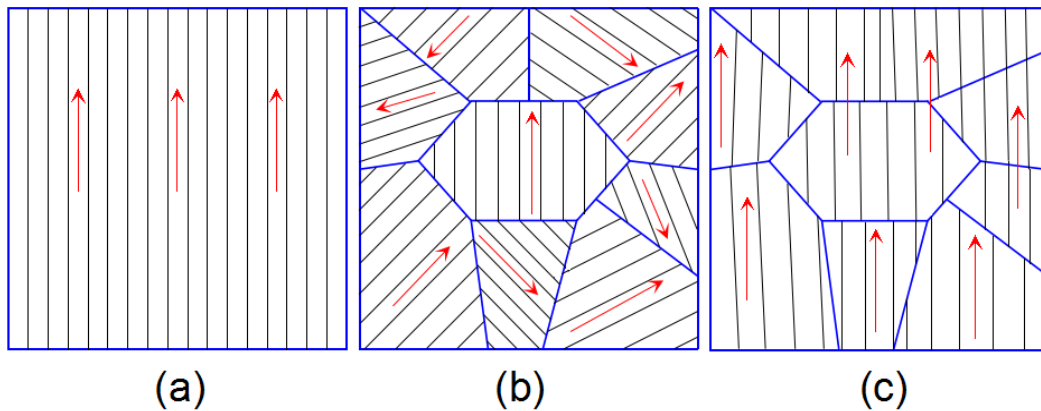
Fig. 1-12 Grain orientation. (a) single crystal, (b) polycrystal, (c) textured polycrystal

Hot processing is a traditional method for the grain orientation. Tadashi *et al.* prepared $SrBi_4Ti_4O_{15}$ ceramics with a grain orientation degree of 95% via hot-forging technique [64]. However, due to the disadvantage such as complexity of the process, hot processing is not widely used.

Strong magnetic field is a effective method for preparing textured piezoelectric ceramics. Makiya *et al.* prepared $Bi_4Ti_3O_{12}$ ceramics with a grain orientation above 90%

at $\{hk0\}$ plane [65]. Masahiko Kimura *et al.* prepared $CaBi_4Ti_4O_{15}$ ceramics with a grain orientation of 82%, and the electromechanical coupling coefficient is about 1.5 times larger than that of the non-oriented ceramics [66].

Templated Grain Growth (TGG) and Reactive Templated Grain Growth (RTGG) are versatile and effective technique for the fabrication of textured ceramics. This technique could be used to texture not only bismuth layer structure but also perovskite-structure and tungsten-bronze structure piezoelectric ceramics. Some of the textured lead-free piezoceramics and their orientation degree prepared by TGG/RTGG technique are listed in Table 1-1.

Table 1-1 Some of textured lead-free piezoceramics prepared by TGG/RTGG technique

Textured composition	Template particles	Orientation degree (%)	Ref.
$0.92Na_{0.5}Bi_{0.5}TiO_3$–$0.08BaTiO_3$	plate-like $Bi_{2.5}Na_{3.5}Nb_5O_{18}$	60	[67]
$0.94Bi_{0.5}Na_{0.5}TiO_3$–$0.6BaTiO_3$	plate-like BNT	92.5	[68]
$(K_{0.44}Na_{0.52}Li_{0.04})(Nb_{0.84}Ta_{0.10}Sb_{0.06})O_3$	plate-like $NaNbO_3$	91	[35]
$Bi_4Ti_3O_{12}$	plate-like $Bi_4Ti_3O_{12}$	92	[69]
$Ba_2NaNb_5O_{15}$	acicular $Ba_2NaNb_5O_{15}$	80.1	[70]

This method includes two key points: the preparation of anisotropic template grain and the process control of template particles oriented in the ceramic matrix. The particles which were appropriate for the ideal template of TGG and RTGG texture techniques have to meet some requirements. Firstly, template particles must have the needle-like or plate-like morphology and have suitable aspect ratio or radius-thickness ratio. In addition, before the actual application the template particles must have structural conformance with the ceramic matrix. Moreover, the melting point of template particles should be higher than the ceramics sintering temperature. The schematic of RTGG techniques is shown in Fig. 1-13.
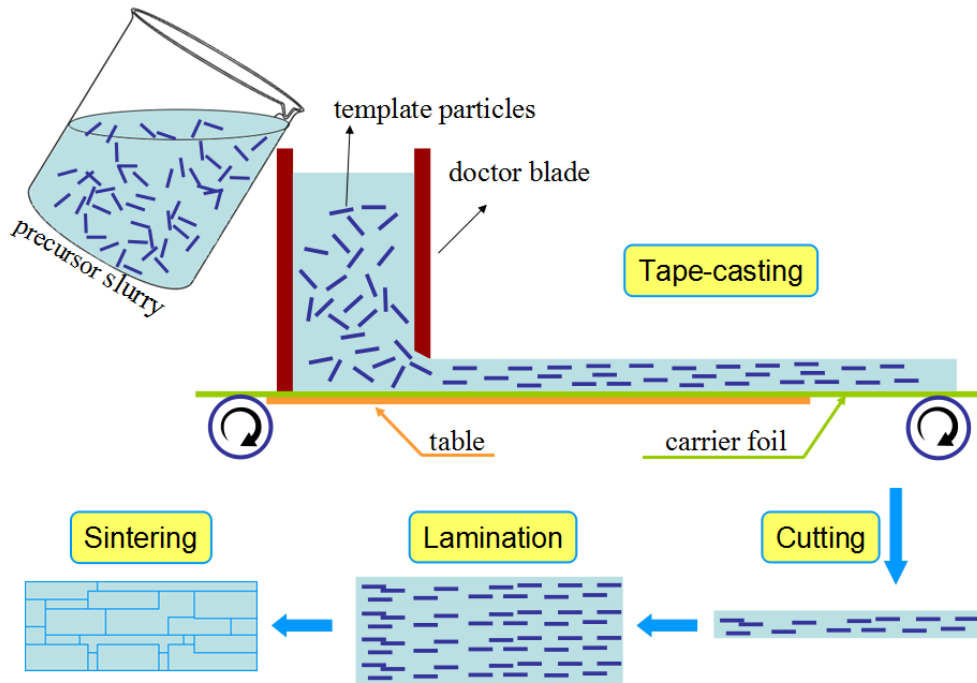
Fig. 1-13 Schematic diagram of reactive templated grain growth techniques.

1.5.4 Nano effect

Numbers of experiments show that the properties of nanoscale ferroelectric thin film, particles, nanowires, nanotube are quite different from those of bulk materials. When the scale of the material is reduced to the nanometer range, surface effect and size effect on its performance becomes very important. Uchino *et al.* [71] studied the effect of surface tension on the Curie temperature of $BaTiO_3$ particles by X-ray diffraction. The results show that the Curie temperature changes with the change of particle size, and it has great difference with the bulk material. Then Ma *et al.* [72] gave the influence of surface tension on the ferroelectric properties of nanomaterials. Recently, Zhou *et al.* [73] prepared PZT nanowires with the size of 70nm. They also confirmed the ferroelectric properties significantly enhanced due to the surface tension. Liu *et al.* [74] found PBST nanotube had stronger ferroelectric properties.

Recently years, theoretical studies on the size effect and surface effect of ferroelectric thin films are divided into phenomenological method and microscopic models method. The phenomenological method can predict the correlative properties of nano-ferroelectric thin films [75-77]. Recently, first principles study simulation experiments of ABO_3 type ferroelectric material was reported [78]. S. K. Streiffer *et al.*

[79] prepared PbTiO$_3$ thin films with different thickness on SrTiO$_3$ substrate and provided relationship between film thickness and Curie temperature. With the progress of the technology and the maturity of theoretical research, the performance nanoscale materials attract a wide range of attention in all aspects of chemical and physics.

1.6 Thesis Objectives and Organization

1.6.1 Thesis Objectives

Piezoelectric ceramic components have many applications such as sensors, transducer, resonators, filters in our daily life, industry and even military field. However, the most wildly used piezoelectric ceramics are Pb-based ceramics. With the improvement of healthy and environmental protection requirements, the development of lead-free piezoelectric ceramics has become a requirement. Potassium sodium niobate (KNN) based piezoelectric materials system is deemed as one of the most promising candidates for substitution of lead-based piezoelectric materials due to the high piezoelectric coefficient and high Curie temperature. However, their piezoelectric properties are still lower than the lead-based piezoelectric materials. Therefore, the objectives of this research is develop high performance lead-free piezoelectric ceramics. Specific objectives are as follows:

(a) Development of KNN-based piezoelectric ceramics with performance-temperature stability.

(b) Preparation of NaNbO$_3$ template particles by hydrothermal method.

(c) Fabrication of oriented piezoelectric ceramics.

1.6.2 Thesis Organization

The thesis consists of 7 chapters. Chapter 1 introduces the background and objectives of this research. Chapter 2 illustrates the reagents, equipment and characterization equipment. Chapter 3 expounds the MPB slope adjusted in BZ–KNLN system. Chapter 4 and 5 discusses the synthesis of NaNbO$_3$ template particles by

hydrothermal method. Chapter 6 expounds the fabrication of oriented KNLN–BZ–BNT ceramics. Finally, chapter 7 presents the conclusions of this research.

References

[1] Tichý, J., Erhart, J., Kittinger, E., & Prívratská, J. Fundamentals of Piezoelectric Sensorics, Springer-Verlag Berlin Heidelberg, 2010.

[2] Curie J, Curie P. Development par compression de l' eletricite polaire dans les cristaux hemiedres a faces inclines. Bulletin no. 4 de la Societe Mineralogique de France 3, 90, 1880 and Comptes Rendus Acad. Sci. Paris 91, 294, 1880.

[3] Lippmann HG. Sur le principe de la conversation de l' eletricite ou second principe de la theorie des phenomenes electriques. Comptes Rendus Acad. Sci. Paris 92, 1049, 1881.

[4] Curie J, Curie P. Contractions et dilations productes par des tensions electriques dans les cristaux hemiedres a faces inclines. Comptes Rendus Acad. Sci. Paris 93, 1137, 1884.

[5] Voigt W. General theory of the piezo and pyroelectric properties of crystals. Abh. Gott. 36, 1, 1890.

[6] Cady WG. Piezoelectricity, Vol. 1 & 2. Dover Publishers, New York, 1964.

[7] Tiersten HF. Linear Piezoelectric Plate Vibrations. Plenum Press, New York, 1969.

[8] Parton VZ, Kudryavtsev BA. Electromagnetoelasticity, Piezoelectrics and Electrically Conductive Solids. Gordon and Breach Science Publishers, New York, 1988.

[9] Ikeda T. Fundamentals of Piezoelectricity. Oxford Science Publications, New York, 1990.

[10] Rogacheva NN. The Theory of Piezoelectric Shells and Plates. CRC Press, Boca Raton, 1994.

[11] Qin QH. Fracture Mechanics of Piezoelectric Materials. WIT Press, Southampton, 2001.

[12] Qin QH. Green's Function and Boundary Elements in Multifield Materials. Elsevier, Oxford, 2007.

[13] Qin QH, Yang QS. Macro-Micro Theory on Multifield Behaviour of Heterogeneous Materials. Higher Education Press & Springer, Beijing, 2008.

[14] A.V. Shirinov, W.K. Schomburg. Pressure sensor from a PVDF film, Sensors and Actuators A: Physical, 142, 48-55, 2008.

[15] P Muralt. Ferroelectric thin films for micro-sensors and actuators: a review, J. Micromech. Microeng. 10, 136, 2000.

[16] Yi, S. H., & Kim, E. S. Micromachined piezoelectric microspeaker, Jpn. J. Appl. Phys. 44, 3836, 2005.

[17] Kim, H. J., Koo, K., Lee, S. Q., Park, K. H., & Kim, J. High performance piezoelectric microspeakers and thin speaker array system, ETRI journal, 31, 680-687, 2009.

[18] Kim H J, Yang W S, No K. Improvement of low-frequency characteristics of piezoelectric speakers based on acoustic diaphragms, Ultrasonics, Ferroelectrics, and Frequency Control, IEEE Transactions, 59, 2027-2035, 2012.

[19] Saunders R E, Gough J E, Derby B. Delivery of human fibroblast cells by piezoelectric drop-on-demand inkjet printing, Biomaterials, 29, 193-203, 2008.

[20] Nagaraj, V. J., Eaton, S., Thirstrup, D., & Wiktor, P. Piezoelectric printing and probing of Lectin NanoProbeArrays for glycosylation analysis, Biochemical and biophysical research communications, 375, 526-530, 2008.

[21] Benjeddou A. Advances in piezoelectric finite element modeling of adaptive structural elements: a survey, Computers & Structures, 76, 347-363, 2000.

[22] Abbate, A., Koay, J., Frankel, J., Schroeder, S. C., & Das, P. Signal detection and noise suppression using a wavelet transform signal processor: application to ultrasonic flaw detection, Ultrasonics, Ferroelectrics, and Frequency Control, IEEE Transactions, 44, 14-26, 1997.

[23] Vig J R. Quartz crystal resonators and oscillators for frequency control and timing applications. A tutorial, NASA STI/Recon Technical Report N, 95, 19519, 1994.

[24] Gallone, G., Carpi, F., De Rossi, D., Levita, G., & Marchetti, A. Dielectric constant enhancement in a silicone elastomer filled with lead magnesium niobate-lead titanate, Materials Science and Engineering: C, 27, 110-116, 2007.

[25] Shastry, S., Srinivasan, G., Bichurin, M. I., Petrov, V. M., & Tatarenko, A. S. Microwave magnetoelectric effects in single crystal bilayers of yttrium iron garnet and

lead magnesium niobate-lead titanate, Physical Review B, 70, 064416, 2004.

[26] European Union. "EU-Directive 2002/95/EC: Restriction of the Use of Certain Hazardous Substances in Electrical and Electronic Equipment (RoHS)," Official J. Eur. Union, 46 [L37] 19-23, 2003.

[27] M. M. Vijatović, J. D. Bobić, B. D. Stojanović. History and challenges of barium titanate: Part I, Science of Sintering, 40, 155-165, 2008.

[28] Shashank Priya, Sahn Nahm. Lead-free piezoelectrics, Springer New York, 255-290, 2012.

[29] W. R. Cook B. Jaffe and H. Jaffe. Piezoelectric ceramics, Academic Press, London, 1971.

[30] L. Egerton and D. M. Dillon. J. Am. Ceram. Soc., 42, 438, 1959.

[31] Yi-qing Lu and Yong-xiang Li. A review on lead-free piezoelectric ceramics studies in china, Journal of Advanced Dielectrics, 1, 269-288, 2011.

[32] Ahn, Z. S. and Schulze, W. A. Conventionally sintered $(Na_{0.5} K_{0.5})N_bO_3$ with barium additions. J. Am. Ceram. Soc., 70, 18-21, 1987.

[33] Kosec, M., Bobnar, V. Hrovat, M., Bernard, J., Malic, B. and Holc, J., New lead-free relaxors based on the $K_{0.5} Na_{0.5}NbO_3$-$SrTiO_3$ solid solution. J. Mater. Res., 19, 1849-1854, 2004.

[34] Ken-ichi Kakimoto, Koichiro Akao, Yiping Guo and Hitoshi Ohsato. Raman scattering study of piezoelectric $(Na_{0.5}K_{0.5})NbO_3$-$LiNbO_3$ ceramics, Jpn. J. Appl. Phys., 44, 7064-7067, 2005.

[35] Saito Y., Takao H., Tani T., Nonoyama T., Takatori K., Homma T., Nagaya T. and Nakamura M. Lead-free piezoceramics, Nature, 432, 84-87, 2004.

[36] Henry Ekene Mgbemere, Ralf-Peter Herber and Gerold A. Schneider. Effect of MnO_2 on the dielectric and piezoelectric properties of Alkaline Niobate based lead free piezoelectric ceramics, Journal of the European Ceramic Society, 29, 1729-1733, 2009.

[37] Walter Heywang, Karl Lubitz, Wolfram Wersing. Piezoelectricity: evolution and future of a technology, Springer-Verlag Berlin and Heidelberg, 147, 2008.

[38] P. B. Jamieson, S. C. Abrahams and J. L. Bernstein. Ferroelectric tungsten bronze-type crystal structures. I. Barium strontium niobate $Ba_{0.27}Sr_{0.75}Nb_2O_{5.78}$, J. Chem. Phys., 48, 5048, 1968.

[39] Lingling Wei, Zupei Yang, Rui Gu and Hongmei Ren. The phase formation, microstructure and electric properties of tungsten bronze ferroelectric $Sr_2NaNb_5O_{15}$

ceramics, J. Am. Ceram. Soc., 93, 1978-1983, 2010.

[40] R. L. Barns. Barium sodium niobate ($Ba_{(4+x)}Na_{(2-2x)}Nb_{10}O_{30}$): crystallographic data and thermal expansion coefficients, J. Appl. Cryst., 1, 290-292, 1968.

[41] Hiroshi Irie, Masaru Miyayama and Tetsuichi Kudo. Domain motion in bismuth-layer-structured ferroelectrics by applying electric fields, Jpn. J. Appl. Phys., 38, 5958-5963, 1999.

[42] J. F. Dorrian, R. E. Newnham, D. K. Smith & M. I. Kay. Crystal structure of $Bi_4Ti_3O_{12}$, Ferroelectrics, 3, 17-27, 1972.

[43] B. Aurivillius. Mixed Oxides with Layer Lattices: III. Structure of $BaBi_4Ti_4O_{15}$, Arkiv For Kemi, 2, 519, 1950.

[44] M. Adamczyk, L. Kozielski, M. Pilch, M. Pawełczyk, A. Soszyński. Influence of vanadium dopant on relaxor behavior of $BaBi_2Nb_2O_9$ ceramics, Ceramics International, 39, 4589-4595, 2013.

[45] T Malcherek, U Bismayer and C Paulmann. The crystal structure of $Cd_2Nb_2O_7$: symmetry mode analysis of the ferroelectric phase, J. Phys.: Condens Matter, 22, 205401, 2010.

[46] Michael Fischer, Thomas Malcherek, and Ulrich Bismayer. Structure and stability of $Cd_2Nb_2O_7$ and $Cd_2Ta_2O_7$ explored by ab initio calculations, Physical Review B, 78, 014108, 2008.

[47] APC International Ltd. Piezoelectric ceramics: principles and applications, APC International, Ltd., 2002.

[48] Jordan T L. Ounaies Z. Piezoelectric ceramics characterization, Institute for computer applications in science and engineering hampton va, 2001.

[49] Chao, X., Yang, Z., Kang, C., & Chang, Y. Effects of $BiFeO_3$ addition on electrical properties and temperature stability of low temperature sintered PZT-PFW-PMN ceramics, Sensors and Actuators A: Physical, 141,482-488, 2008.

[50] Sun, X., Chen, J., Yu, R., Xing, X., Qiao, L., & Liu, G. $BiFeO_3$-doped $(Na_{0.5}K_{0.5})NbO_3$ lead-free piezoelectric ceramics, Sci. Technol. Adv. Mater. 9, 025004, 2008.

[51] Shen, Z. Y., Li, Y. M., Jiang, L., Li, R. R., Wang, Z. M., Hong, Y., & Liao, R. H. Phase transition and electrical properties of $LiNbO_3$-modified $K_{0.49}Na_{0.51}NbO_3$ lead-free piezoceramics, J Mater Sci: Mater Electron, 22, 1071-1075, 2011.

[52] Lee, J. K., Yi, J. Y., & Hong, K. S. Relationship between structure and dielectric property in $(1-x)$(Na$_{1/2}$Bi$_{1/2}$)TiO$_3$-xPbZrO$_3$ ceramics, Jpn. J. Appl. Phys., 40, 6003-6007, 2001.

[53] Kahoul, F., Hamzioui, L., Abdessalem, N., & Boutarfaia, A. Synthesis and piezoelectric properties of Pb$_{0.98}$Sm$_{0.02}$[(Zr$_y$,Ti$_{1-y}$)$_{0.98}$(Fe$_{1/2}^{3+}$,Nb$_{1/2}^{5+}$)$_{0.02}$]O$_3$ ceramics, Materials Sciences and Applications, 3, 50-58, 2012.

[54] B. Jaffe, W.R. Cook, and H. Jaffe. Piezoelectric ceramics, Academic Press, London, p.92, 1971.

[55] Ibrahim, A. B. M., Murgan, R., Rahman, M. K. A., & Osman, J. Morphotropic phase boundary in ferroelectric materials, Ferroelectrics-Physical Effects, 2011.

[56] T. Takenaka, K. Maruyama, and K. Sakata. (Bi$_{1/2}$Na$_{1/2}$)TiO$_3$-BaTiO$_3$ system for lead-free piezoelectric ceramics, Jpn. J. Appl. Phys., 30, 2236, 1991.

[57] S.J. Zhang, T.R. Shrout, H. Nagata, Y. Hiruma, and T. Takenaka. Piezoelectric properties in (K$_{0.5}$Bi$_{0.5}$)TiO$_3$-(Na$_{0.55}$Bi$_{0.5}$)TiO$_3$-BaTiO$_3$ lead free ceramics, IEEE Trans. Ultra. Ferro. Freq. Control., 54, 2007.

[58] E. Hollenstein, M. Davis, D. Damjanovic, N. Setter. Piezoelectric properties of Li- and Ta-modified ceramics, Appl. Phys. Lett. 87, 182905, 2005.

[59] Y. Guo, K. Kakimoto, H. Ohsato. (Na$_{0.5}$K$_{0.5}$)NbO$_3$-LiTaO$_3$ lead-free piezoelectric ceramics, Mater. Lett. 59, 241, 2005.

[60] R. Wang, R. Xie, K. Hanada, K. Matsusaki. H. Bando, M. Itoh, Phys. Status Sol, A., Phase diagram and enhanced piezoelectricity in the strontium titanate doped potassium-sodium niobate solid solution, 202, R57-R59, 2005.

[61] Shujun Zhang, Ru Xia and Thomas R. Shrout. Lead-free piezoelectric ceramics vs. PZT?, J Electroceram., 19, 251-257, 2007.

[62] Y. Guo, K. Kakimoto, H. Ohsato. Phase transitional behavior and piezoelectric properties of (Na$_{0.5}$K$_{0.5}$)NbO$_3$-LiNbO$_3$ ceramics, Appl. Phys. Lett. 85, 4121, 2004.

[63] Zang, G. Z., Wang, J. F., Chen, H. C., Su, W. B., Wang, C. M., Qi, P., & Shrout, T. R. Perovskite (Na$_{0.5}$K$_{0.5}$)$_{(1-x)}$(LiSb)$_x$Nb$_{1-x}$O$_3$ lead-free piezoceramics, Appl. Phys. Lett., 88, 212908, 2006.

[64] Tadashi Takenaka and Koichiro Sakata. Grain orientation and electrical properties

of hot-forged $Bi_4Ti_3O_{12}$ ceramics, Jpn. J. Appl. Phys., 19, 31, 1980.

[65] Atsushi Makiya, Dai Kusano, Satoshi Tanaka, Nozomu Uchida, Keizo Uematsu, Tsunehisa Kimura, Koichi Kitazawa, Yutaka Doshida. Particle oriented bismuth titanate ceramics made in high magnetic field, Journal of the ceramic society of Japan, 111, 702-704, 2003.

[66] Masahiko Kimura, Kosuke Shiratsuyu, Akira Ando, Tohru S. Suzuki and Yoshio Sakka. Layer structure of textured $CaBi_4Ti_4O_{15}$ ceramics fabricated by slip casting in high magnetic field, J. Am. Ceram. Soc., 90, 1463-1466, 2007.

[67] Feng Gao, Rong-zi Hong, Jia-ji Liu   Grain growth kinetics of textured $0.92Na_{0.5}Bi_{0.5}TiO_3$-$0.08BaTiO_3$ ceramics by tape casting with $Bi_{2.5}Na_{3.5}Nb_5O_{18}$ templates, Journal of Electroceramics, 24, 145-152, 2010.

[68] T. Kimura, T. Takahashi, T. Tani, Y. Saito. Preparation of crystallographically textured $Bi_{0.5}Na_{0.5}TiO_3$-$BaTiO_3$ ceramics by reactive-templated grain growth method, Ceramics International, 30, 1161-1167, 2004.

[69] Kan, Y., Wang, P., Li, Y., Cheng, Y. B., & Yan, D. Fabrication of textured bismuth titanate by templated grain growth using aqueous tape casting, Journal of the European Ceramic Society, 23, 2163-2169, 2003.

[70] Qiao-Xia Bao, Li-Hui Zhu, Qing-Wei Huang, Jiong Xv. Preparation of textured $Ba_2NaNb_5O_{15}$ ceramics by templated grain growth, Ceramics International, 32, 745-749, 2006.

[71] K. J. Uchino, E. J. Sadanaga and Terikiyo Hirose. Dependence of crystal structure on particle size in Barium Titanate. J. Am. Ceram. Soc., 72, 1555-1560, 1989.

[72] W. H. Ma, M. S. Zhang, and Z. H. Lu. A study of size effects in $PbTiO_3$ nanocrystal. Phys. Stat. Sol. (b)., 166, 811-814, 1998.

[73] Zhou, Z. H., Gao, X. S., Wang, J., Fujihara, K., Ramakrishna, S., & Nagarajan, V. Giant Strain in $PbZr_{0.2}Ti_{0.8}O_3$ nanowires. Appl. Phys. Lett., 90, 052902, 2007.

[74] Liu, W., Sun, X., Han, H., Li, M., & Zhao, X. Z. Surface polarization enhancement in $(Pb_{0.25}Ba_{0.15}Sr_{0.6})$ TiO_3 nanotube. Appl. Phys. Lett., 89, 163122, 2006.

[75] Zhong, W. L., Qu, B. D., Zhang, P. L., & Wang, Y. G. Thickness dependence of the dielectric susceptibility of ferroelectric thin films. Phys. Rev. B., 50, 12375-12380, 1994.

[76] Li, S., Eastman, J. A., Vetrone, J. M., Foster, C. M., Newnham, R. E., & Cross, L. E. Dimension and size effects in ferroelectric. Jpn. J. Appl. Phys. A., 36, 5169-5174, 1997.

[77] K. Ishikawa and T. Uemori. Surface relaxation in ferroelectric perovskite. Phys. Rev. B., 60, 11841-11845, 1999.

[78] J. Junquera and P. Ghosez. Critical thickness for ferroelectric in perovskite ultrathin films. Nature, 422, 506-509, 2003.

[79] Streiffer, S. T., Eastman, J. A., Fong, D. D., Thompson, C., Munkholm, A., Murty, M. R., & Stephenson, G. B. Observation of nanoscale of 180º stripe domains in ferroelectric $PbTiO_3$ thin films. Phys. Rev. Lett., 89, 067601, 2002.

Chapter 2
Experiment and Characterization

This chapter describes the experiment reagents, equipment used for hydrothermal synthesis and tape-casting process. Main characterization instruments in our laboratory are introduced.

2.1 Experiment reagents

All experiment reagents used in this research are listed in table 2.1.

Table 2.1 Experiment reagents.

Reagent	Formula	Purity	Manufacturer
Potassium hydroxide	KOH	85%	Wako pure chemical
Sodium hydroxide	NaOH	97%	Wako pure chemical
Niobium pentoxide	Nb_2O_5	99.9%	High purity chemicals
Lithium carbonate	Li_2CO_3	99.99%	High purity chemicals
Sodium carbonate	Na_2CO_3	99%	High purity chemicals
Potassium carbonate	K_2CO_3	99.5%	High purity chemicals
Barium carbonate	$BaCO_3$	99.95%	High purity chemicals
Titanium oxide	TiO_2	99.99%	High purity chemicals
Zirconium oxide	ZrO_2	98%	High purity chemicals
Bismuth oxide	Bi_2O_3	99.99%	High purity chemicals
Sodium dodecyl benzene sulfonate	$C_{18}H_{29}NaO_3S$	-	Tokyo kasei kogyo
Polyvinyl pyrrolidone	$(C_6H_9NO)_n$	-	Wako pure chemical
Hexadecyl trimethyl ammonium bromide	$C_{16}H_{33}(CH_3)_3NBr$	-	Wako pure chemical
Citric acid	$C_6H_8O_7$	98%	Wako pure chemical
Dodecyl phosphate	$C_{12}H_{27}PO_4$	-	Wako pure chemical

2.2 Experiment equipment

2.2.1 Equipment for hydrothermal synthesis

Fig. 2-1 Teflon-lined autoclave with different volume.

Autoclaves used in hydrothermal synthesis are shown in Fig. 2-1. The corresponding volume from left to right is 50 ml, 100 ml, 200 ml, respectively. The maximum operating temperature is 200 °C. In hydrothermal synthesis, the filling factor of these autoclave is approximately 80 vol%. Fig. 2-2 shows the 1 L autoclave for preparing large amount of particles.


Fig. 2-2 1 L autoclave.

2.2.2 Equipment for tape-casting
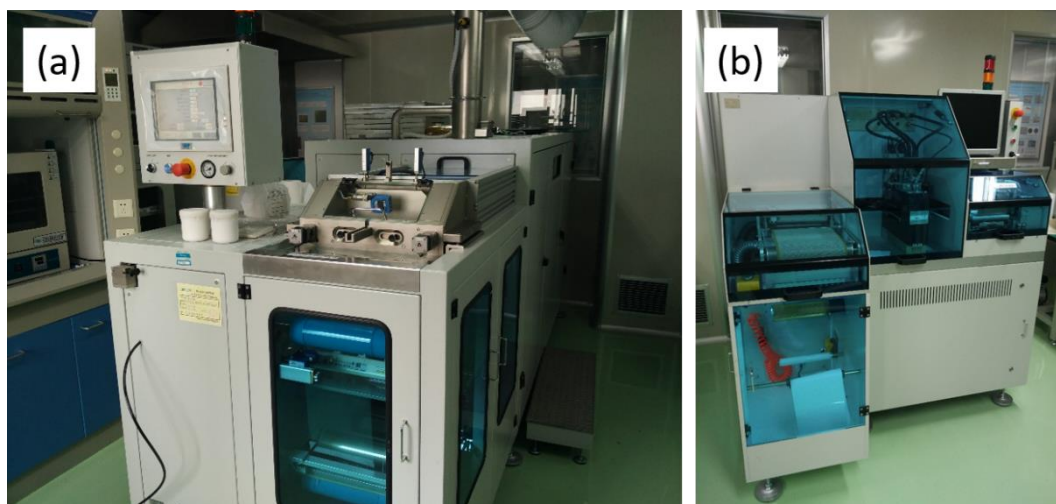
Fig. 2-3 (a) Tape-casting machine and (b) Punching and cutting machine

Tape-casting machine, Fig. 2-3a, with a number of different temperature heating and drying unit makes the slurry evenly coated on the carrier foil to form a thick film. Fig. 2-3b is punching and cutting machine. The thick film is cut into small pieces with the same size for subsequent laminating.
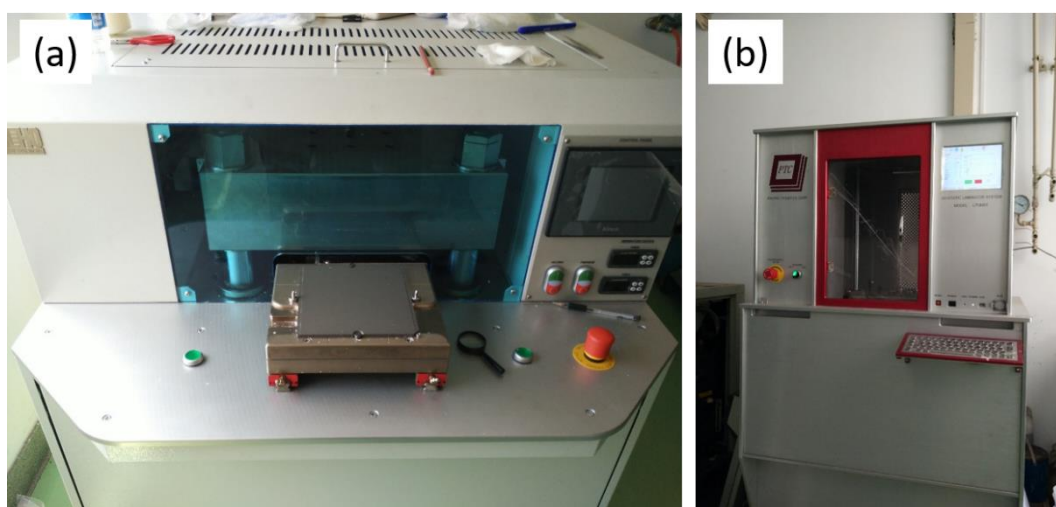
Fig. 2-4 (a) Laminating machine with heating unit and (b) Hot isostatic press machine

Laminating machine, Fig. 2-4, by setting the temperature and pressure the thick film could be separated. Under the heating situation the carrier foil could be take off

easily. Laminating the film piece by piece, green ceramic body with length of 15cm and thickness of 1.5 mm could be obtained. The green ceramic body is compacted by the hot isostatic press machine at 50 °C with a press of 50 MPa.
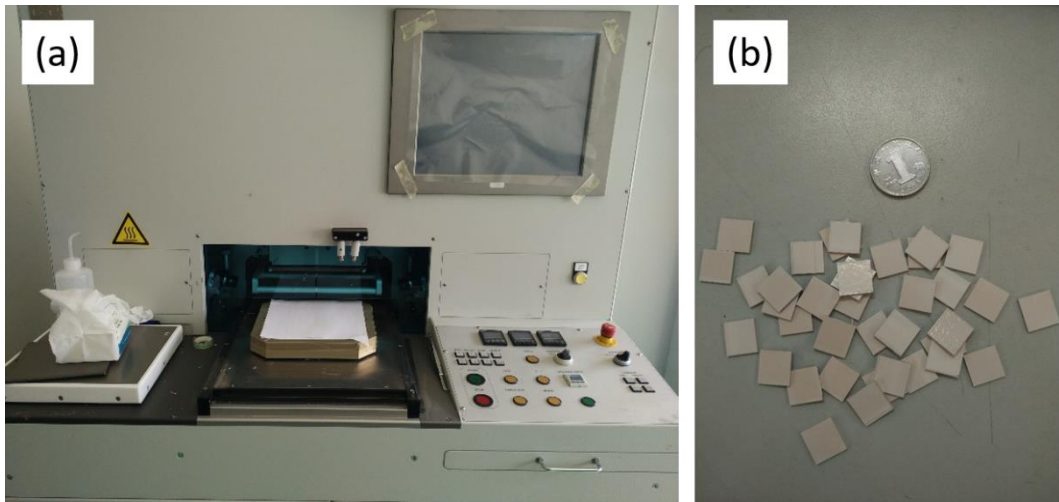
Fig. 2-5 (a) Cutting Machine and (b) Square samples with length of 1 cm.

The compacted ceramic green body is cut to a desired size evenly by cutting machine (Fig. 2-5). Square samples with length of 1cm and thickness of 1.2 mm are show in Fig. 2-5.

Before sintering, binder and other additives must be removed from the green body. In order to ensure no cracks appear, binder removal process is set to 1 °C/min to 600 °C and then keep for 1 h.

2.3 Characterization

2.3.1 X-ray diffraction analysis.

The crystal structure of the particles is identified by X-ray diffraction (XRD) (Model RINT 2200; Rigaku Corp., Tokyo, Japan) using CuKa radiation. This XRD instrument have a heating unit and could be used to characterize the process of phase transformation while temperature is increased.

Fig. 2-6 X-ray diffraction instrument.

2.3.2 Scanning electron microscopy analysis.

The morphology and microstructure of samples were characterized by scanning electron microscopy (SEM) (S-3000N, Hitachi Ltd., Tokyo, Japan). This SEM equipped with energy dispersive X-ray spectroscopy (EDX) is used to study the composition of particles. All the particle samples were sputter-coated with a thin Au or Pt film prior, which can increase electrical conductivity on the surface and prevent a charge that tends to decrease image clarity.

Fig. 2-6 Scanning electron microscope.

Chapter 3

MPB Slope Adjusted in BZ－KNN System

3.1 Introduction

Lead-based piezoceramics are most widely used in modern electronic devices. Since the 1950s, $PbZr_{1-x}Ti_xO_3$ (PZT) ceramics have drawn much attention because of their excellent piezoelectric properties. So widely used just because it has a nearly vertical tetragonal–rhombohedral morphotropic phase boundary (MPB). The dielectric and piezoelectric properties show their maximal values around the MPB composition. Due to this nearly vertical MPB [1], the PZT have a wide temperature-stability. Other high-performance Pb-based materials such as lead magnesium niobate-lead titanate (PMN–PT) and lead zinc niobate-lead titanate (PZN–PT) have a similar MPB [2]. However, these Pb-based ceramics with above 60 wt% Pb will be prohibited in the near future from many practical applications because of their toxicity during preparation and processing. Therefore, high-performance lead-free piezoceramics has attracted much attention in recent years.

Through the effort of many researchers in the past two decades, it was recognized that the $(K_{0.5}Na_{0.5})NbO_3$ (KNN) family and their derivatives are the most promising candidates, which have high piezoelectric coefficient and high Curie temperature [3-6]. In many reports, the orthorhombic-tetragonal or rhombohedral-tetragonal phase boundary has successfully been adjusted to room temperature with specially designed compositions, resulting in high piezoelectric properties at room temperature [7-11]. However, the properties deteriorate quickly when the temperature increase because of the temperature-unstable phase boundary [6,7]. Adjusting the MPB slope is an effective way to improve the temperature-stability. Z. Chen *et al.* [12] adjusted the ferroelectric–antiferroelectric (FE–AFE) phase boundary slope of $Pb(Zr_{0.95}Ti_{0.05})O_3$ (PZT95/5) system. After adding the antiferroelectric perovskite $PbSnO_3$, a vertical FE–AFE phase boundary was obtained. This suggest that the MPB slope could be adjust by adding the

third component.

R. Wang *et al.* [13] reported a negative-slope MPB in the BZ–KNN system. With temperature increase, the phase around the MPB transforms from rhombohedral to tetragonal then to cubic indicate that tetragonal phase is stable at high temperatures. Therefore, perovskite structure compound with rhombohedral phase could be used as third component for enhancing the rhombohedral phase at high temperatures, resulting in a change of MPB slope. In this work, rhombohedral perovskite component BNT was employed to adjust the slope of BZ–KNN system. A small amount of Li is added to increase the Curie temperature

3.2 Experimental procedure

(1-x-y)BZ–xKNLN–yBNT were prepared by a traditional solid-state reaction method. Ceramics stoichiometric of this ternary systems are shown in Fig. 3-1. Analytical reagent Na_2CO_3, K_2CO_3, Li_2CO_3, Nb_2O_5, $BaCO_3$, TiO_2, ZrO_2 and Bi_2O_3 were adopted as raw materials. In a typical synthesis, raw material powders were mixed by planetary ball milling with zirconia balls and ethanol for 4 h. After drying, the mixtures were compacted and calcined at 1000 $^{\circ}$C for 2 h. Then the calcined powders were crushed and ball-milled again for 10 h. The final powders were mixed with a few polyvinyl alcohol binder and then formed into disks with a diameter of 12 mm by pressing. After burning out the binder carefully, the disks were sintered at 1180 $^{\circ}$C for 4 h. The sintered disks were lapped to 1mm thickness and then coated silver-electrode on both surfaces at 600 $^{\circ}$C for 1 h, then poled in 130 $^{\circ}$C of silicone oil for 15 min with 1kV/mm. Flow diagram of solid-state reaction method was shown in Fig. 3-2.
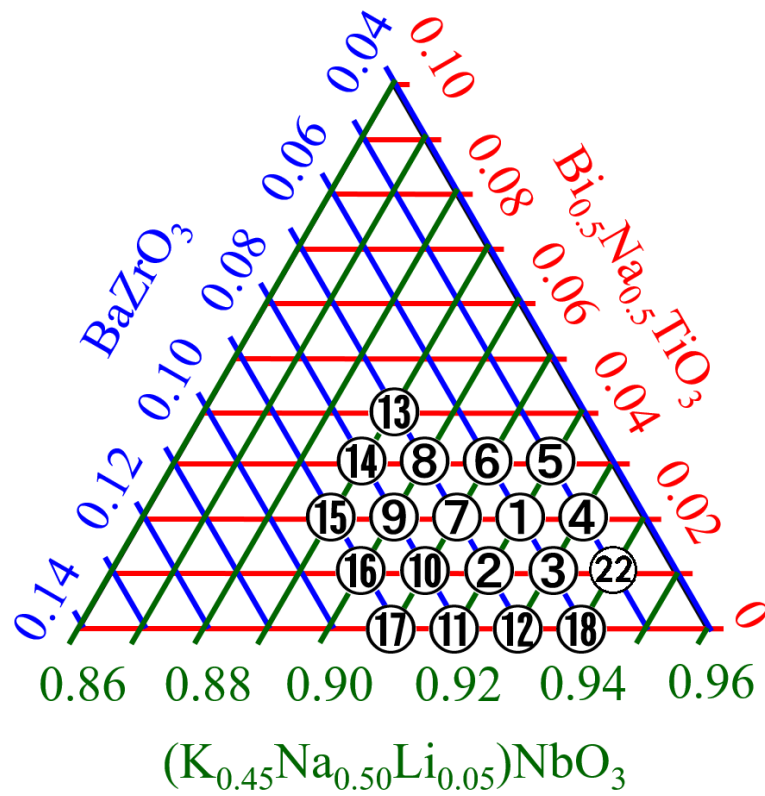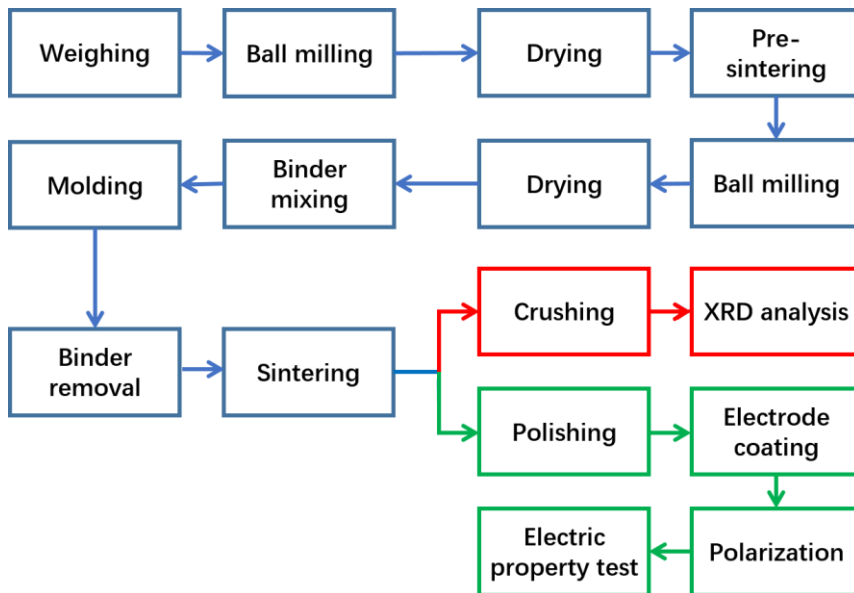
Fig. 3-1 Ternary compositions and sample number.


Fig. 3-2 Flow diagram of solid-state reaction method.

The phase was identified by X-ray diffraction (XRD) (Model RINT 2200; Rigaku Corp., Tokyo, Japan) using CuKa radiation. This XRD equipped with a heating unit was used to characterize the process of phase transformation while temperature was increased. Cubic, rhombohedral, tetragonal and orthorhombic phase of perovskite structure could be confirmed by the shape of $(200)_{pc}$ diffraction peak around 45°. The judgment method was shown in Fig. 3-3.

$(200)_{pc}$ diffraction peak around 45°	Shape	Phase
Single		Above T_c : Cubic, Under T_c : Rhombohedral
Double weak-left		Tetragonal
Double weak-right		Orthorhombic

**Fig. 3-3** Method for judging various phases of perovskite structure [14-16]

The T_c was determined at the peak value from the curve of the temperature dependence of the dielectric constant at 1 kHz. The electromechanical coupling factor k_p was measured by the resonance-antiresonance method, and the piezoelectric constant d_{33} measured by a d_{33}-meter using specimens with 10 mm diameter and 1mm thickness.

3.3 Results and discussion
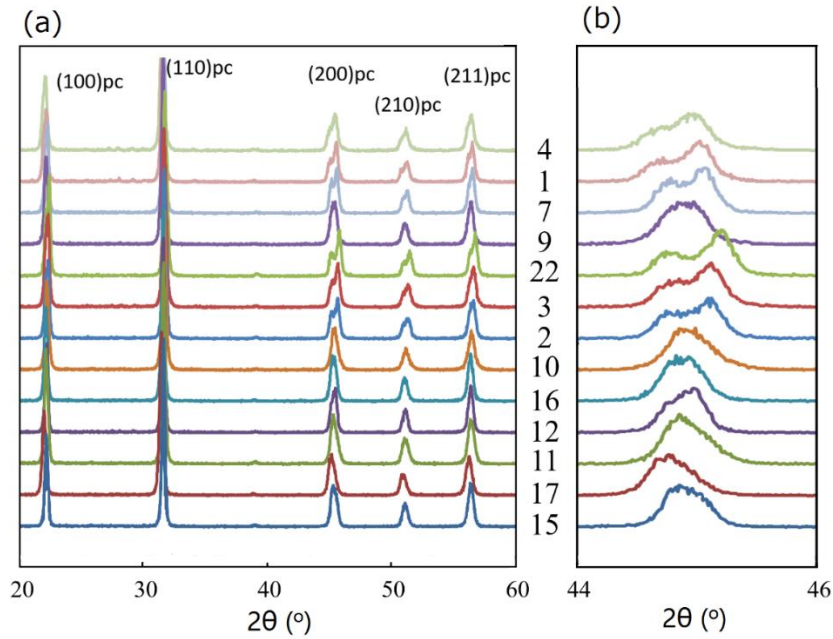
Fig. 3-3 XRD patterns of samples (a) from $2\theta = 20 - 60^o$; (b) Pseudocubic (200) peak.

XRD patterns shown in Fig. 3-3 indicate that all samples had a perovskite structure at room temperature. It was determined from the XRD patterns that sample 4, 1, 7, 22, 3, 2 had a tetragonal phase and sample 9, 10, 16, 12, 11, 17, 15 had a rhombohedral phase.
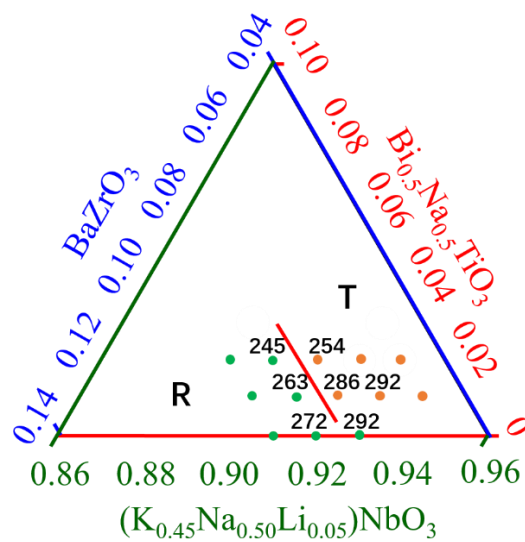
Fig. 3-4 Phase diagram. Solid line in the triangle shows the MPB and the numbers are Curie temperatures.

Fig. 3-4 shows the phase diagram, in which the solid line indicates the MPB. The numbers in Fig. 3-4 are the T_c of the samples. The T_c decreased with BZ or/and BNT increased in the system.
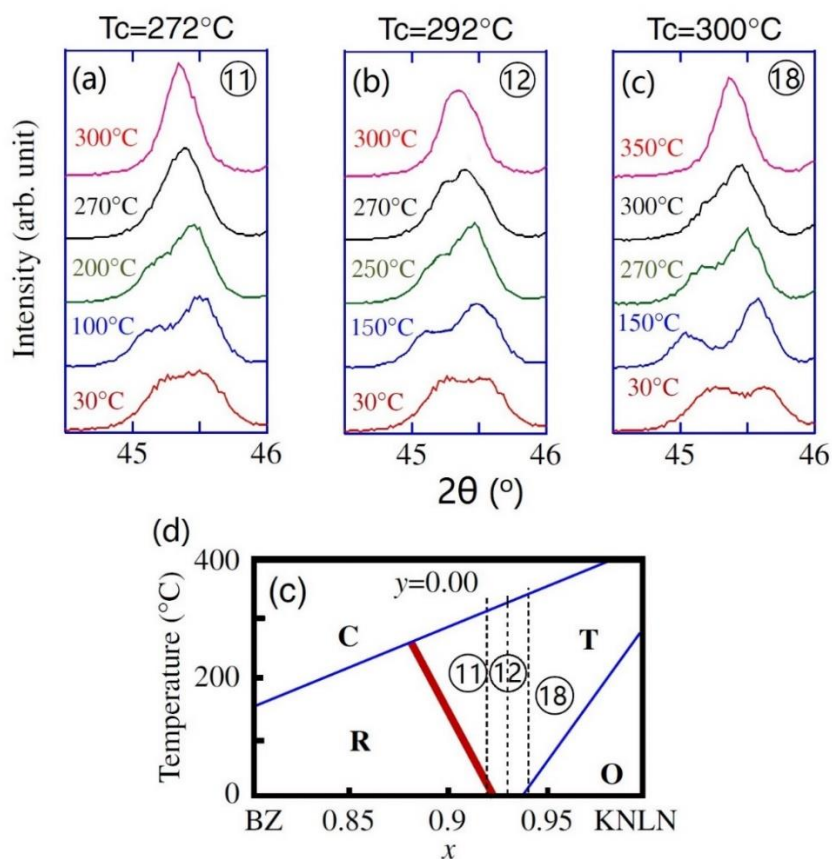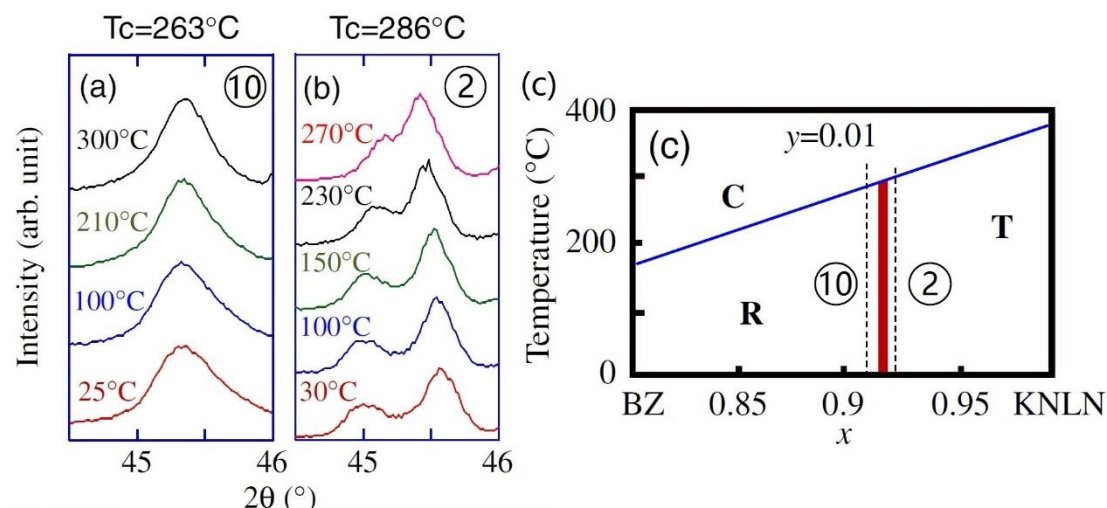

Fig. 3-5 (a-c) High-temperature XRD patterns of pseudocubic (200) peaks from sample 11, 12 and 18, respectively. (d) Schematic diagram of MPB slope with $y = 0$.

High temperature XRD analysis was used to investigate the slope of MPB, from room temperature to 300 °C in the range of $2\theta = 44.5$–$46°$. Sample 11 changed their phase from rhombohedral to tetragonal and then to cubic with temperature increased. Sample 18 shows orthorhombic phase at room temperature then transforms into tetragonal with just a little temperature increase. These results indicated tetragonal

phase was stable at high temperatures for these compositions. Fig. 3-5d shows diagram of the MPB for y = 0. The shape of MPB displays a negative-slope.

Fig. 3-6 (a), (b) High-temperature XRD patterns of pseudocubic (200) peaks from sample 10, 2. (c) Schematic diagram of MPB slope with y = 0.01.

The same measurements were carried out for other samples. Sample 10 and 2 changed their phase from rhombohedral and tetragonal to cubic, respectively, as shown in Fig. 3-4(a, b). It's worth noting that, the MPB is vertical, as shown in Fig. 3-6c.

Fig. 3-6 (a), (b) High-temperature XRD patterns of pseudocubic (200) peaks from sample 9, 7. (d) Schematic diagram of MPB slope with y = 0.02.
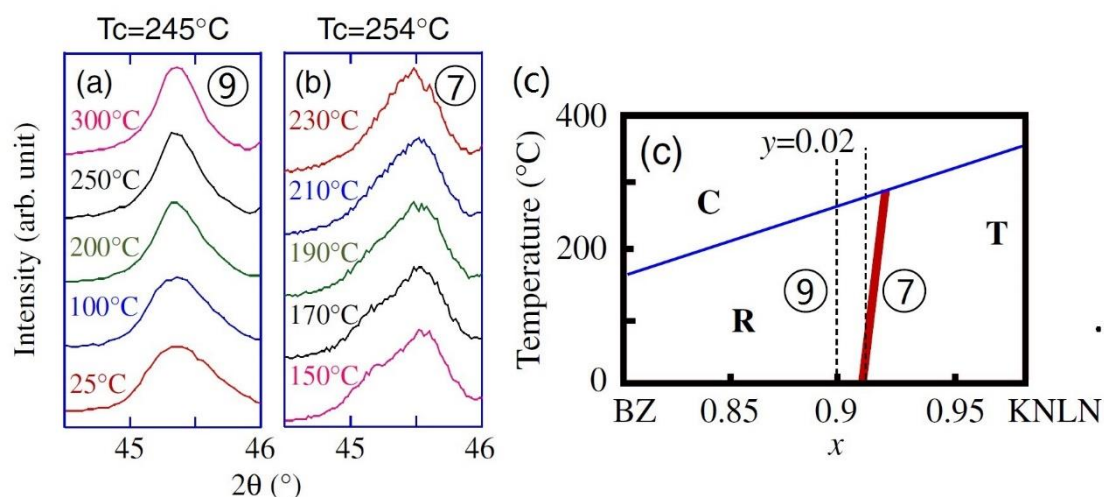
Fig. 3-5(a, b) shows phase change of sample 9 and 7. Sample 9 change its phase from rhombohedral to cubic with temperature increase. Sample 7 change its phase from

tetragonal to rhombohedral then to cubic. The MPB present positive-slope shape, as shown in Fig. 3-5(c).

Through increasing the third component BNT, the slope of MPB changed from negative to positive. This result verifies the existence of vertical MPB composition. Relationship between MPB slope and the amount of doped–BNT was shown in Fig. 3-7.
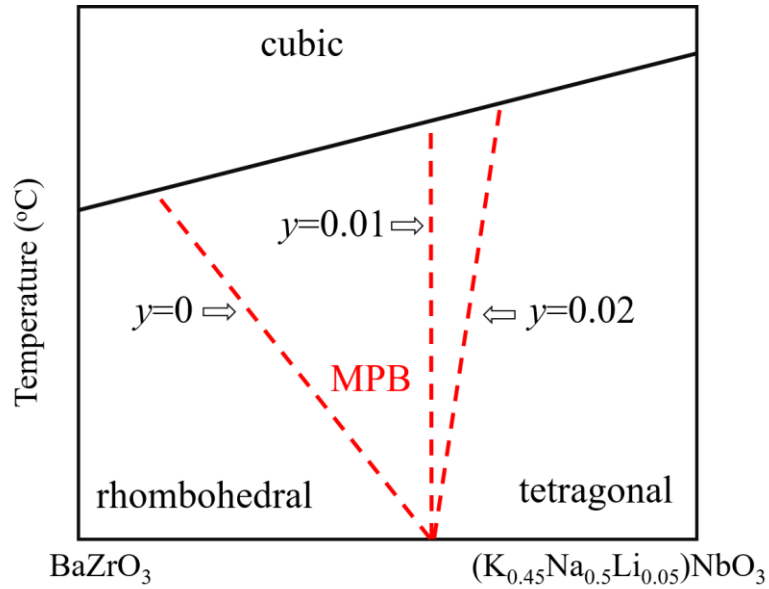
Fig. 3-7 The MPB slope change with BNT increase.

Sintering temperature and density of sample with vertical MPB composition are shown in Fig. 3-8. When the sintering temperature reached 1190 °C, sample with the highest density, 4.37 g/cm^3, could be obtained.
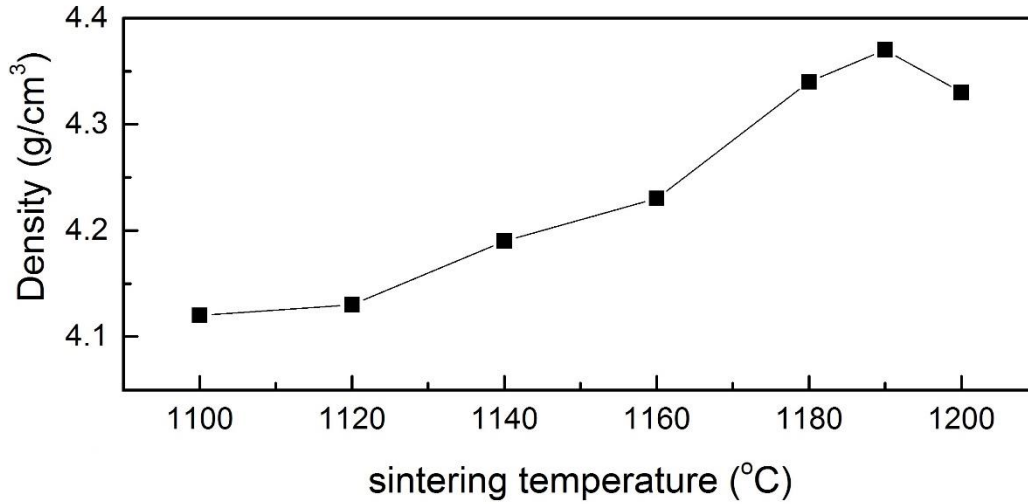
Fig. 3-8 Effects of sintering temperature on density.

Electric properties of the sample sintered at 1190 °C are also tested. The T_c of sample was 279 °C. The sample had a dielectric constant and loss (before poling) $\varepsilon_r = 1600$, $\tan\delta = 3.5\%$, $k_p = 42\%$, and $d_{33} = 285$ pC/N at room temperature.

3.4 Summary

MPB slope of KNLN–BZ system was adjusted from negative to positive by adding a small amount of the third component, BNT. A vertical MPB was formed when the addition amount of BNT was 1%. The vertical MPB composition, 0.075BZ–0.915KNLN–0.01BNT, with temperature-independent behavior has important practical value. The research method, using a stable rhombohedral perovskite component to adjust the negative MPB slope, indicates the possibility that the positive slope of MPBs could be made perpendicular to the composition axis by adding a stable tetragonal perovskite component as the third component in lead-free piezoceramic systems. The method provides a route for improving the performance with temperature stability of lead-free piezoceramics.

Reference

[1] Noheda, B., Cox, D. E., Shirane, G., Gonzalo, J. A., Cross, L. E., & Park, S. E. A monoclinic ferroelectric phase in the Pb $(Zr_{1-x}Ti_x)O_3$ solid solution. Applied Physics Letters, 74, 2059-2061, 1999.

[2] B. Noheda, D. E. Cox, G. Shirane, J. Gao, and Z.-G. Ye, Phase diagram of the ferroelectric relaxor $(1-x)PbMg_{1/3}Nb_{2/3}O_3-xPbTiO_3$, Phys. Rev. B, 66, 054104, 2002.

[3] Zheng, L., Huo, X., Wang, R., Wang, J., Jiang, W., & Cao, W. Large size lead-free $(Na,K)(Nb,Ta)O_3$ piezoelectric single crystal: growth and full tensor properties, CrystEngComm, 15, 7718, 2013.

[4] E. Hollenstein, M. Davis, D. Damjanovic and N. Setter. Piezoelectric properties of Li-and Ta-modified $(K_{0.5}Na_{0.5})NbO_3$ ceramics, Appl. Phys. Lett., 87, 182905, 2005.

[5] T. Shrout and S. Zhang, J. Lead-free piezoelectric ceramics: Alternatives for PZT?, Electroceram., 19, 113, 2007.

[6] Y. Xu, Q. Yu and J.-F. Li. A facile method to fabricate vertically aligned $(K,Na)NbO_3$ lead-free piezoelectric nanorods, J. Mater. Chem., 22, 23221, 2012.

[7] R. Wang, H. Bando, and M. Itoh. Universality in phase diagram of $(K,Na)NbO_3$-$MTiO_3(K,Na)NbO_3$-$MTiO_3$ solid solutions, Appl. Phys. Lett. 95, 092905, 2009.

[8] W. Liu and X. Ren. Large piezoelectric effect in Pb-free ceramics, Phys. Rev. Lett. 103, 257602, 2009.

[9] K. Yan, K. Matsumoto, T. Karaki, and M. Adachi. Microstructure and piezoelectric properties of $(K_{0.5}Na_{0.5})NbO_3$-$BaTiO_3$ lead-free piezoelectric ceramics modified by B_2O_3-CuO, J. Am. Ceram. Soc. 93, 3823, 2010.

[10] H. Birol, D. Damjanovic, and N. Setter. Preparation and characterization of $(K_{0.5}Na_{0.5})NbO_3$ ceramics, J. Eur. Ceram. Soc. 26, 861, 2006.

[11] Y. Hiruma, H. Nagata, and T. Takenaka. Grain-size effect on electrical properties of $(Bi_{1/2}K_{1/2})TiO_3$ ceramics, Jpn. J. Appl. Phys. 46, 1081, 2007.

[12] Z. Chen, J. Lian, and Y. Wang. Phase transition studies of PSZT ceramics with vertical ferro-antiferroelectric phase boundary. Ferroelectrics. 101, 225, 1990.

[13] R. Wang, H. Bando, M. Kidate, Y. Nishihara, and M. Itoh, Effects of A-site ions on the phase transition temperatures and dielectric properties of $(1-x)(Na_{0.5}K_{0.5})NbO_3$-$xAZrO_3$ solid solutions, Jpn. J. Appl. Phys. 50, 09ND10, 2011.

[14] A. W. Hewat. Soft modes and the structure, spontaneous polarization and Curie constants of perovskite ferroelectrics: tetragonal potassium niobate, J. Phys. C. 6, 2559, 1973.

[15] A. M. Glazer, S. A. Mabud, and R. Clarke. Powder profile refinement of lead zirconate titanate at several temperatures. I. $PbZr_{0.9}Ti_{0.1}O_3$, Acta Crystallogr. Sect. B. 34, 1060, 1978.

[16] R. Wa¨sche, W. Denner, and H. Schulz. Influence of high hydrostatic pressure on the crystal structure of barium titanate ($BaTiO_3$). Mater. Res. Bull. 16, 497-500, 1981.

Chapter 4

Hydrothermal Synthesis of Sodium Niobate

4.1 Introduction

In recent years, the application of lead-based piezoelectric ceramics has been limited for its harm to human health and pollution of the environment [1]. Consequently, lead-free piezoelectric ceramics have attracted much attention, especially potassium sodium niobate-based piezoelectric ceramics (KNN), which are considered to be the most promising substitute for lead zirconium titanate (PZT) for its high-performance piezoelectric properties [2,3]. To further improve the properties of KNN, researchers have assessed many methods, including doping elements [4-6], texture [7], and adjusting the morphotropic phase boundary slope [8]; the most well-known and effective method is the tape-casting texture technique first reported by Saito [7]. By adding the template particles and tape-casting treatment, the ceramic matrix orientated growth and properties were greatly improved. Appropriate size and oriented template particles are important factors of the method. KNN is characterized as having a high and narrow sintering temperature range [9]; therefore, the $NaNbO_3$ with a higher melting point of 1422 °C is more suitable than $KNbO_3$ with a melting point of 1050 °C as a proper material for template particles. The traditional method of preparing $NaNbO_3$ template particles is the molten salt method [10-12], which topochemically converts a layer-structured plate-like $Bi_{2.5}Na_{3.5}Nb_5O_{18}$ precursor in an NaCl flux. However, it is accompanied by disadvantages such as complicated operation and high energy consumption. Compared with the traditional method, the hydrothermal method is an effective approach to achieving metal oxides and hydroxides with some advantages such as low cost, low pollution and controllable morphology. In this study, $NaNbO_3$ particles with various types morphology were prepared by hydrothermal method. Effects of reaction conditions such as reaction temperature, time and concentration of OH^- on morphology were discussed.

4.2 Experimental procedure

Sodium hydroxide (NaOH, 97%), and niobium oxide (Nb$_2$O$_5$, 99.9%) were adopted as raw materials. In a typical synthesis, NaOH were dissolved in distilled water at a settled overall concentration between 2 and 16 M. Then, 0.5 g of Nb$_2$O$_5$ was added to the above solution and stirred for 30 min, resulting in a suspension. The suspension was placed in a 50-mL Teflon-lined autoclave with a filling factor of approximately 80 vol%. The autoclave was heated at different temperature for a period between 2 and 8 h to yield white particles. After cooling, the white precipitations were repeatedly washed with deionized water before drying at 80°C. Some of the particles were further calcined at 600°C to examine their phase and microstructure in detail before and after calcination.

The crystal structure of the particles was identified by X-ray diffraction (XRD) (Model RINT 2200; Rigaku Corp., Tokyo, Japan) using CuKa radiation. The morphology and microstructure of the as-prepared particles were characterized by scanning electron microscopy (SEM) (S-3000N; Hitachi Ltd., Tokyo, Japan). The thermal stability of the particles was tested by thermogravietric analysis (TGA) and differential thermal analysis (DTA) (Thermo Plus 2, Rigaku corporation, Japan).
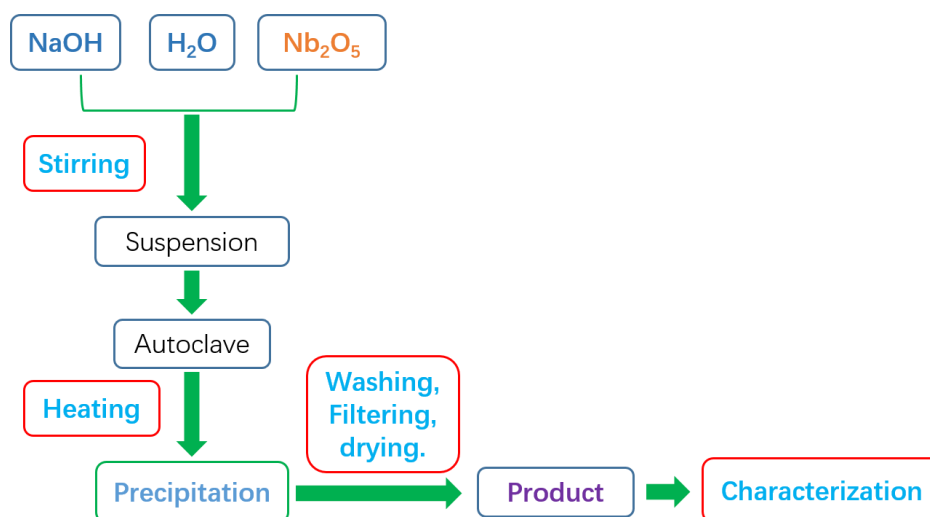
Fig. 4-1 Flow diagram of hydrothermal synthesis.

4.3 Results and discussion

4.3.1 Effect of reaction temperature
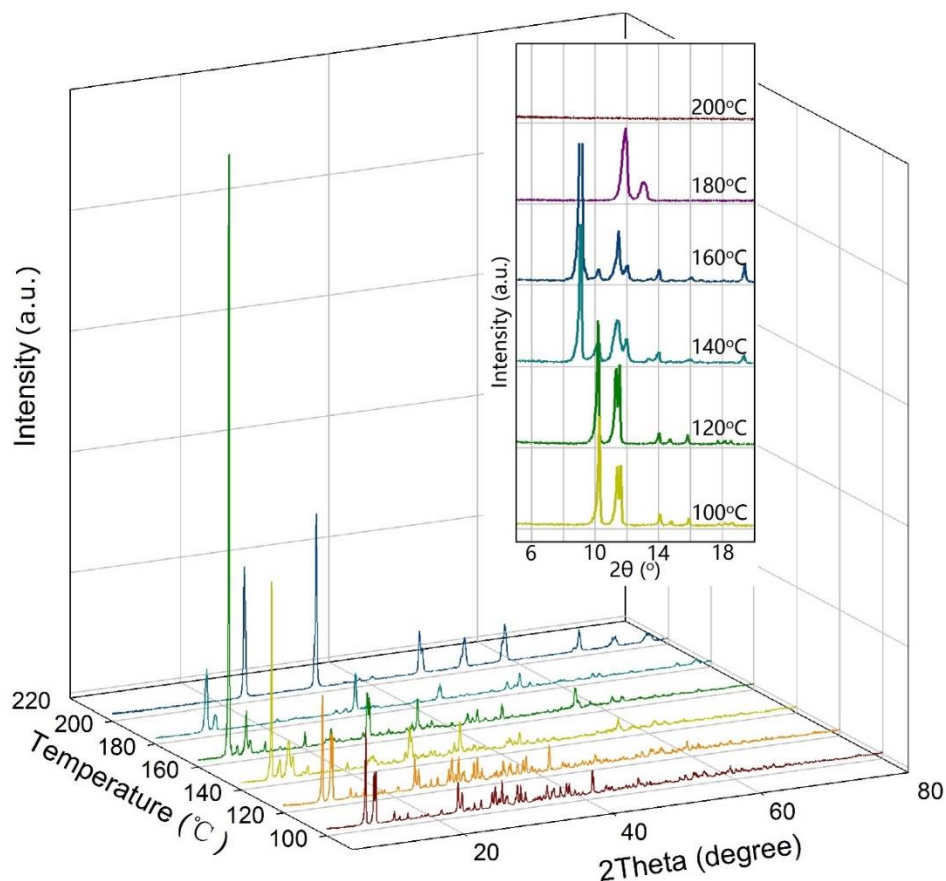
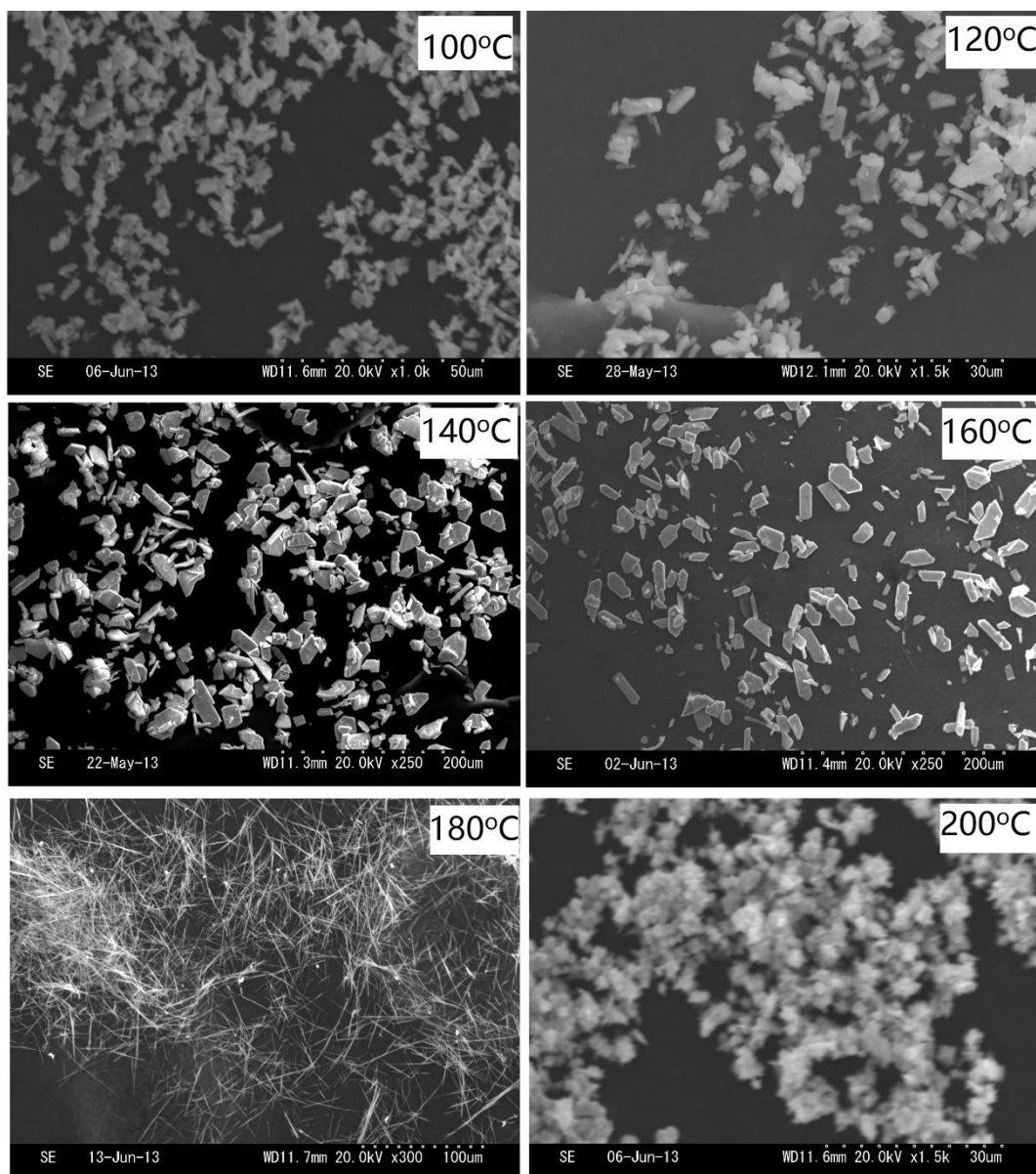**Fig. 4-2** XRD patterns of particles obtained at different temperatures
and (inset) patterns details from 5 to 20°.

Figure 4-2 shows XRD patterns of particles obtained for 3 h in 12 mol/L of NaOH at different reaction temperatures. The XRD patterns matched $Na_8Nb_6O_{19} \cdot 13H_2O$ [13] (JCPDS Card NO. 14-0370) at 100 °C and 120 °C. From 140 °C to 160 °C, the strongest diffraction peak appeared at $2\theta = 9°$, but no standard data could be matched. As the reaction temperature rose to 180 °C, the main product is $Na_2Nb_2O_6 \cdot H_2O$ [14] which has a fiber morphology and monoclinic lattice. The particles obtained at 180 °C are a metastable intermediate of this reaction, and they completely convert to the final product $NaNbO_3$ cubes at 200 °C.

Fig. 4-3 SEM images of particles obtained at different temperatures.

SEM images of particles obtained at different temperatures were shown in Fig. 4-3. The Nb_2O_5 powder aggregated first to irregular bars below 120 °C, and then turn to plate-like morphology with a width of 35 μm and a thickness of 3 μm at 140 °C. When temperature was 180 °C, the morphology of particles turned to fibrous with an aspect ratio. The fibers completely converted to the final cubic morphology at 200 °C. The morphology evolution of particles with the increase of reaction temperature is shown in Fig. 4-4.
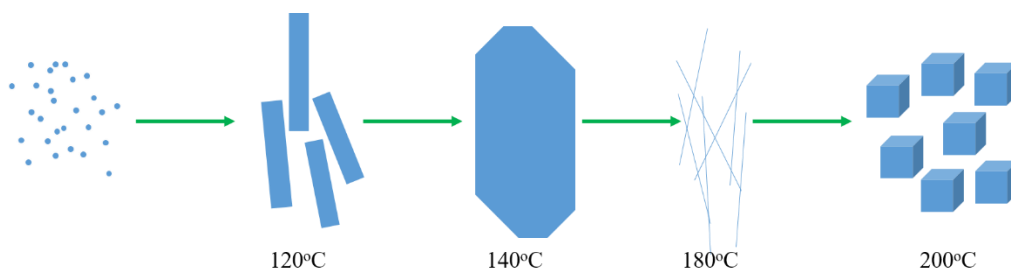
Fig 4-4 Morphology evolution of particles with the increase of reaction temperature.

4.3.2 Effect of reaction time
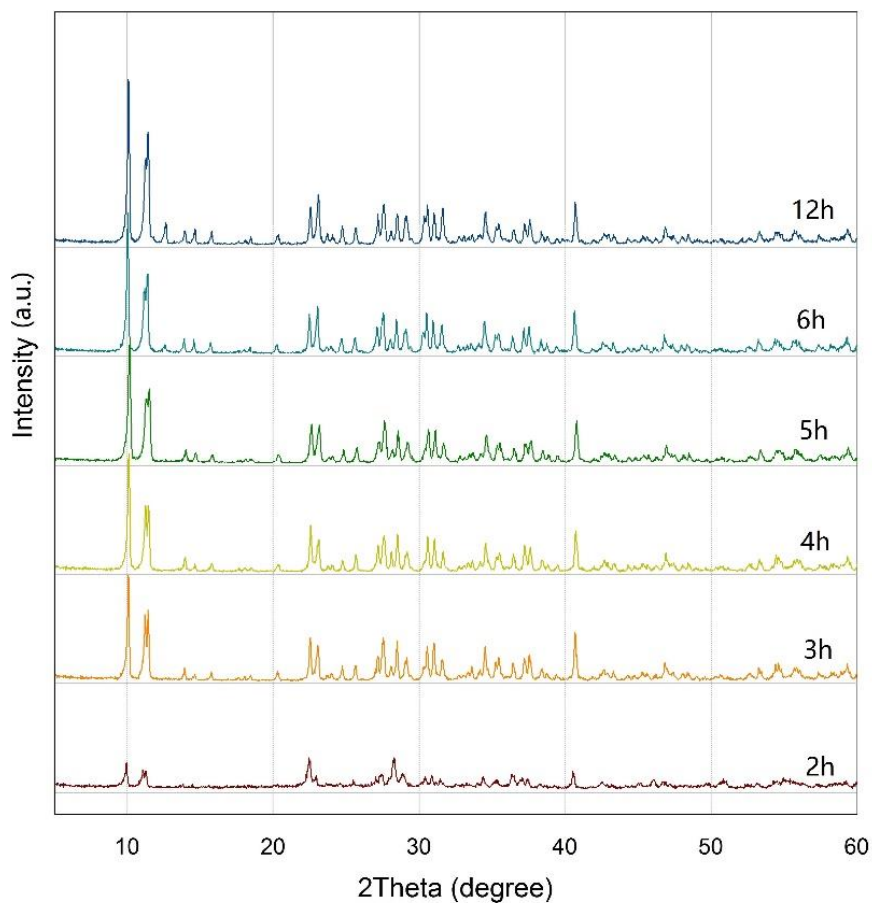
Fig. 4-5 XRD patterns of particles obtained at different times.

XRD patterns of particles obtained at 140 °C for different times were shown in Fig. 4-5. The weak diffraction peak intensity of the particles obtained at 2 h indicate that the

crystallinity of the patrticles was not high and the reaction time was not enough. When the reaction time was above 3 h, no difference could be observed by the XRD patterns indicated that 3 hours is enough for this reaction.
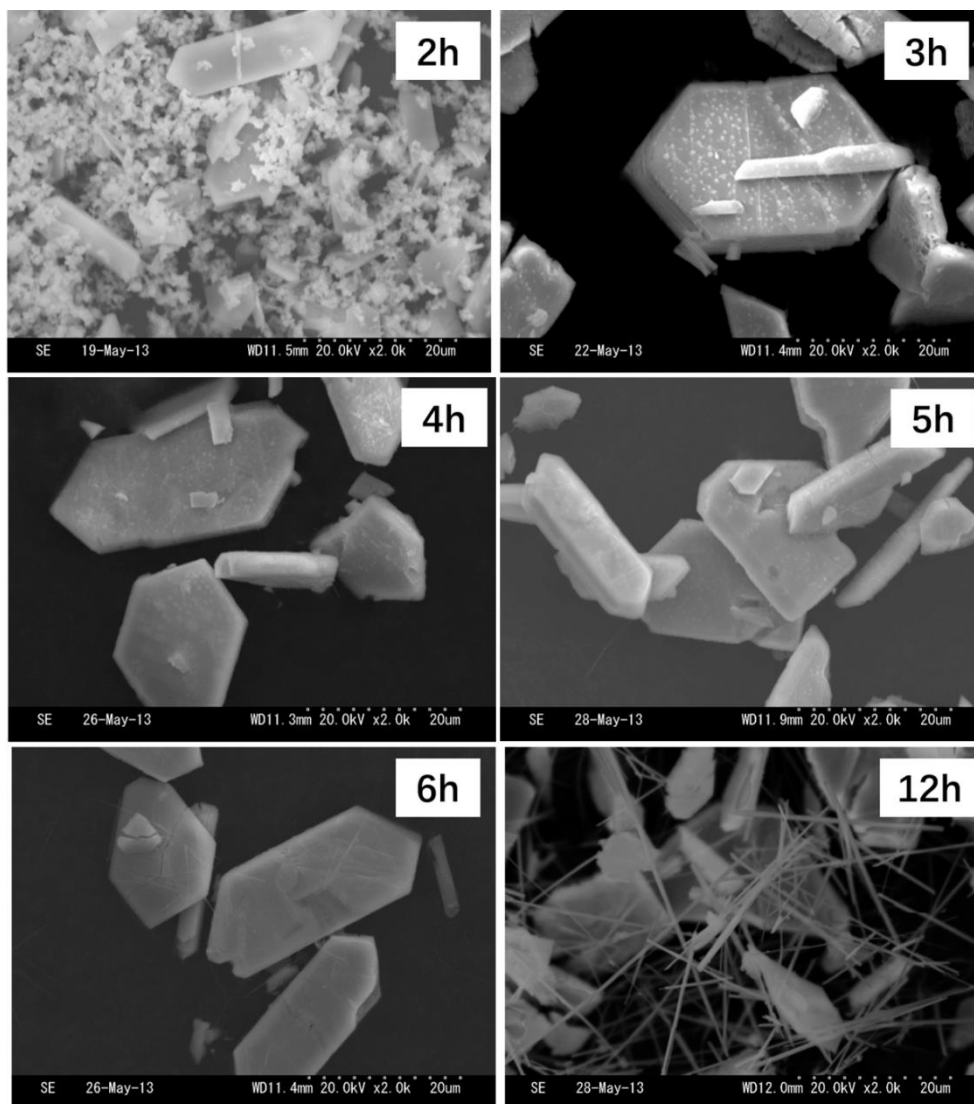

Fig. 4-6 SEM images of particles obtained at different times.

SEM images of particles obtained at different reaction times were shown in Fig. 4-6. When the reaction time is 2h, the particles are mixture without regular morphology indicated that the reaction has not completed. This was consistent with the above XRD results. For 3 h to 6 h, plate-like morphology particles were obtained. It is noteworthy that the particles broke into needle-like when the reaction time reached 12 h. Therefore, too long reaction time is not suitable for the synthesis of plate-like morphology and 3 hours is a more appropriate reaction time.

4.3.3 Effect of NaOH concentration
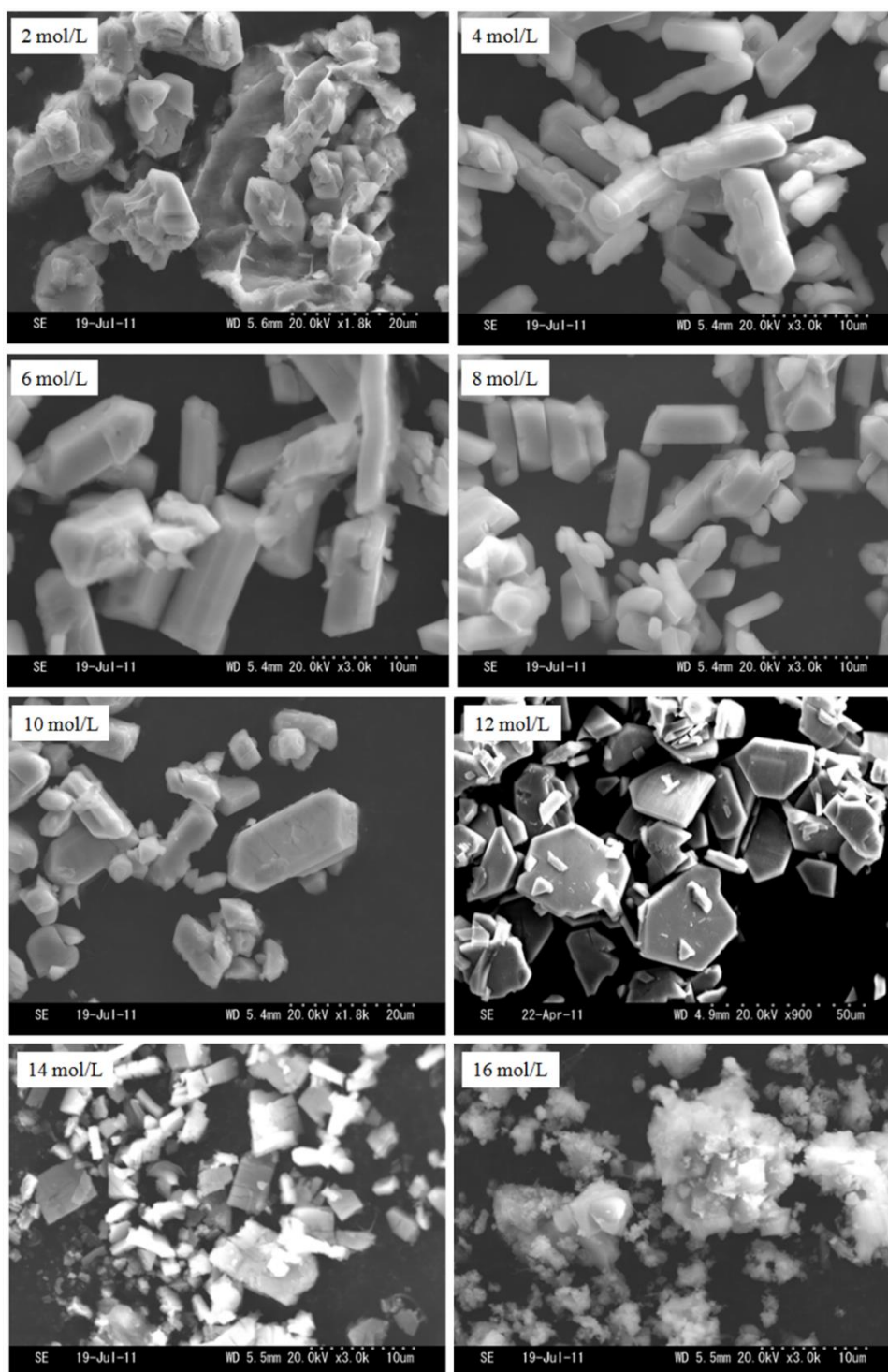
Fig. 4-7 SEM images of particles obtained in different NaOH concentration.

SEM images of particles obtained in different NaOH concentration were shown

in Fig. 4-7. The NaOH concentration was an important factor for controlling the morphology. When the concentration of NaOH was 2 mol/L, the morphology of the particles was irregular. The powder mainly presented the stick shape at a NaOH concentration of 4–10 mol/L. The NaOH concentration increased to 12 mol/L, plate-like morphology could be observed. With the mineralizer concentration increased to 14 mol/L, the morphology of the particles became irregular. Therefore, 12 mol/L is the optimal concentration for preparing the plate-like morphology.

As the template particles for fabricating the oriented ceramic, morphology of particles should be plate-like and needle-like. To summarize, reaction temperature 140 °C, time 3 h, and 12 mol/L of NaOH were the best conditions for prepared the plate-like particles. The fibrous NN particles could be obtained if the reaction temperature increase to 180 °C.

From all of the above results, a plausible formation mechanism of this system is shown as follows. As temperature is raised, the thermal active energy promotes the acceleration of the reaction and the transformation from the intermediates to the final products. The reaction initially ruptures the corner-sharing of the niobium-oxygen polyhedra in Nb_2O_5, yielding intermediates with edge-sharing octahedra. Therefore, the first step reaction is rupturing the corner-sharing between NbO_6 octahedra:

$$3Nb_2O_5 + 8OH^- \rightarrow Nb_6O_{19}^{8-} + 4H_2O, \tag{1}$$

Then, the $Nb_6O_{19}^{8-}$ reacted with metal cation and yielded $Na_8Nb_6O_{19} \cdot 13H_2O$:

$$Nb_6O_{19}^{8-} + 8Na^+ + 13H_2O \rightarrow Na_8Nb_6O_{19} \cdot 13H_2O, \tag{2}$$
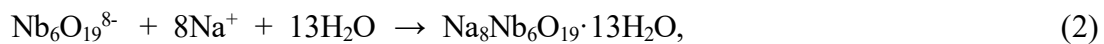
With the increase of temperature, $Na_8Nb_6O_{19} \cdot 13H_2O$ gradually dehydrated, and the degree of dehydration was closely related to the temperature. Particles with plate-like morphology were obtained by dehydration before 160 °C. When the reaction temperature reached 180 °C, $Na_2Nb_2O_6 \cdot H_2O$ was formed, and the reaction can be expressed as:

$$Na_8Nb_6O_{19} \cdot 13H_2O \rightarrow 3Na_2Nb_2O_6 \cdot H_2O + 2Na^+ + 2OH^- + 9H_2O. \tag{3}$$

The structure of the $Na_2Nb_2O_6 \cdot H_2O$ is metastable and a stable structure of $NaNbO_3$ forms at the expense of the fibers in the final stage of the reaction:

$$Na_2Nb_2O_6 \cdot H_2O \rightarrow 2NaNbO_3 + H_2O. \tag{4}$$

4.3.4 Phase and morphology of particles after annealing treatment.
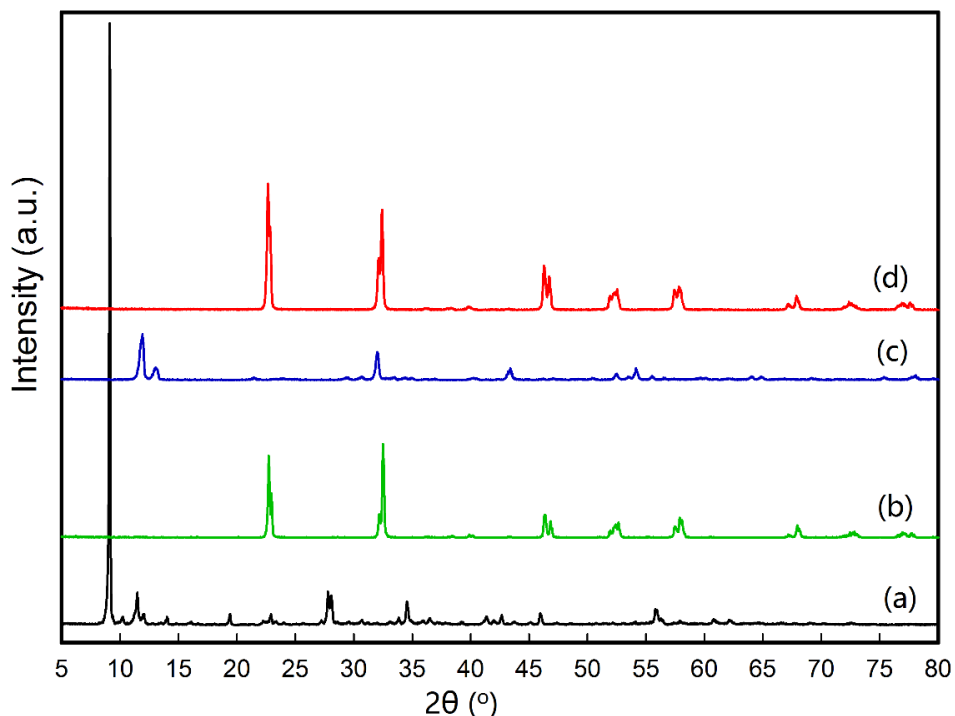
Fig. 4-8 (a) XRD patterns of plate-like NN; (b) plate-like NN after annealing treatment; (c) XRD patterns of fiber NN; (d) fiber NN after annealing treatment

For further application, the phase and morphology should be confirmed. After annealing treatment at 600 °C, the plate-like NN and fiber NN both turned in to perovskite structure as shown in Fig. 4-8. The morphology can still remain constant as shown in Fig. 4-9.
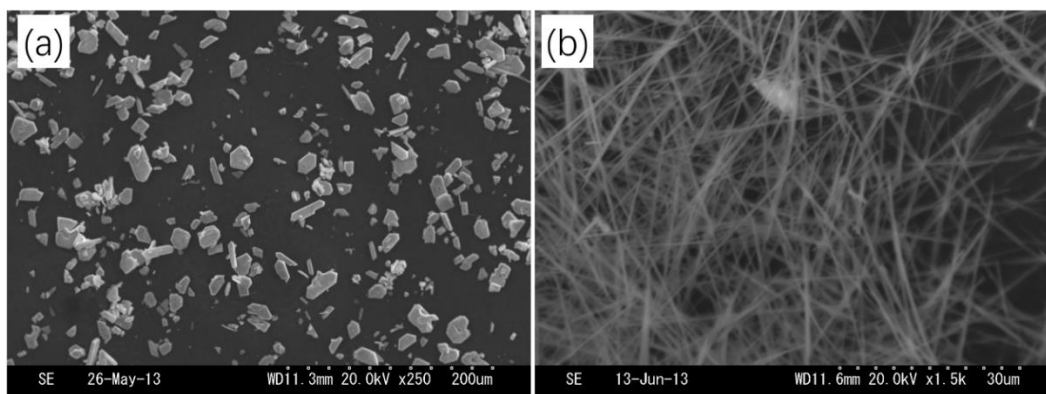
Fig. 4-9 SEM images of different morphology particles after annealing treatment; (a) plate-like NN and (b) fiber NN.

4.3.5 Thermal analysis
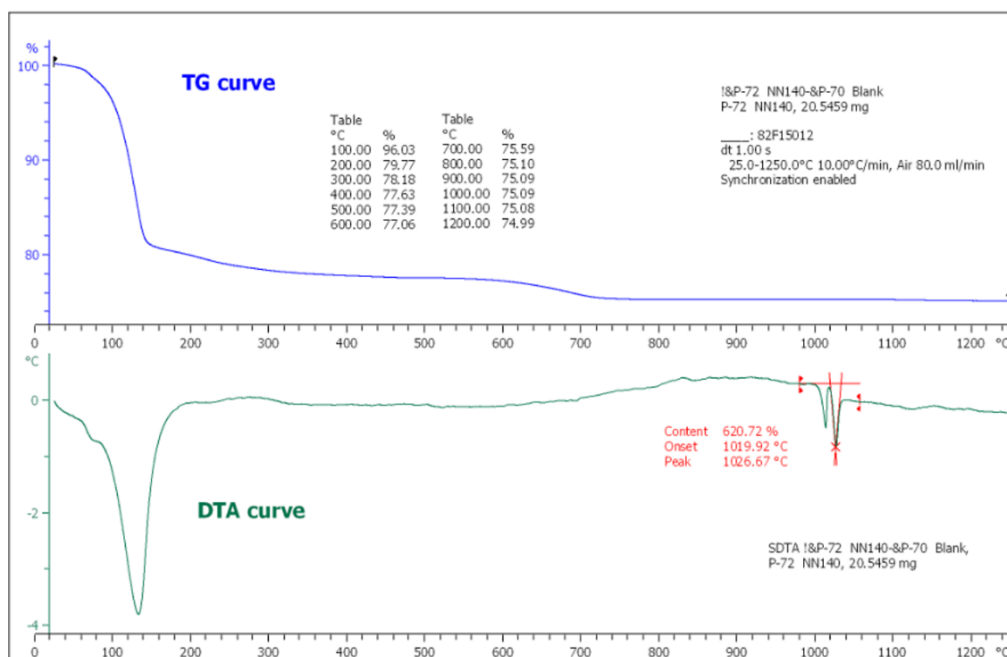
Fig. 4-10 TG and DTA curve of plate-like sodium niobate hydrate particles

obtained at 140 °C for 3 h in 12 mol/L NaOH.

DTA and TG analysis of the plate-like particles obtained at 140 °C was shown in Fig. 4-10. An endothermic peak appeared at 150 °C by the DTA, and the TG revealed total weight loss of approximately 18 wt%. It was indicating the combined water-loss of the particles. However, the endothermic peak appeared around 1000 °C indicated the melting point of the particles was around 1000 °C. For common sintering of KNN-based ceramic, this melting point was too low. The particles could only be used in low temperature sintering below 1000 °C.

4.4 Summary

$NaNbO_3$ particles with different morphology were synthesized by hydrothermal method. Plate-like morphology particles with a width of 35 μm and a thickness of 3 μm and fibrous morphology particles with an aspect ratio were obtained as expected morphology.

Through investigating the hydrothermal conditions such as reaction time, temperature and NaOH concentration on the phase and morphology of the particles, process of crystal growth was conjectured. The plate-like NN particles were grown form the strip-like $Na_8Nb_6O_{19} \cdot 13H_2O$ through dehydration and rearrangement with the increase of temperature. The optimal hydrothermal conditions for preparing plate-like morphology were confirmed as 140 $^{\circ}$C, 3 h and 12 mol/L of NaOH. Fibers NN particles with an aspect ratio could be obtained with further increase of temperature to 180 $^{\circ}$C.

After annealing treatment at 600 $^{\circ}$C, the plate-like NN and fiber NN both turned in to perovskite structure without morphology change. However, the melting point of the plate-like particles confirmed by TG-DTA analysis was around 1000 $^{\circ}$C. This limited the particles could only be used in low temperature sintering below 1000 $^{\circ}$C.

References

[1] EU-Directive 2002/95/EC: Restriction of the use of certain hazardous substances in electrical and electronic equipment (RoHS), Official Journal of the European Union, 46[L37] 19-23, 2003.

[2] E. Cross, Lead-free at last, Nature, 432, 24-25, 2004.

[3] J. Tellier, B. Malic, B. Dkhil, D. Jenko, J. Cilensek and M. Kosec, Crystal structure and phase transitions of sodium potassium niobate perovskites, Solid State Sci., 11, 320-324, 2009.

[4] Y. Guo, K. Kakimoto, and H. Ohsato, $(Na_{0.5}K_{0.5})NbO_3$-$LiTaO_3$ lead-free piezoelectric ceramics, Mater Lett., 59, 241-244, 2005.

[5] S. Y. Chu, W. Water, Y. D. Juang, and J. T. Liaw, Properties of $(Na, K)NbO_3$ and $(Li, Na, K)NbO_3$ ceramic mixed systems, Ferroelectrics, 287, 23-33, 2003.

[6] J. Kroupa, J. Petzelt, B. Malic, and M. Kosec, Electro-optic properties of KNN-STO lead-free ceramics, J. Phys. D. Appl Phys., 38, 679, 2005.

[7] Y. Saito, H. Takao, T. Tani, T. Nonoyama, K. Takatori, T Homma, T. Nagaya and M. Nakamura, Lead-free piezoceramics, Nature, 432, 84, 2004.

[8] T. Karaki, T. Katayama, K. Yoshida, S. Maruyama and M. Adachi, Morphotropic phase boundary slope of $(K,Na,Li)NbO_3$-$BaZrO_3$ binary system adjusted using third component $(Bi,Na)TiO_3$ additive, Jpn. J. Appl. Phys., 52, 09KD11, 2013.

[9] Y. Zhen and J. F. Li, Normal sintering of $(K,Na)NbO_3$-based ceramics: Influence of sintering temperature on densification, microstructure, and electrical properties, J. Am. Ceram Soc., 89, 3669-3675, 2006.

[10] M. Cao, W. Wang, F. Li, H. Hao, Z. Yu and H.X. Liu, Structure control of $NaNbO_3$ template for textured ceramics synthesized by two-step molten salt method, Ferroelectrics, 404, 39-44, 2010.

[11] S. F. Poterala, Y. F. Chang, T. Clark, R. J. Meyer, Jr, and G. L. Messing, Mechanistic interpretation of the aurivillius to perovskite topochemical microcrystal conversion process, Chem. Mater., 22, 2061-2068, 2010.

[12] Y. Saito, H. Takao, Synthesis of polycrystalline platelike $NaNbO_3$ particles by the

topochemical micro-crystal conversion from $K_4Nb_6O_{17}$ and fabrication of grain-oriented $(K_{0.5}Na_{0.5})NbO_3$ ceramics, J Electroceram, 24, 39-45, 2010.

[13] S. Y. Wu, W. Zhang, X. M. Chen, Formation mechanism of $NaNbO_3$ powders during hydrothermal synthesis, Mater Electron, 21, 450-455, 2010.

[14] H. Zhu, Z. Zheng, X. Gao, Y. Huang, Z. Yan, J. Zou, H. Yin, Q. Zou, Scott H. Kable, J. Zhao, Y. Xi, W. N. Martens, and R. L. Frost, Structural evolution in a hydrothermal reaction between Nb_2O_5 and NaOH solution: From Nb_2O_5 grains to microporous $Na_2Nb_2O_6 \cdot 2/3H_2O$ fibers and $NaNbO_3$ cubes, J. Am. Chem. Soc., 128, 2373-2384, 2006.

Chapter 5
Morphology Control and Phase Transition of Hexagonal Sodium Niobate Particles

5.1 Introduction

In the previous chapter, although plate-like $NaNbO_3$ particles were prepared, it could only be used for low temperature sintering below 1000 °C. For the low temperature sintering of KNN-based ceramics, the usual practice is to add sintering aids such as CuO, $K_4CuNb_8O_{23}$, and ZnO [1-3]. However, the adding of sintering aids tend to sacrifice T_c or d_{33}. Therefore, $NaNbO_3$ particles with high melting point is expected to be synthesize. In previous work, $K_4Na_4Nb_6O_{19} \cdot 9H_2O$ with plate-like morphology was prepared [4]. In this work, through adjusting synthesis conditions of the previous work, hexagonal $NaNbO_3$ with plate-like morphology was prepared by the hydrothermal method. Effects of reaction conditions such as reaction time, concentration of OH^-, and K^+: Na^+ ratio on morphology are discussed. The phase and morphology of the powders after calcination treatment are also investigated.

5.2 Experimental procedure

Potassium hydroxide (KOH, 85%), sodium hydroxide (NaOH, 97%), and niobium oxide (Nb_2O_5, 99.9%) were adopted as raw materials. In a typical synthesis, KOH and NaOH were dissolved in distilled water at a settled overall concentration between 0.5 to 1.5 mol/L with a designed K^+: Na^+ ratio. Then, 0.5 g Nb_2O_5 and appropriate surfactant were added to the above solution and stirred for 30 min, resulting in a suspension. The suspension was placed in a 50-mL Teflon-lined autoclave with a filling factor of approximately 80 vol%. The autoclave was heated at 200 °C for a period between 2–8 h to yield white particles. After cooling, the white precipitations were repeatedly washed with de-ionized water before drying at 80 °C. Some of the particles were further calcined at 600 °C to examine their phase and microstructure in detail

before and after calcination.

The crystal structure of the particles was identified by X-ray diffraction (XRD) (Model RINT 2200, Rigaku Corp., Japan) using Cu Kα radiation. An XRD equipped with a heating unit was used to characterize the process of phase transformation while temperature was increased. The morphology and microstructure of the as-prepared particles were characterized by scanning electron microscopy (SEM) (S-3000N, Hitachi Ltd., Tokyo, Japan). An SEM equipped with energy dispersive X-ray spectroscopy (EDX) was used to study the composition of particles. Electron back-scattered diffraction (EBSD) analysis was used to study the orientation of the particles.
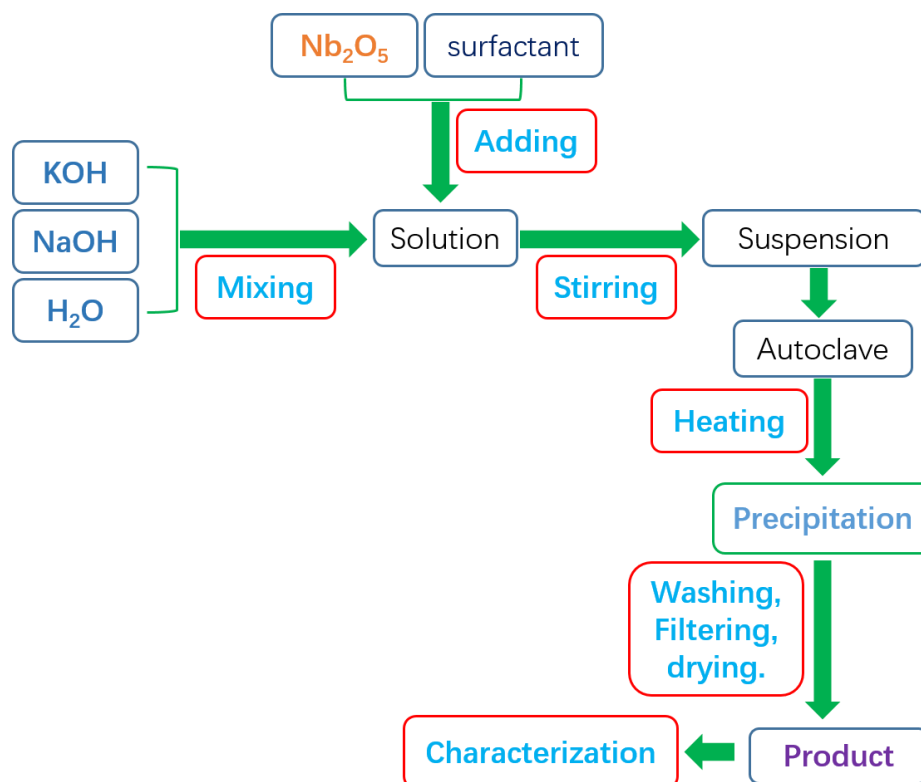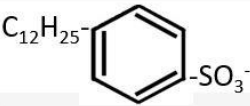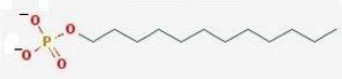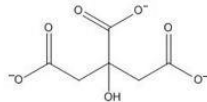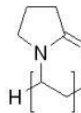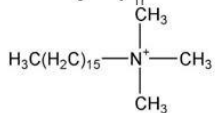

Fig. 5-1 Flow diagram of hydrothermal synthesis.

5.3 Preparation and morphology control of ilmenite NaNbO$_3$

5.3.1 Effect of surfactant on the morphology

Surfactants are often used in hydrothermal processes to adjust the morphology of product. Chunxia Li *et al*. [5] prepared β-NaLuF$_4$ microplates by trisodium citrate (Cit^{3-}) assisted. Xiao Li Zhang [6] prepared ZnO particles with different morphology by adding SDBS. In this work, in order to more effectively control the morphology of the product, different types of surfactants were used. Surfactants used in the experiment were listed in Table 5-1.

Table 5-1 Surfactant used in experiment.

Type	Reagent	Abbreviation	Effective group
Anionic	Sodium dodecyl benzene sulfonate	SDBS	
	Dodecyl Phosphate	DP	
	Citric Acid	CA	
Nonionic	Polyvinyl pyrrolidone	PVP	
Cationic	Hexadecyl trimethyl ammonium Bromide	CTAB	
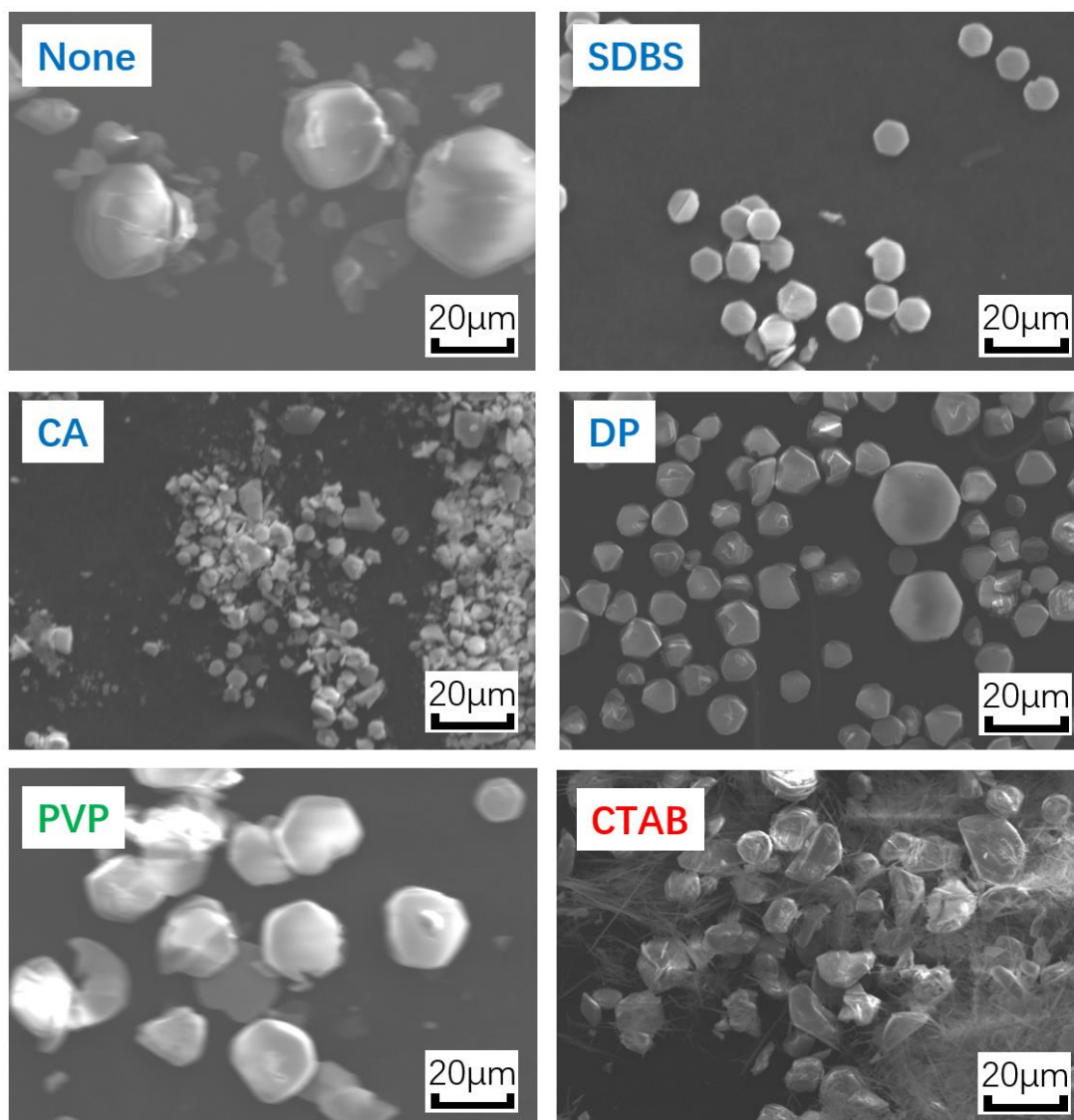
Fig. 5-2 SEM images of particles obtained by adding different surfactant.

Fig. 5-2 shows the SEM images of particles obtained with different surfactant. Particles obtained without adding surfactant mainly shows plate-like morphology with a diameter of 25 μm. But there are many small particles without uniform morphology exist. Adding SDBS make particle size becomes smaller and the morphology becomes more uniform. Adding CA make particles too small to use as template particles. Particles with well dispersibility could be obtained by adding DP, but disadvantages are obvious such as non-uniform particles size and smaller aspect ratio. The regularity of particles is only a little improvement by adding nonionic surfactant PVP. Cationic

surfactant CTAB acts as a barrier to the formation of plate-like morphology.

In conclusion, the anionic surfactant SDBS is suitable for the system. Through adding SDBS, particles with well dispersibility and uniform size could be obtained. When SDBS is introduced into the reaction system, it can selectively adsorb on different crystallographic facets, resulting in the modification of the surface free energy of the individual crystallographic faces and leading to the formation of anisotropic microplates. The dominant adsorption of SDBS on the {0001} facets lowers the surface energy of these facets and drives the growth of the nuclei along the [001] direction. Function mechanism of SDBS in this system was shown in Fig. 5-3.
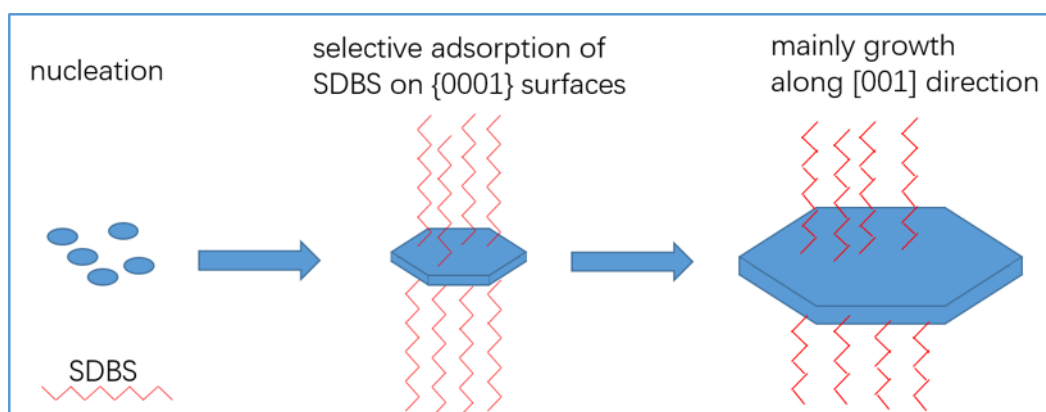

Fig. 5-3 Function mechanism of SDBS in this system.

5.3.2 Effect of reaction temperature
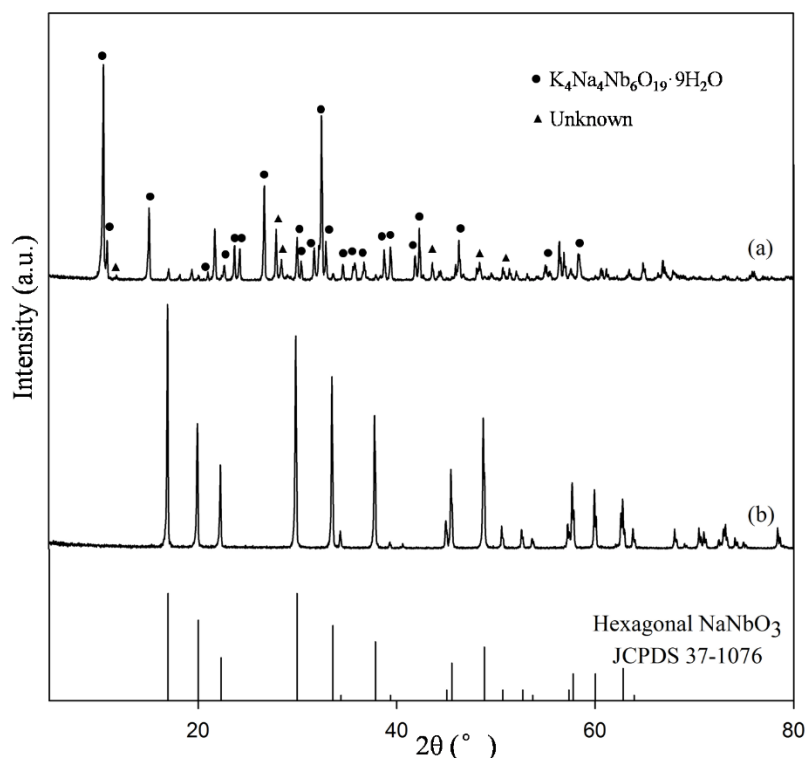
Fig. 5-4 XRD patterns of powders synthesized for 8h in $[OH^-]$ = 1.0 mol/L with different reaction temperature

(a) 180 ^oC; (b) 200 ^oC and the standard diffraction data of hexagonal $NaNbO_3$ (JCPDS Card No. 33-1270).

Fig. 5-4 shows the XRD patterns of powders synthesized for 8 h with $[OH^-]$ = 1.0 mol/L under different reaction temperature. When reaction temperature is 180 ^oC, the particles is a mixture of $K_4Na_4Nb_6O_{19}\cdot9H_2O$ [4] (JCPDS Card No. 14-0360) and some unknown impurity. When reaction temperature is 200 ^oC, all the diffraction peaks of the as-prepared powders are consistent with the standard diffraction date of hexagonal $NaNbO_3$ (JCPDS Card No. 37-1076). According to solution chemistry of niobium, different types of niobium oxide species such as $NbO_2(OH)_4^{3-}$, $Nb_6O_{19}^{8-}$, or $Nb_{12}O_{36}^{12-}$ exist in aqueous solutions depending on the solution pH as well as the ratio of niobium oxide [7]. In the $Nb_6O_{19}^{8-}$ hexaniobate, which is formed in low temperature, NbO_6 octahedrons share the edges as shown in Fig. 5-5 [8]. However, this structure is not stable due to the NbO_6 octahedrons is greatly distorted and the centre of negative charge in

the crystal structure might be deviated from that of positive charge. More stable structure can be formed under higher temperature conditions. The exchange of cations under high temperature could be contributed to the different ionic radius of Na^+ and K^+, which are 102 and 138 pm respectively; the smaller ionic radius of Na^+ probably provided its higher reaction activity, thus formed more stable structure. Therefore, when the reaction temperature is high enough, K^+ ions will be released, followed by the Na^+ ions occupying their side and resulted in a stable structure.
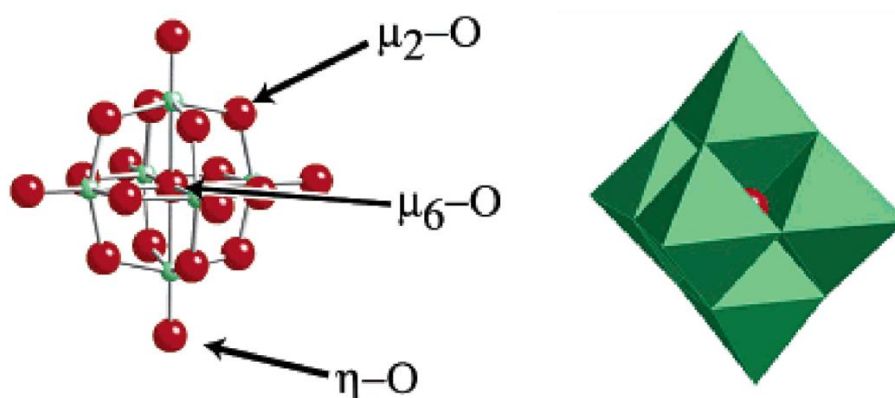
Fig. 5-5 $[Nb_6O_{19}]^{8-}$ ion shown in ball-and-stick (left) and polyhedral (right) representation. The structure has a central μ_6-O sites that is inert to exchange, 12 μ_2-O bridges, and 6 terminal η-O sites. The central μ_6-O site is shown as a red sphere in the polyhedral representation (right). In the ball-and-stick representation, the oxygens are red and the Nb(V) metals are green [8].

5.3.3 Effect of reaction time
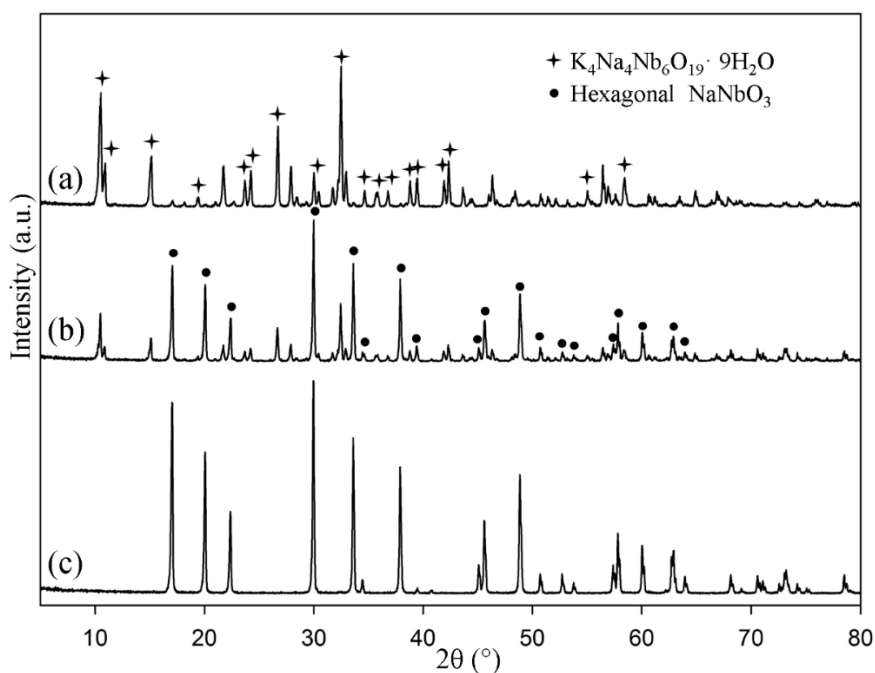
Fig. 5-6 XRD patterns of reaction under conditions of 200 °C , [OH⁻] = 1.0 mol/L
and K⁺ : Na⁺ ratio of 2 : 1 at different times: (a) 2 h; (b) 4 h; (c) 8 h.

The XRD patterns shown in Fig. 5-6 provide the evolution of product with the time extend under the conditions of 200 °C, $[OH^-]$ = 1 mol/L, and K^+ : Na^+ ratio of 2 : 1. As shown in Fig. 5-6a, the main product is $K_4Na_4Nb_6O_{19} \cdot 9H_2O$ (JCPDS Card NO. 14-0360). As the reaction time extended, the diffraction peaks of $K_4Na_4Nb_6O_{19} \cdot 9H_2O$ were decreased while hexagonal $NaNbO_3$ (JCPDS Card NO. 37-1076) was enhanced (Fig. 5-6b). The diffraction peaks of $K_4Na_4Nb_6O_{19} \cdot 9H_2O$ disappear as the reaction time over exceeds 8 h, and the hexagonal $NaNbO_3$ is obtained as the end product (Fig. 5-6c).

SEM images in Fig. 5-7 illustrate the morphological evolution of the powders obtained at different times. At the starting stage, the precipitations show irregular morphology (Fig. 5-7a). As the reaction time extended, small particles gradually disappeared and formed plate-like morphology (Fig. 5-7b). After 8 h, the small particles completely transformed to hexagonal plate-like morphology with of about 20 μm in diameter and 2 μm in thickness (Fig. 5-7c).
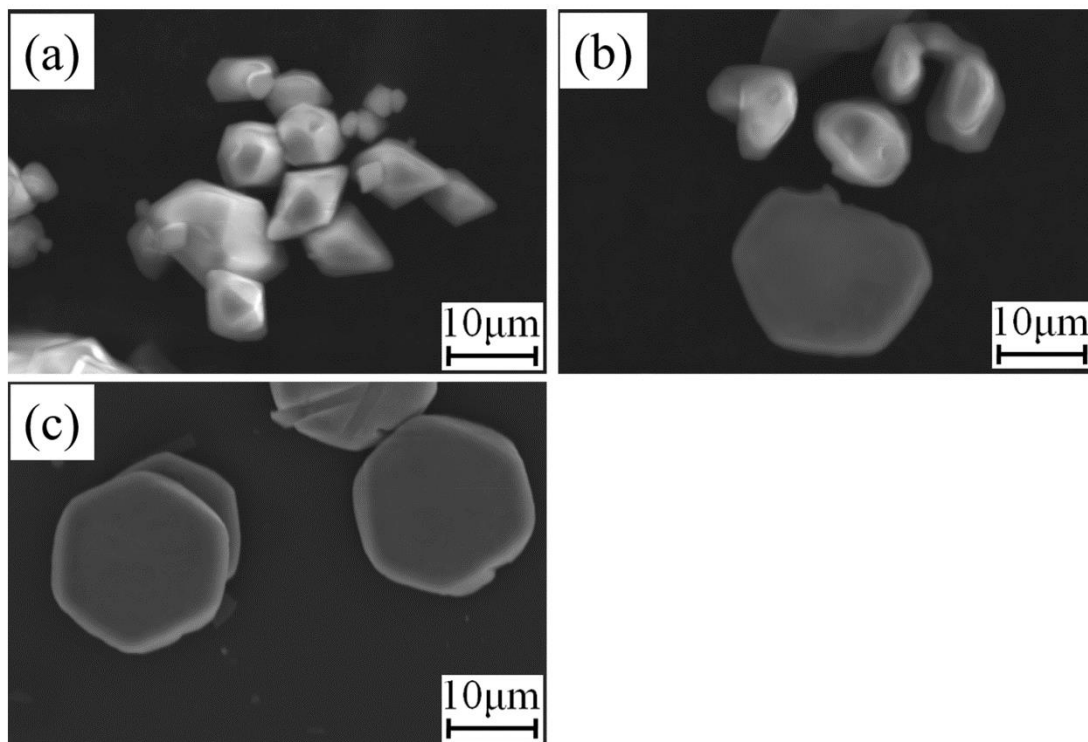
Fig. 5-7 SEM images of reaction under conditions of 200 °C, [OH⁻] = 1 mol/L and K⁺:Na⁺ ratio of 2 : 1 at different times: (a) 2 h; (b) 4 h; (c) 8 h.

5.3.4 Effect of K^+ : Na^+ ratio

Fig. 5-8 XRD patterns of particles obtained at $[OH^-] = 1$ mol/L for 8 h with different K^+ : Na^+ ratios: (a) 1 : 3 and 1 : 2; (b) 1 : 1, 2 : 1, 3 : 1 and 4 : 1; and inset (c) EDX analysis result.
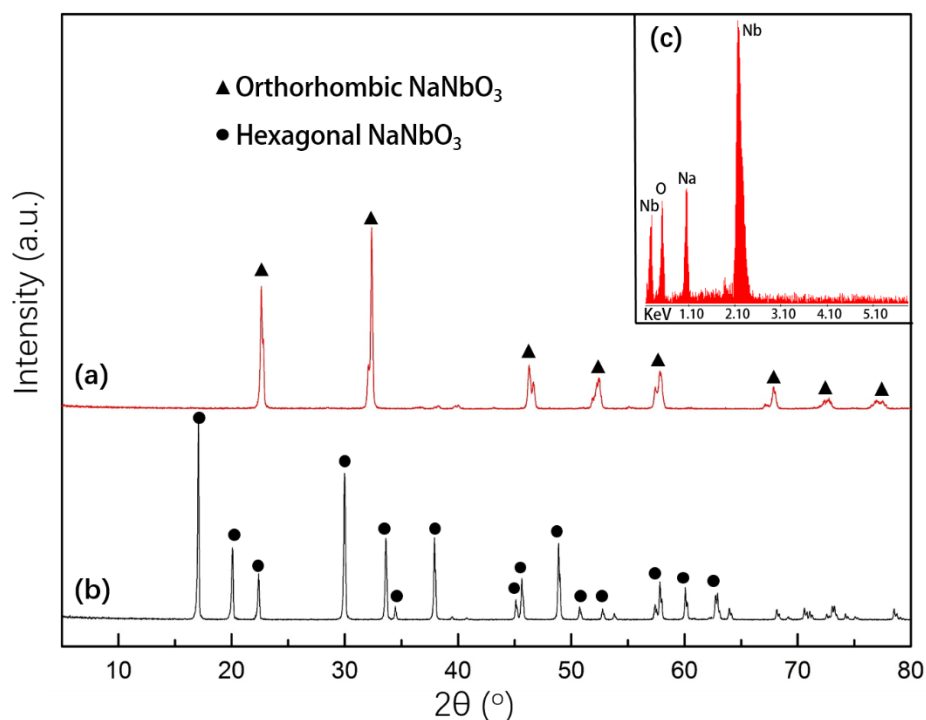
Fig.5-8 shows the XRD patterns of the powders obtained with different ratios of K^+ : Na^+ at 200 $^{\circ}$C for 8 h. When the ratio ranged from 1 : 3 to 1 : 1, the XRD patterns of the particles fit for those of orthorhombic $NaNbO_3$. When the ratio is equal to or greater than 1 : 1, hexagonal $NaNbO_3$ could be obtained. However, when the ratio was changed to 1 : 0, no precipitation was obtained. It could be deduced that when reacted long enough at low concentration of OH^-, K^+ could be totally replaced by Na^+ and product was only $NaNbO_3$. EDX analysis was used to prove the inference. Before the test, the sample was milled into smaller particles with diameter of about 1 μm by planetary ball mill. Then, EDX analysis was performed on positions including the face and section. All the results were the same and it are shown in Fig. 5-8c. The peaks are observed clearly for Na, Nb, and O elements, and no impurity is detected. When sufficient Na^+ exists in solution, a large number of the resultant Nb–O species in the alkaline solution system and their chemical interactions with plenty of Na^+ ions induce the subsequent phase transformation process, which dominates the crystallization of the

orthorhombic phase $NaNbO_3$. The Na^+ ions easily occupy the cavities of the corner-sharing NbO_6 octahedra, which form a three-dimensional framework to constitute perovskite $NaNbO_3$. While the amount of K^+ was greater than Na^+, $K_4Na_4Nb_6O_{19} \cdot 9H_2O$ was first synthesized, and was later transformed into hexagonal $NaNbO_3$ through ion exchange.
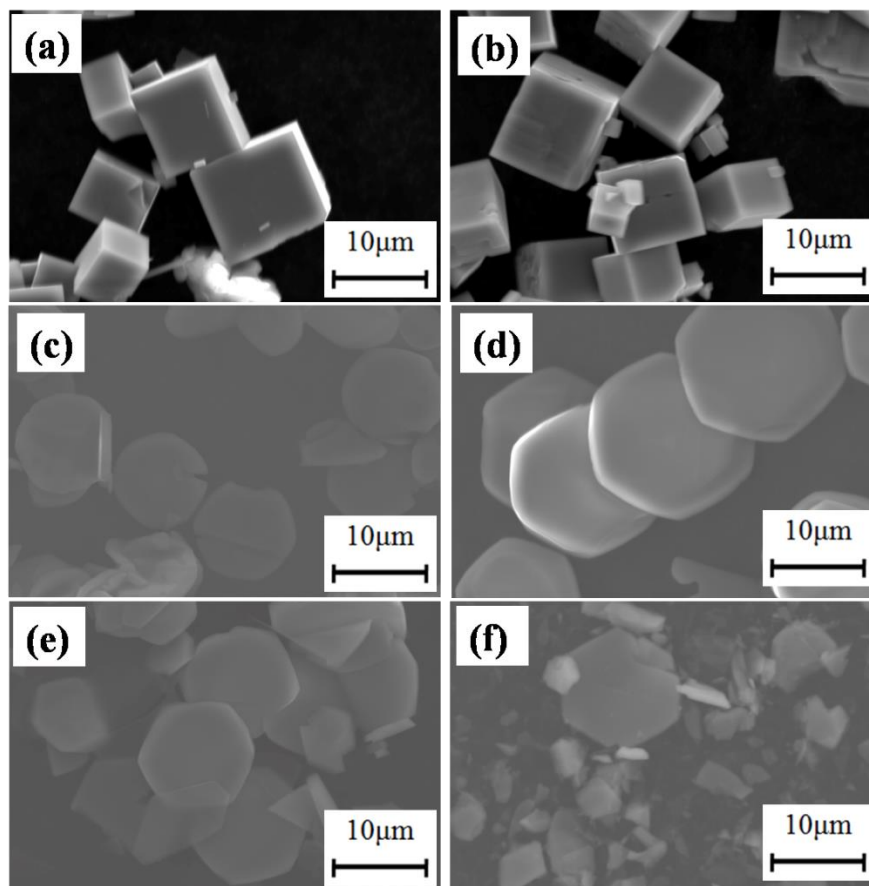
Fig. 5-9 SEM images of particles obtained at $[OH^-]$ = 1.0 mol/L for 8 h with different K^+: Na^+ ratios: (a) 1 : 3; (b) 1 : 2; (c) 1 : 1; (d) 2 : 1; (e) 3 : 1; (f) 4 : 1.

The SEMs of particles from different K^+ : Na^+ ratios are shown in Fig. 5-9. While the K^+ : Na^+ ratio was below 1 : 1, the orthorhombic $NaNbO_3$ displayed cubic morphology. As the ratio increased to 1 : 1, $NaNbO_3$ formed a hexagonal structure and displayed plate-like morphology. It is noteworthy that under high K^+ : Na^+ ratio (Fig. 5.9f), although the product remained in a hexagonal crystal structure, the particles could not remain intact and disintegrated into small pieces. Therefore, there should be a proper K^+ : Na^+ ratio for the preparation of plate-like morphology.

5.3.5 Effect of OH⁻ concentration
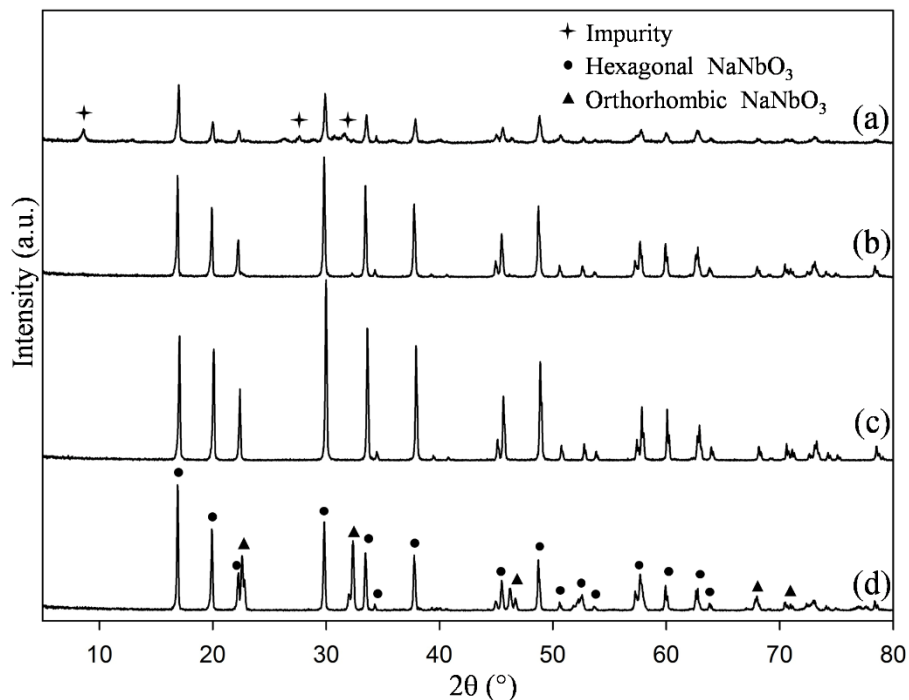
Fig. 5-10 XRD patterns of particles obtained at 200 °C for 8 h with K^+:Na^+ ratio of 2 : 1 in different [OH⁻]: (a) 0.5 mol/L; (b) 0.8 mol/L; (c) 1.0 mol/L; (d) 1.5 mol/L.

Figure 5-10 shows the XRD patterns of particles obtained at different concentrations of 0.5–1.5 mol/L. As shown in Fig. 5-10a, the diffraction peaks of hexagonal $NaNbO_3$ and a small amount of impurity are observed at the concentration of 0.5 mol/L. The impurity disappears as the concentration increases to 0.8 mol/L, as shown in Fig. 5-10. When the concentration increases to 1 mol/L, the increase of relative intensity indicates that the crystallinity of the particles is enhanced (Fig. 5-10c). By further increasing the concentration to 1.5 mol/L, a mixture of hexagonal and orthorhombic $NaNbO_3$ (JCPDS card No. 33-1270) is obtained (Fig. 5-10d).
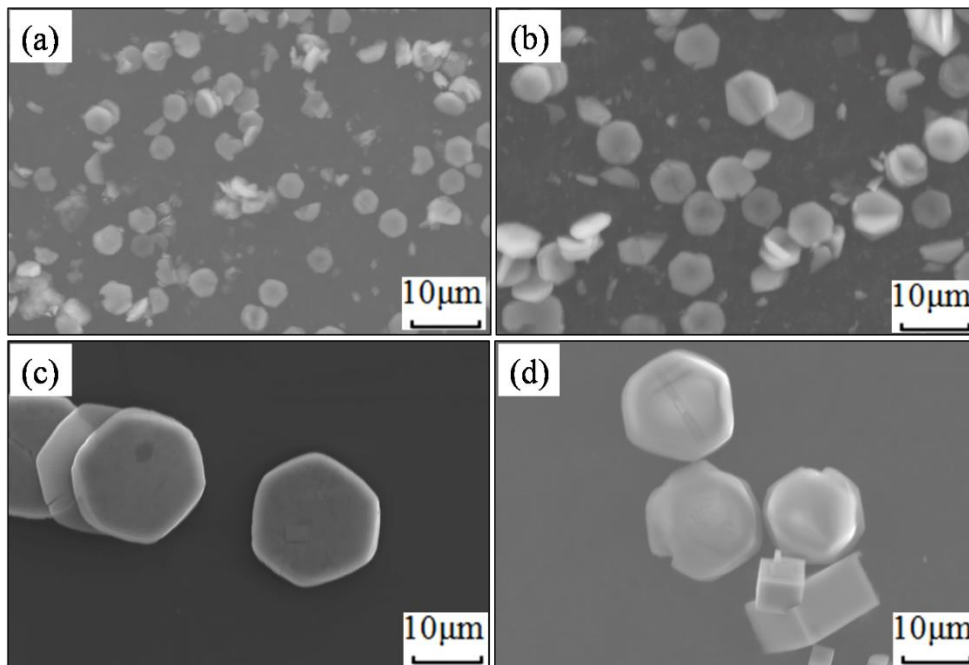
Fig. 5-11 SEM images of particles obtained at 200 °C for 8 h with K$^+$: Na$^+$ ratio of 2 : 1 in different [OH$^-$]: (a) 0.5 mol/L; (b) 0.8 mol/L; (c) 1.0 mol/L; (d) 1.5 mol/L.

SEM images of particles synthesized at different [OH$^-$] concentrations are shown in Fig. 5-11. In a low [OH$^-$] condition, the particles showed plate-like but not regular morphology with a diameter of about 3 μm (Fig. 5-10a). As [OH$^-$] increased to 0.8 mol/L, the size of the plate-like particles increased to about 8 μm (Fig. 5-11b). Particles of uniform size and plate-like morphology with a diameter of about 15 μm and thickness of about 2 μm were obtained at higher [OH$^-$] of 1 mol/L (Fig. 5-11c). When the [OH$^-$] reached 1.5 mol/L, the product was a mixture of plate-like hexagonal NaNbO$_3$ and cube-shaped orthorhombic NaNbO$_3$ (Fig. 5-11d). The formation of the hexagonal phase is sensitive to [OH$^-$]. Adjusting the concentrations of OH$^-$ is an effective approach to controlling the shape and size of particles.
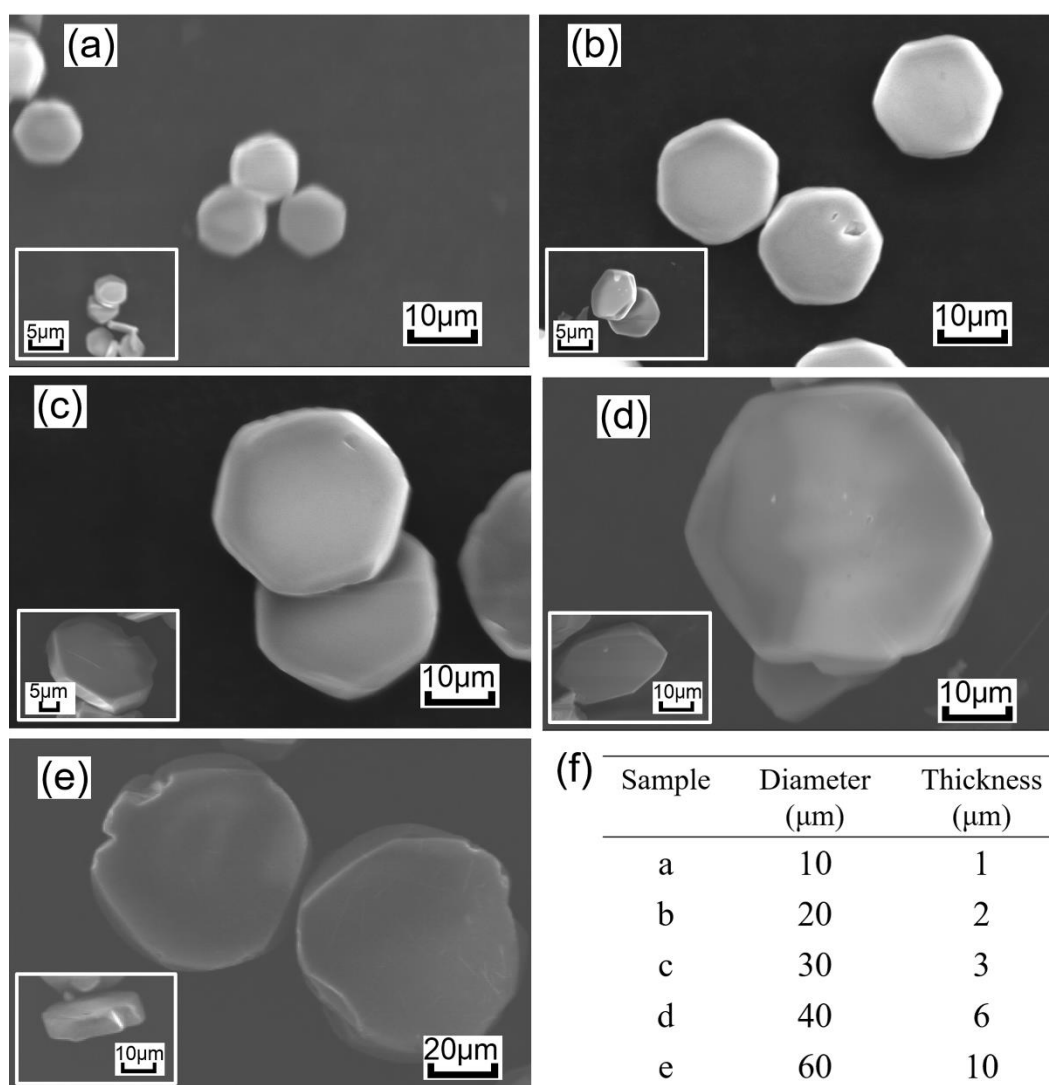
Fig. 5-12 SEM images of particles obtained at 200 °C for 8 h with K^+ : Na^+ ratio of 2 : 1 in different [OH^-]: (a) 0.7 mol/L; (b) 0.9 mol/L; (c) 1.0 mol/L; (d) 1.2 mol/L; (e) 1.4 mol/L and (f) the diameter & thickness of samples a-e.

Mineralizer concentration too low or too high were not favorable for preparing the plate-like $NaNbO_3$ particles, and the optimum concentration range was confirmed to be 0.4–1.4 mol/L. Through carefully controlling the [OH^-], particles with a diameter of 10–60 μm and a thickness of 1–10 μm were obtained. The mineralizer concentration used in the synthesis of samples a-e shown in Fig. 5-11 was 0.7 mol/L, 0.9 mol/L, 1.0 mol/L, 1.2 mol/L and 1.4 mol/L, respectively. The diameter and thickness of samples were shown in Fig 5-12f.

The particles size is particularly sensitive to the mineralizer concentration, perhaps because the solution supersaturation (σ) increased with the increase of mineralizer

concentration in this reaction. For two-dimensional nucleation growth, normal growth rate (Rn) of particles is directly proportional to solution supersaturation [9,10]. Therefore, the particle size, especially along (0001) plane, increased rapidly. However, excessive mineralizer concentration result in excessive supersaturation, 2-dimensional nucleation is replaced by 3-dimensional nucleation resulting cubic morphology.

Fig. 5-13 shows the particles obtained under different [OH$^-$] and K$^+$:Na$^+$ hydrothermal conditions. Only within the appropriate ranges, ilmenite type NaNbO$_3$ with plate-like morphology could be obtained.
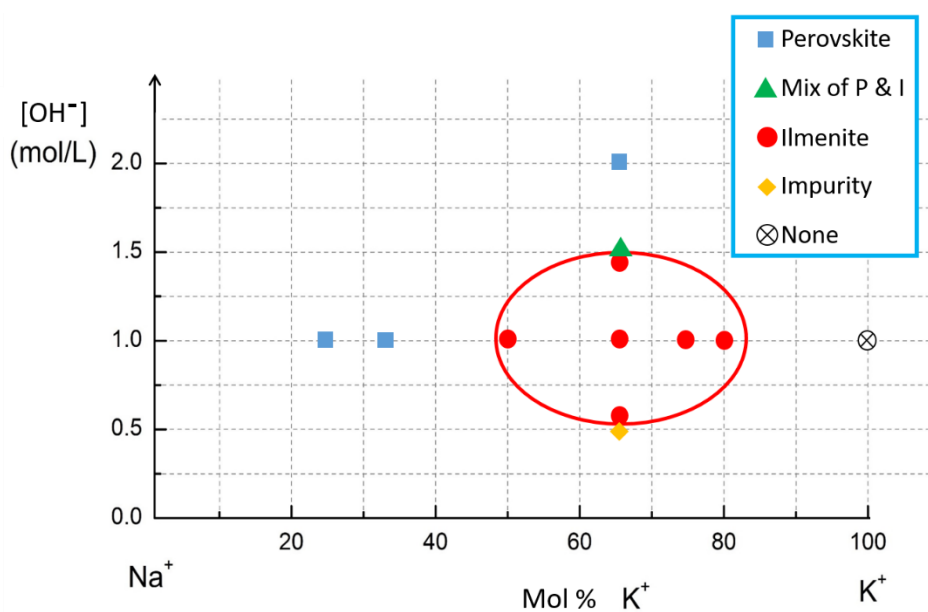
Fig. 5-13 Particles obtained under different [OH$^-$] and K$^+$:Na$^+$ hydrothermal conditions.

Formation Mechanism

From the crystal structure, hexagonal $NaNbO_3$ have anisotropic unit cell structures, which can induce anisotropic growth along crystallographically reactive directions, resulting in the formation of hexagonal structures. In addition, the reaction follows the 2-dimensional nucleation growth mechanism. The lowest surface energy of (0001) in hexagonal system leads facets tend to growth along (0001) surface resulting plate-like morphology.

From all of the above results, a plausible formation mechanism of this system is shown as follows:

$$3Nb_2O_5 + 8OH^- \rightarrow Nb_6O_{19}^{8-} + 4H_2O, \tag{1}$$

$$Nb_6O_{19}^{8-} + 4Na^+ + 4K^+ + 9H_2O \rightarrow K_4Na_4Nb_6O_{19} \cdot 9H_2O, \tag{2}$$

$$K_4Na_4Nb_6O_{19} \cdot 9H_2O + 2Na^+ \rightarrow 6NaNbO_3 + 4K^+ + 2OH^- + 8H_2O. \tag{3}$$
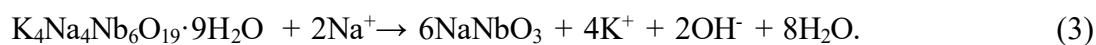
As temperature is raised, the thermal active energy promotes the acceleration of the reaction and the transformation from the intermediates to the final products. The reaction initially ruptures the corner-sharing of the niobium-oxygen polyhedra in Nb_2O_5, yielding intermediates with edge-sharing octahedra. Therefore, the first reaction step is the rupture of the corner-sharing between the NbO_6 octahedra (formula 1). Then, the $Nb_6O_{19}^{8-}$ reacted with metal cation and yielded $K_4Na_4Nb_6O_{19} \cdot 9H_2O$ (formula 2). As the temperature reached 200 °C, ion exchange was accessible. The phase transformation and morphology change occurred with the rearrangement of the cations in the network of these NbO_6 octahedra. Finally, the K^+ was replaced by Na^+, and the product was transformed to a single phase of $NaNbO_3$ (formula 3).

5.4 Phase transition and characterization of ilmenite NaNbO$_3$

5.4.1 Thermal analysis
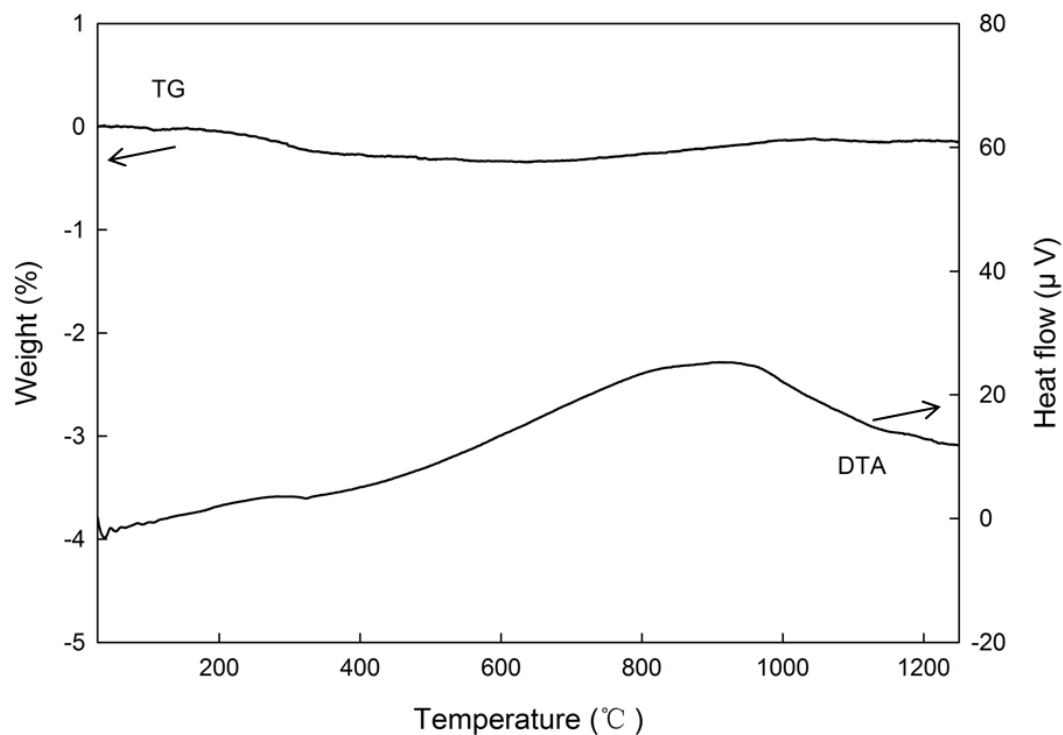
Fig. 5-14 TG–DTA plot of template particles after calcination treatment.

The sample was tested by TG–DTA analysis as shown in Fig. 5-14. The upper curve of TG is basically a straight line during the sample heated from room temperature to 1250 °C, indicating that the sample had good thermal stability. In the DTA plot, on the other hand, no decalescence peak was observed in the temperature range tested, indicating that the sample did not melt under 1250 °C.

5.4.2 Phase and morphology of particles after annealing treatment.
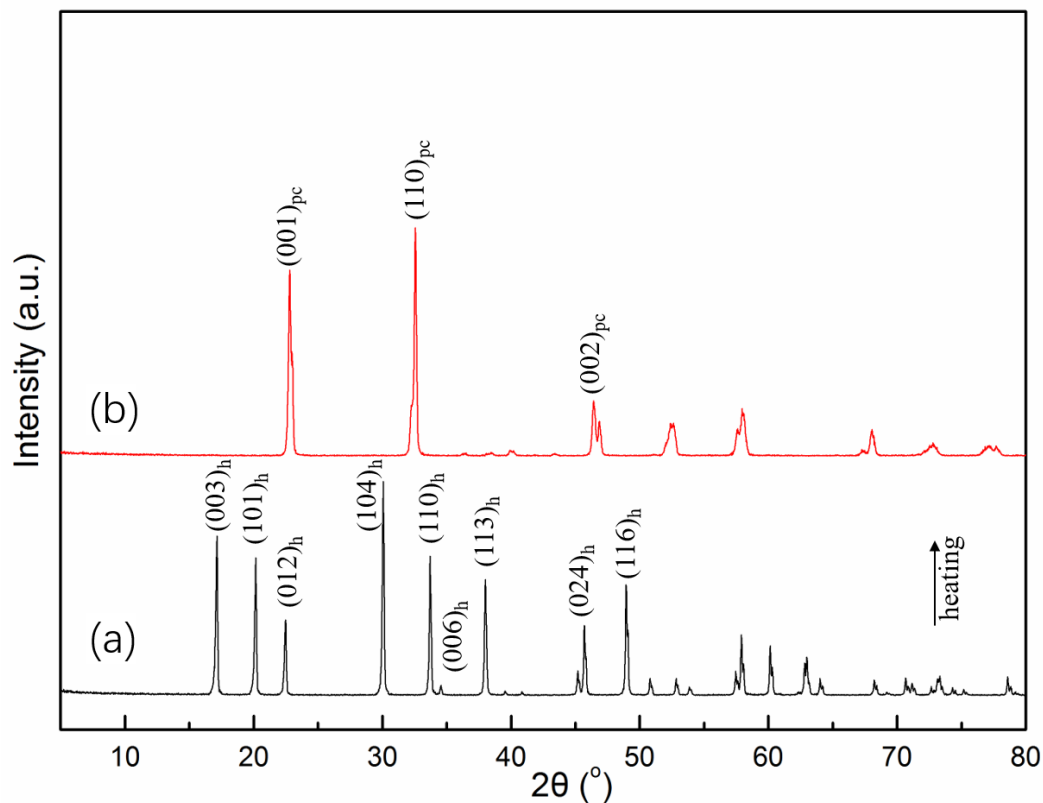
Fig.5-15 XRD patterns of (a) particles obtained at 200°C, [OH] = 1M and K$^+$:Na$^+$ ratio of 2:1 for 8 h and (b) the above particles after calcination treatment at 600°C.

Through annealing treatment at 600 °C lasting for 2 h, the product was totally transformed into perovskite structure according to the XRD results Fig. 5-15.
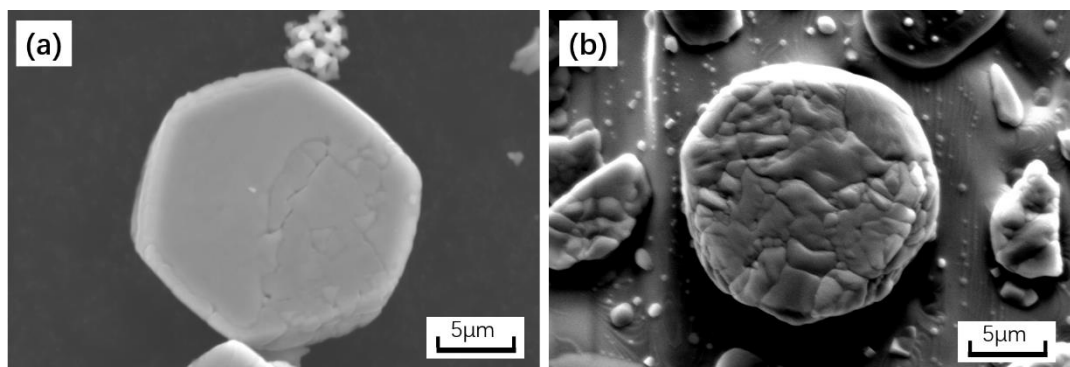
Fig. 5-16 SEM images of particles annealed at different temperature (a) 600 °C and (b) 1200 °C.

Although the morphology of the particles remains intact even after annealing at 1200 °C, some cracks appear on the surface as shown in Fig. 5-16. During the thermal

process, particles transformed from the hexagonal phase (H) at room temperature to the cubic phase (C) at high temperature and finally transformed into orthorhombic phase (O) after cooling down to room temperature. Thus, the crystal structure transformed from ilmenite into perovskite, which was stabilized by its denser molar volume and higher entropy [11]. The change in the crystal structure during the thermal treatment is shown in Fig. 5-17. The H to C transition is irreversible, while the C to O transition is reversible [12,13], indicating that Na^+ and Nb^+ are rearranged during the H to C transition. During the hexagonal-to-cubic phase transition, the theoretical density of the $NaNbO_3$ particles changed from 4.22 g/cm^3 to 4.44 g/cm^3, which can be attributed to the atomic arrangement becoming more compact. Therefore, the H to C phase transition is a process of contraction, and lattice vacancies generated during this process can explain the occurrence of these cracks.
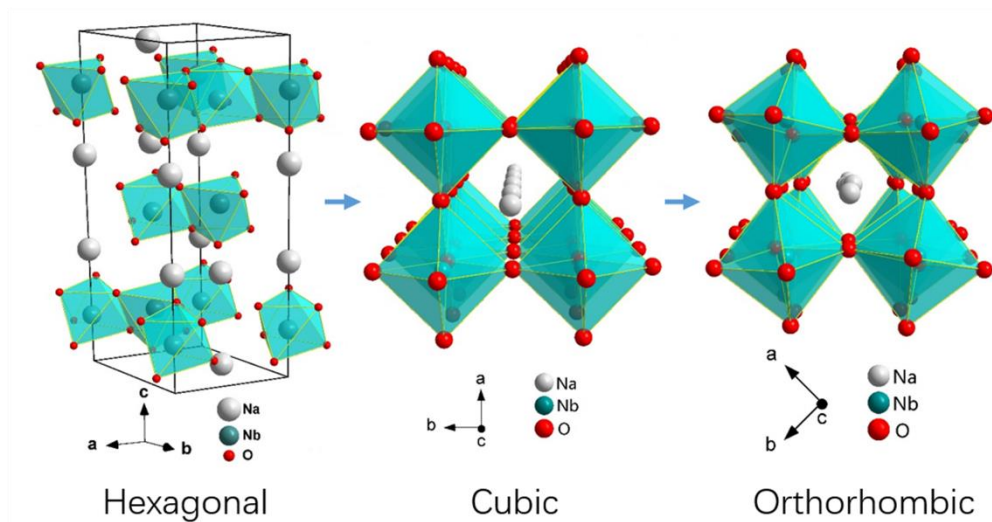
Fig. 5-17 Crystal structure transformation during the annealing treatment.

During the phase transformation, atomic rearrangement and volume shrinkage occurred asynchronously from the particle surface, which caused the formation of cracks on the particles. The top surface of the plate-like particles was closely related to our template purpose and almost the only part to observe. Therefore, we focused on factors that affect the morphology of top surface. Specifically, we hypothesized that the disorientation of the top surface mainly resulted from defects in the particles. The

accumulation of defects in the normal direction and the disorientation of the top surface should be positively correlated. Assuming that the defects in particles are evenly dispersed and the defect density is the same in all types of particles, a thicker particle should have a higher accumulation of defects in the normal direction and more disorientation on the top surface. Therefore, individually thermal treated (600 ^{o}C, 2 h) particles with different thickness were selected, and their surface orientation was characterized by EBSD analysis. As shown the inverse pole figure map in Fig. 5-18, the proportion of the $(001)_{pc}$ orientation decreased (represented in red) with the increasing thickness, thus indicating that the particle surface gradually changed from the $(001)_{pc}$ orientation to an irregular orientation.
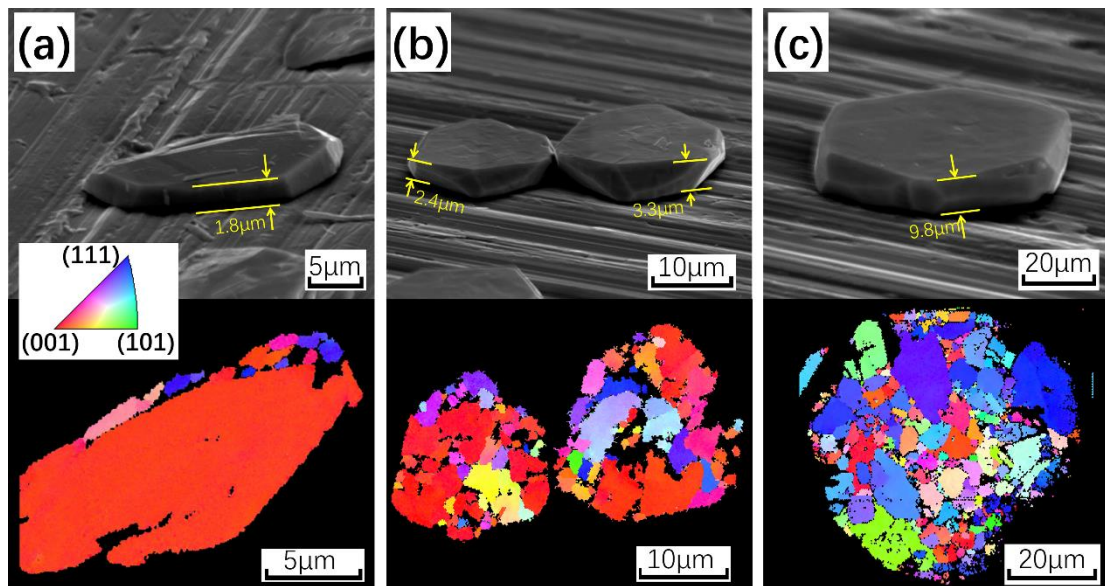
Fig. 5-18 SEM images and EBSD inverse pole figure map of particles with different thickness: (a) 1.8 μm; (b) 2.4 μm and 3.3 μm; (c) 9.8 μm.

However, the surface orientation of individual particles is not enough to represent the whole group. Therefore, Lotgering factors, *F*, calculated from XRD data were adopted to macroscopically characterize the overall sample quality. Characterization on the macro, the *F* proved to be of good use as a result of its easy calculation and the simplicity of the representation for the orientation degree. The *F* is calculated from the intensities of XRD peaks with the conventional 2θ/θ scan mode, and is defined as the following equation [14],

$$F = \frac{P - P_0}{1 - F_0} \ ,$$

where P denotes the fraction of the summation of the peak intensities corresponding to the preferred orientation axis to that of the summation of all diffraction peaks in particle-oriented materials. P_0 is P of a material with a random particle distribution. The F varies between zero to unity; $F = 0$ corresponds to random orientation, and $F = 1$ to perfect orientation [15].

Before testing, samples of particles with different thickness were prepared using a simple orientation treatment wherein the particles were first separated in alcohol by ultrasonic dispersion. When this dispersion was dropped onto a glass slide, the plate-like particles tended to lie flat on the glass surface. Thus, the particles were easily oriented by this treatment.
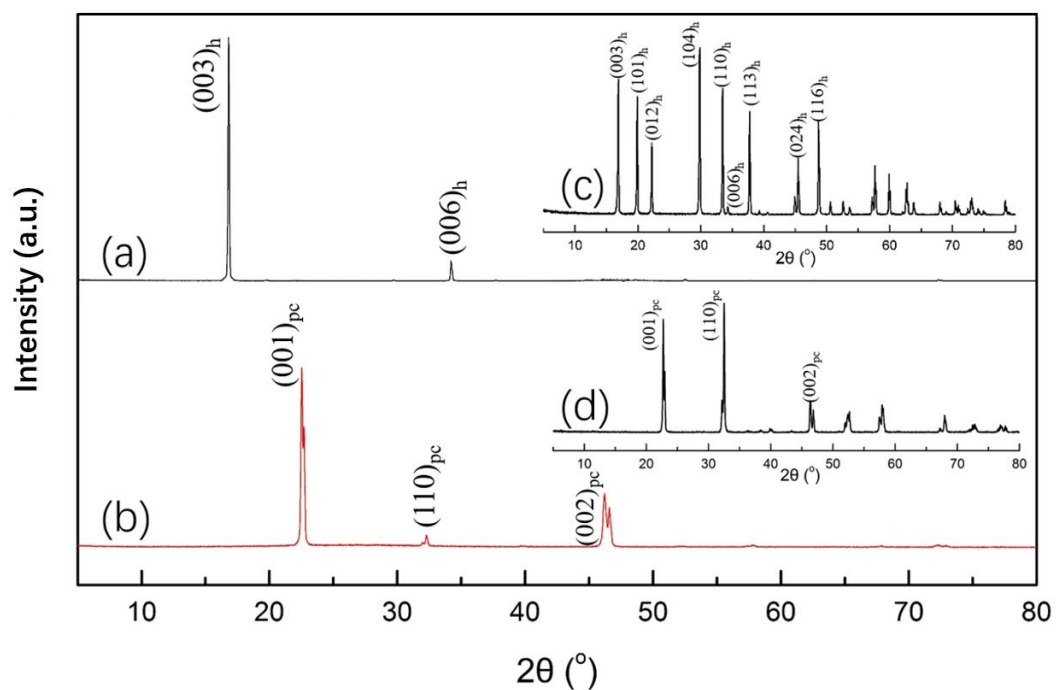
Fig. 5-19 XRD patterns of oriented sample of particles (a) before and (b) after thermal treatment at 600 °C and inset (c), (d) XRD patterns of non-oriented sample of particles.

The XRD patterns of the oriented samples with the a particle thickness of 1 μm are shown in Fig. 5-19a. In contrast with the unoriented sample (Fig. 5-19c), the diffraction peaks disappeared except those indicating the (003) and (006) faces, thus

indicating that the major face of the particles is parallel to the crystallographic (00l) plane. The thermal treatment transformed the hexagonal $NaNbO_3$ with an ilmenite structure into the more stable perovskite structure Fig. 5-19b. The Lotgering factors (F) of the (00l) crystal planes of the samples before and after thermal treatment and its variation ratio R could be calculated using the XRD relative peak intensities. R is defined by

$$R = \frac{F_i - F_p}{F_i} \, ,$$

where F_i and F_p are calculated before and after the thermal treatment, respectively. The calculated results for particles with a thickness of 1 μm were $F_i = 0.954$, $F_p = 0.91$ and $R = 4.61\%$. The same measurements were carried out for thicker particles, and the results are shown in Fig. 5-20.
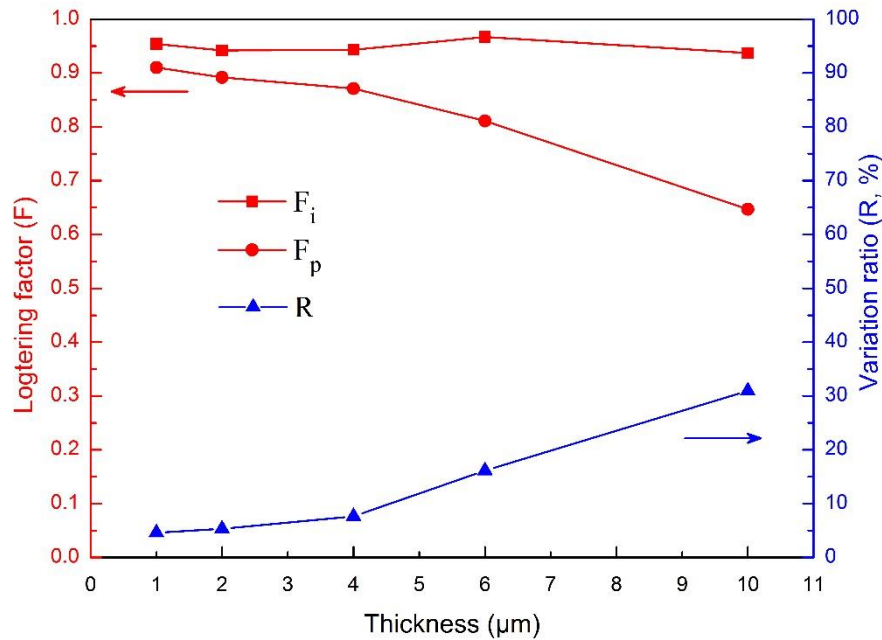
Fig. 5-20 The Lotgering factors of particles with different thickness
before and after annealing treatment and its variation ratio.

Due to the limitations of the simple orientation treatment, F_i could not be ideal (i.e., 1) and therefore, a value of about 0.95 is acceptable as a macroscopic threshold value to quantify ordering. After the thermal treatment, F_p decreased; however, the variation ratio tended to increase. This indicates that the thinner particles remained well

oriented. This result demonstrates that the synthesized particles could be a suitable template for fabricating potassium sodium niobate-based lead-free piezoelectric ceramics if the particles thickness is sufficiently thin.
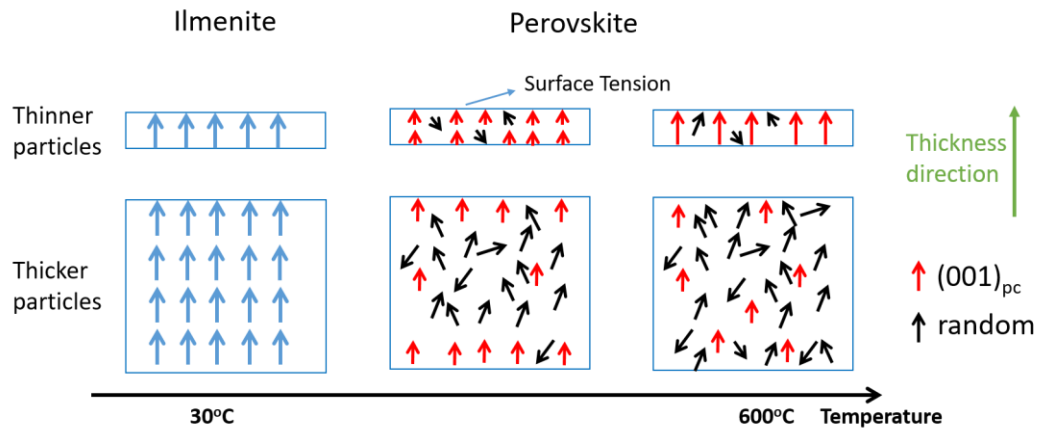
Fig. 5-21 Orientation change of particles with different thickness during thermal treatment.

Fig. 5-21 shows the orientation change of particles with different thickness during thermal treatment. As temperature increases, the phase change begins from the outside to inside. Due to the effect of surface tension, the movement of the cation on the surface of particles presents a regular state. In the case of a thin particle, the movement of the cations inside the particle is also affected by the surface tension and follows the change of surface cation, resulting in a well orientation on the surface. However, as the thickness of the particle increases, the influence of surface tension on the interior decreases, resulting in an irregular movement of the cation inside the particle. Due to the increase of accumulated defects, the surface orientation of a thicker particle becomes disordered.

5.5 Summary

In this chapter hexagonal $NaNbO_3$ particles with plate-like morphology were synthesized by hydrothermal method. Hydrothermal conditions, such as reaction time, temperature, mineralizer concentration, surfactant, and K^+ : Na^+ ratio, were discussed. Mineralizer concentration is the key factor for controlling the particle size. The mineralizer concentration in the hydrothermal reaction was able to control the particle morphology. Plate-like particles with a diameter of 10–60 μm and a thickness of 1–10 μm were obtained at mineralizer concentrations between 0.7–1.4 M. However, excessive mineralizer concentration resulted in excessive supersaturation, and two-dimensional nucleation was replaced by three-dimensional nucleation, resulting in cubic morphology. The phase transition of particles was also discussed. A thermal treatment at 600 °C irreversibly transformed the ilmenite structure into the perovskite structure. The contraction of the lattice during the phase transformation caused some lattice defects and further resulted in a change in the surface orientation. The thickness of the particles was positively correlated with the disorientation of the top surface. More defects accumulated in the thickness direction as the particles became thicker, and the surface orientation changed from ordered to completely disordered. These results indicate that thinner particles tend to have higher orientation in the (00l) crystal planes.

References

[1] Matsubara M, Yamaguchi Y, Sakamoto W, Kikuta K, Yogo T, Hirano S, Processing and piezoelectric properties of lead-free (K, Na)(Nb, Ta)O_3 ceramics. J. Am. Ceram Soc., 88, 1190-1196, 2005.

[2] Matsubara M, Kikuta K, Hirano S, Piezoelectric properties of $(K_{0.5}Na_{0.5})(Nb_{1-x}Ta_x)O_3$-$K_{5.4}CuTa_{10}O_{29}$ ceramics. J. Appl. Phys., 97, 114105-114111, 2005.

[3] Park SH, Ahn CW, Nahm S, Song JS, Microstructure and piezoelectric properties of ZnO-added $(Na_{0.5}K_{0.5})NbO_3$ ceramics. Jpn. J. Appl. Phys., 43, L1072-L1074, 2004.

[4] S. Bai, T. Karaki, Two-step synthesis of platelike potassium sodium niobate template particles by hydrothermal method, J. Am. Chem. Soc., 96, 2515-2518, 2013.

[5] A. V. Besserguenev, M. H. Dickman, M. T. Pope, Robust, alkali-stable, triscarbonyl metal Derivatives of hexametalate Anions, $[M_6O_{19}\{M'(CO)_3\}_n]^{(8-n)-}$(M=Nb, Ta; M'=Mn, Re; n=1, 2), Inorg. Chem., 40, 2585, 2001.

[6] Zhang, X. L., Qiao, R., Qiu, R., Kim, J. C., & Kang, Y. S. Fabrication of hierarchical ZnO nanostructures via a surfactant-directed process, Crystal Growth & Design, 9, 2906-2910, 2009.

[7] A. V. Besserguenev, M. H. Dickman, M. T. Pope, Robust, alkali-stable, triscarbonyl metal Derivatives of hexametalate Anions, $[M_6O_{19}\{M'(CO)_3\}_n]^{(8-n)-}$(M=Nb, Ta; M'=Mn, Re; n=1, 2), Inorg. Chem., 40, 2585, 2001.

[8] Black, J. R., Nyman, M., & Casey, W. H. Rates of Oxygen Exchange between the $[H_xNb_6O_{19}]_{8-x}$ (aq) Lindqvist Ion and Aqueous Solutions. Journal of the American Chemical Society, 128, 14712-14720, 2006.

[9] Burton W K, Cabrera N. Crystal growth and surface structure. Part I. Discussions of the Faraday Society, 5, 33-39, 1949.

[10] Malkin A I, Chernov A A, Alexeev I V. Growth of dipyramidal face of dislocation-free ADP crystals; free energy of steps. Journal of Crystal Growth, 97, 765-769, 1989.

[11] Mehta, A., Navrotsky, A., Kumada, N., and Kinomura, N. Journal of Solid State Chemistry, 102, 213, 1993.

[12] Glazer, A. M., and H. D. Megaw Acta Crystallographica Section A: Crystal Physics,

Diffraction, Theoretical and General Crystallography, 29, 489, 1973.

[13] X.B. Wang, Z. X. S., Z.P. Hu, L. Qin, S.H. Tang, M.H. Kuok Journal of Molecular Structure, 385, 1, 1996.

[14] F. K. Lotgering, Topotactical reactions with ferrimagnetic oxides having hexagonal crystal structures-I, J. Inorg. Nucl. Chem., 9, 113-123, 1959.

[15] Furushima, R., Tanaka, S., Zenji, K. A. T. O., & Uematsu, K. Orientation distribution-Lotgering factor relationship in a polycrystalline material-as an example of bismuth titanate prepared by a magnetic field. Journal of the Ceramic Society of Japan, 118, 921-926, 2010.

Chapter 6

Fabrication of Oriented KNLN – BZ – BNT Piezoceramics

6.1 Introduction

It is well known that the crystallization process is of technological importance in the manufacture of ceramics. The physico-chemical properties of the ceramics largely depend on the microstructure, phase and the morphology of the crystalline, *etc.* Controlled crystallization makes it possible to obtain ceramic materials with the desired properties [1-3]. The oriented ceramics exhibited improved and highly anisotropic properties when compared with randomly oriented ceramics. Reactive templated grain growth (RTGG) offers the possibility of fabricating grain-oriented polycrystalline ceramics. Crystallographic texturing of polycrystalline ferroelectric ceramics, such as $Pb(Mg_{1/3}Nb_{2/3})O_3$–$PbTiO_3$ [4] and $Pb(Mg_{1/3}Nb_{2/3})O_3$–$Pb(Zr,Ti)O_3$ [5], results in greatly enhanced piezoelectric properties that can reach$\geq$50% of single-crystal values [6]. For the lead-free piezoceramics, Tani [7] first prepared $Bi_{0.5}Na_{0.5}TiO_3$ lead-free ceramics by using $Bi_4Ti_3O_{12}$ as template. Sugawara *et al.* [8] prepared $BaTiO_3$ ceramics using $Ba_6Ti_{17}O_{40}$ template in 2001. Gao [9] prepared oriented $Bi_{0.5}(Na,K)_{0.5}TiO_3$ ceramics with d_{33} of 134 pC/N parallel to casting plane.

In chapter 3, BZ–KNLN–BNT tertiary system piezoceramic was developed for the performance with temperature-stability. In order to improve its electrical properties, texture technique can be an effective way.

In this chapter, BZ–KNLN–BNT was employed as matrix material; plate-like $NaNbO_3$ particles synthesized in chapter 5 was used as template. Using RTGG method, oriented BZ–KNLN–BNT piezoceramic was fabricated. Oriented process of ceramics was studied and template particles evolution during the RTGG process was also discussed.

6.2 Experimental section

Slurry for tape-casting was first prepared. It is uniformly mixed with solvent, binder, dispersant, plasticizer, matrix powders and template particles. Specific slurry component is listed in table 6-1. Raw materials are well mixed by a mild roller milling. Then the slurry was coated on the carrier foil using the tape-casting machine which was introduced in Fig. 2-3 (a). After drying, this film with carrier foil was cut into same size. The carrier foil was carefully stripped and films were laminated into a thin plate with a thickness of 1.2 mm. In order to ensure the density of the sample, the thin plate was compacted at 70 °C, 50 MPa by hot insostatic pressing (HIP). Then the plate was cut into small square with a length of 10 mm. After burning out the binder carefully, the samples were sintered between 1000 °C and 1200 °C for a period of time. The sintered samples were lapped to 1mm thickness and then coated with silver-electrode on both surfaces at 600 °C for 1 h, then poled in 130 °C of silicone oil for 15 min with 1kV/mm.

Table 6-1 Slurry component.

Function	Reagent	Abbreviation	Dosage (g)
Solvent	Ethanol	EtOH	20
	Ethyl acetate	EAC	20
Binder	Polyvinyl butyral	PVB	16
Dispersant	Glyceryl trioleate	GT	1.55
Plasticizer	Polyethylene glycol	PEG400	2.4
	Butylbenzyl phthalate	BBP	2.4
Matrix and template	-	-	100

The crystal structure and grain orientation were determined by the intensity of X-ray diffraction (XRD) (Model RINT 2200; Rigaku Corp., Tokyo, Japan) on the major surfaces of sintered ceramics, with 2θ in the range of 5–80° and with a step of 0.02°. The morphology and microstructure of the samples were characterized by scanning electron microscopy (SEM) (S-3000N, Hitachi Ltd., Tokyo, Japan). The T_c was determined at the peak value from the curve of the temperature dependence of the

dielectric constant at 1 kHz. The electromechanical coupling factor k_p was measured by the resonance-antiresonance method, and the piezoelectric constant d_{33} measured by a d_{33}-meter.
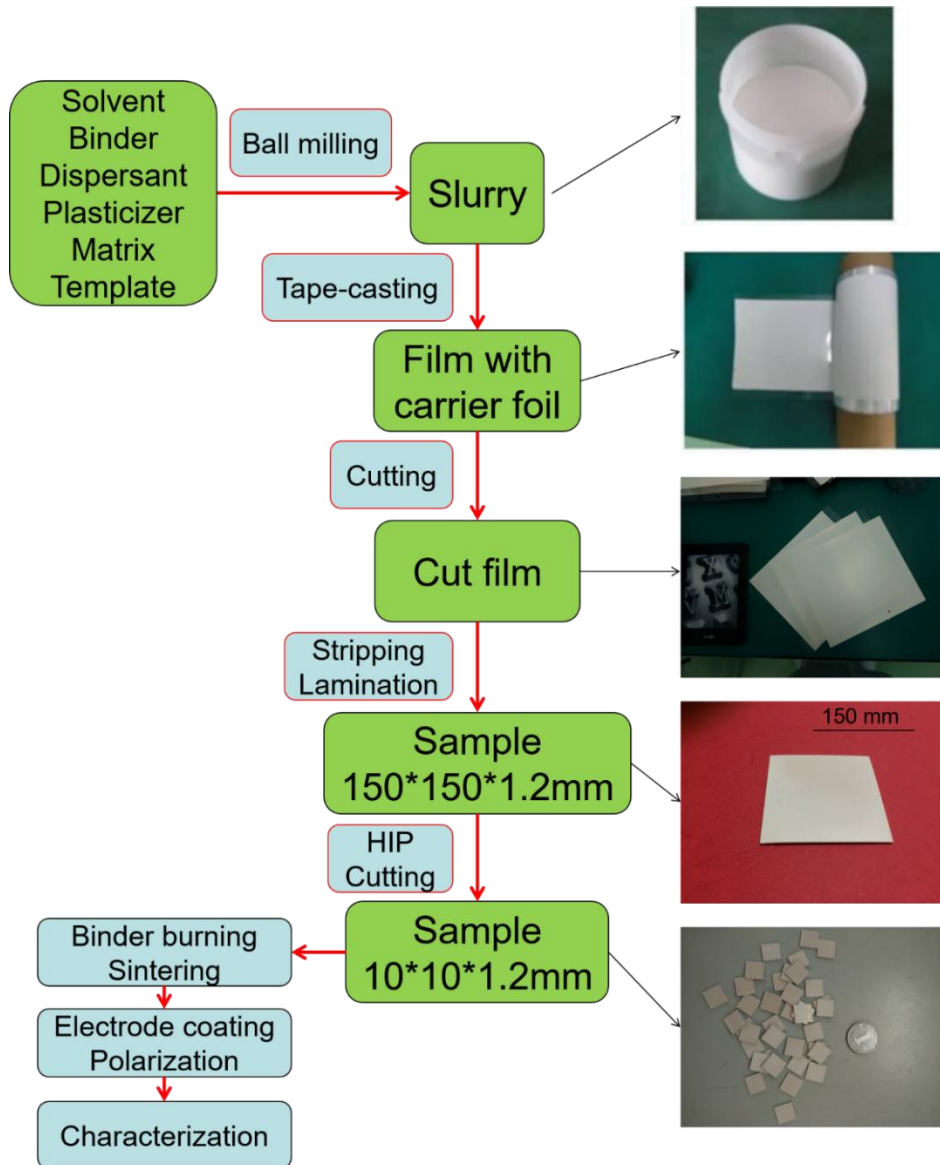
Fig. 6-1 Flow diagram and the corresponding physical photos.

6.3 Results and discussion

The difficulty of experimental operation rises with smaller diameter of template particles and thinner tape-casting film. In this experiment, template particles with 20 μm in diameter and 2 μm in thickness were selected in this work. The samples were stacked together and covered with a small crucible during sintering process to reduce the volatility of K^+ and Na^+. Two kinds of grain growth, matrix-matrix and matrix-template, existed during the sintering process. In order to reduce the matrix-matrix growth, a faster heating rate of 10 °C/min was used in the sintering process.

Physical photo of samples sintered under different temperature for 5 h was shown in Fig. 6-1. With the sintering temperature increase, shrinkage rate of samples was gradually increased. However, the sample after 1180 °C sintering could not be separated indicate that the sintering temperature could not be further increased.
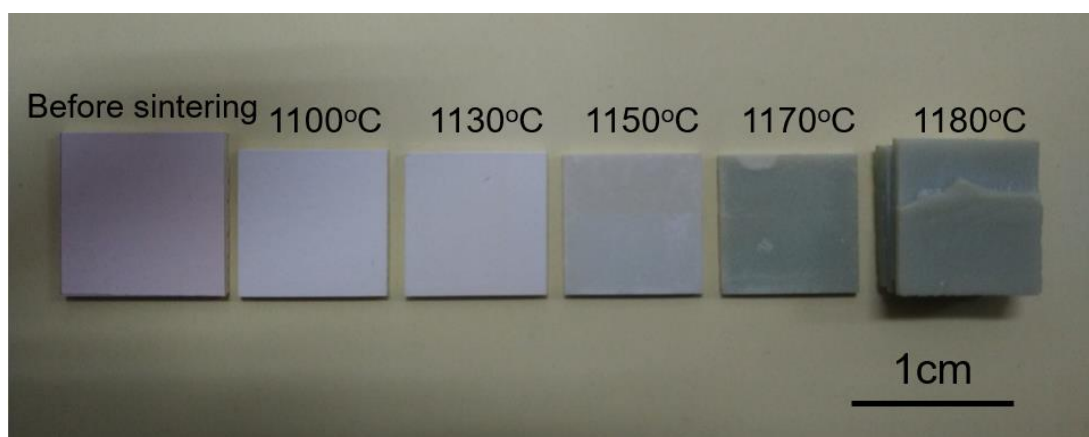
Fig. 6-2 Images of samples sintered under different temperature for 5h.
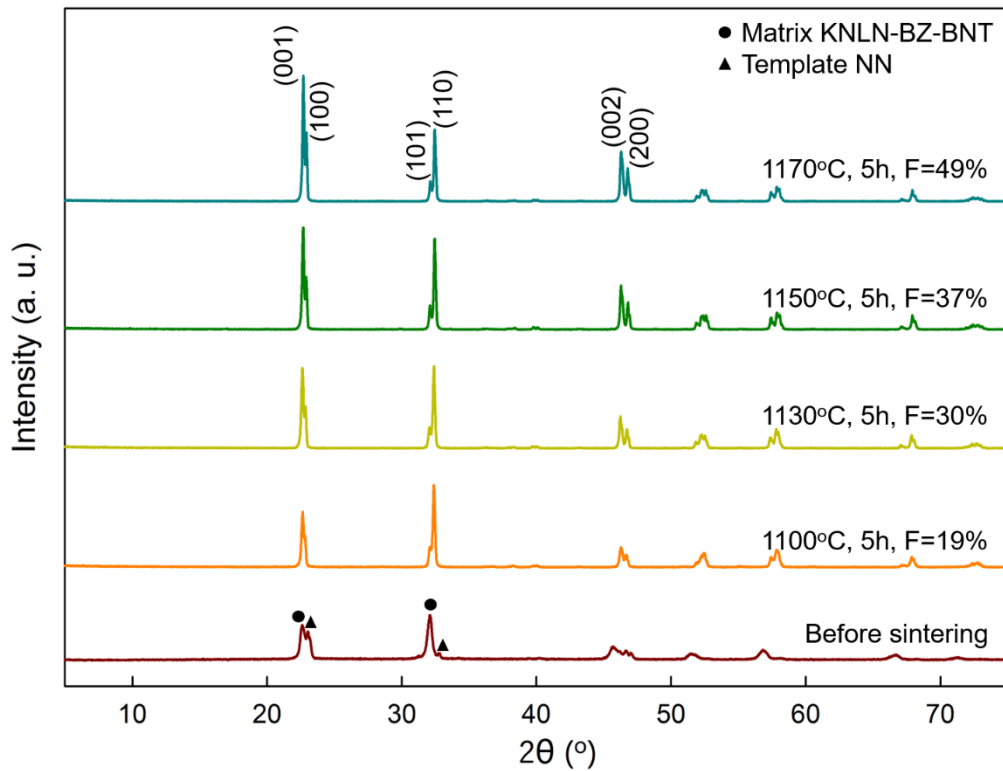
Fig. 6-3 XRD patterns of samples before sintering and sintered under different temperatures for 5h.

The XRD patterns shown in Fig. 6-3 provide the XRD patterns of samples before sintering and sintered under different temperatures for 5 h. Due to the little difference in the size of the lattice between matrix KNLN−BZ−BNT and template NN, their diffraction peaks were separated before sintering. After sintering, only a perovskite structure diffraction peak could be observed, indicating the reaction between the matrix and the template was completed. When the sintering temperature is at 1100 °C, 1130 °C, 1150 °C and 1170 °C, the Lotgering factor (F) of samples is 19%, 30%, 37% and 49%, respectively. The relative density of samples sintered under different temperature is shown in Fig. 6-4.

Burke [10] reported only when the relative density of the ceramics reached 90%, the grain could abnormally grow because of the pores pin grain boundaries. Hong *et al.* [11] reported that the abnormal grain growth of alumina occurred when the relative density of ceramics reached 97%. Since the grain growth during the texturing process is similar to the abnormal growth of grains, it can be inferred that there is a critical

relative density of KNLN−BZ−BNT ceramics when the grain began to orient grow. In this experiment, the critical relative density was about 90%.
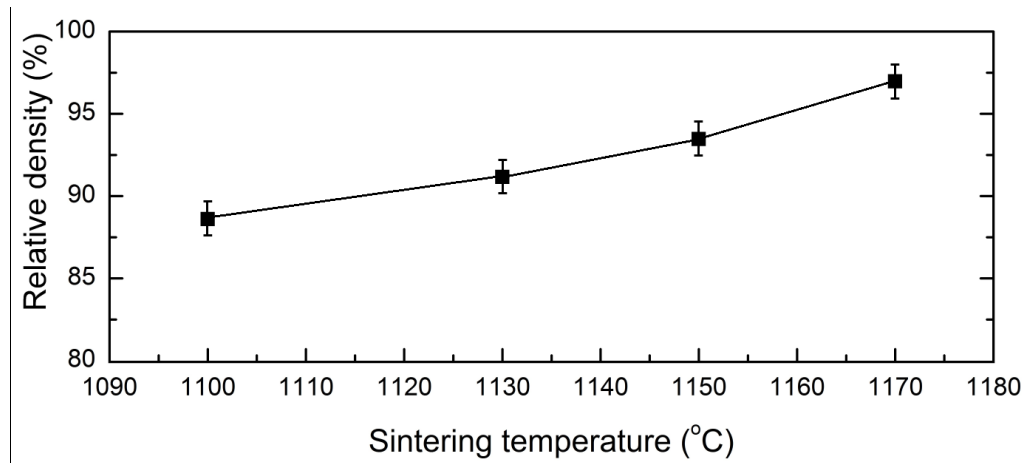
Fig. 6-4 The relative density of samples sintered under different temperature.
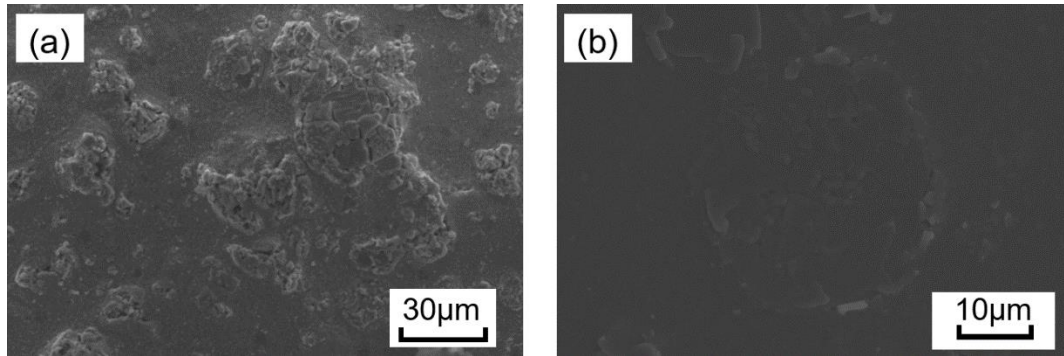
Fig. 6-5 SEM images of sample sintered at 1170 °C for 5h
(a) surface and (b) thermally etched surface.

SEM images of samples sintered at 1170 °C for 5h were shown in Fig. 6-5. From the higher magnification of the thermally etched surface image (Fig. 6-5b), the diameter of the oriented particles increased to 30 μm and matrix-matrix grain growth did not make the grain of ceramics become very large. In the sintering process, the thermodynamic driving force of oriented grain growth was the solubility difference between template particles and matrix particles. The solubility of substances in liquid phase (S) is defined by the relationship:

$S = S_0 \exp(2\sigma_m M / \rho r R T),$

where S_0 is equilibrium solubility, σ_m is average surface free energy, M is molecular

weight, ρ is density, r is the radius of the particles, and R is gas constant. According to this formula, the difference of solubility in the liquid phase is mainly caused by the difference of grain size. Due to the large size of template particles than matrix particles, the surface energy of the template particles is much smaller than the surface energy of the matrix particles. Therefore, the solubility of the template particles in the liquid phase (S_T) is smaller than that of the matrix particles (S_M). With the increase of the sintering time, the template particles gradually grew. Moreover, according to Gibbs-Wulff theorem: a droplet or crystal will arrange itself such that its surface Gibbs free energy is minimized by assuming a shape of low surface energy. Perovskite KNLN–BZ–BNT belongs to the cubic crystal system, with strong symmetry, and its most stable morphology was cubic. Therefore, in the early stage of grain growth, due to the length of the template particles is larger than the thickness, the growth rate of the template particles in the thickness direction was greater than in the length direction. After a period of growth, the difference between the thickness and the length decreased, and the growth rate in two directions also decrease, resulting in a limited growth of the oriented particles.

Above all, the orient development process in KNLN–BZ–BNT ceramics can be divided into 3 stages which was shown in Fig. 6-6: (1) ceramics densification followed with in situ reaction between template particles and matrix particles; (2) rapid growth of individual oriented grain; (3) slow growth of oriented grain. In the first stage, with the increasing of the sintering time, pores in the ceramics were gradually eliminated and the ceramics become denser. With increasing contact between the template particles and matrix particles, the reaction began as mutual diffusion of Na^+, K^+ and Li^+, then a layer of KNLN formed on the surface of $NaNbO_3$ template particles. As the reaction is only the mutual diffusion of ions, the morphology of the template grain unchanged, so this process is called in situ reaction [12,13]. The texturing then proceeded to the second stage. The matrix particles were rapidly epitaxial growth along the template particles formed oriented grain. After the grain growth to a certain extent, the growth rate began to slow down, the reaction has entered the final stage.

(a) First stage

Matrix particles   Template particle

(b) Second stage

S

S_M

ΔS

S_T

X

Liquid phase

Nucleation and growth

(c) Last stage

Oriented grain
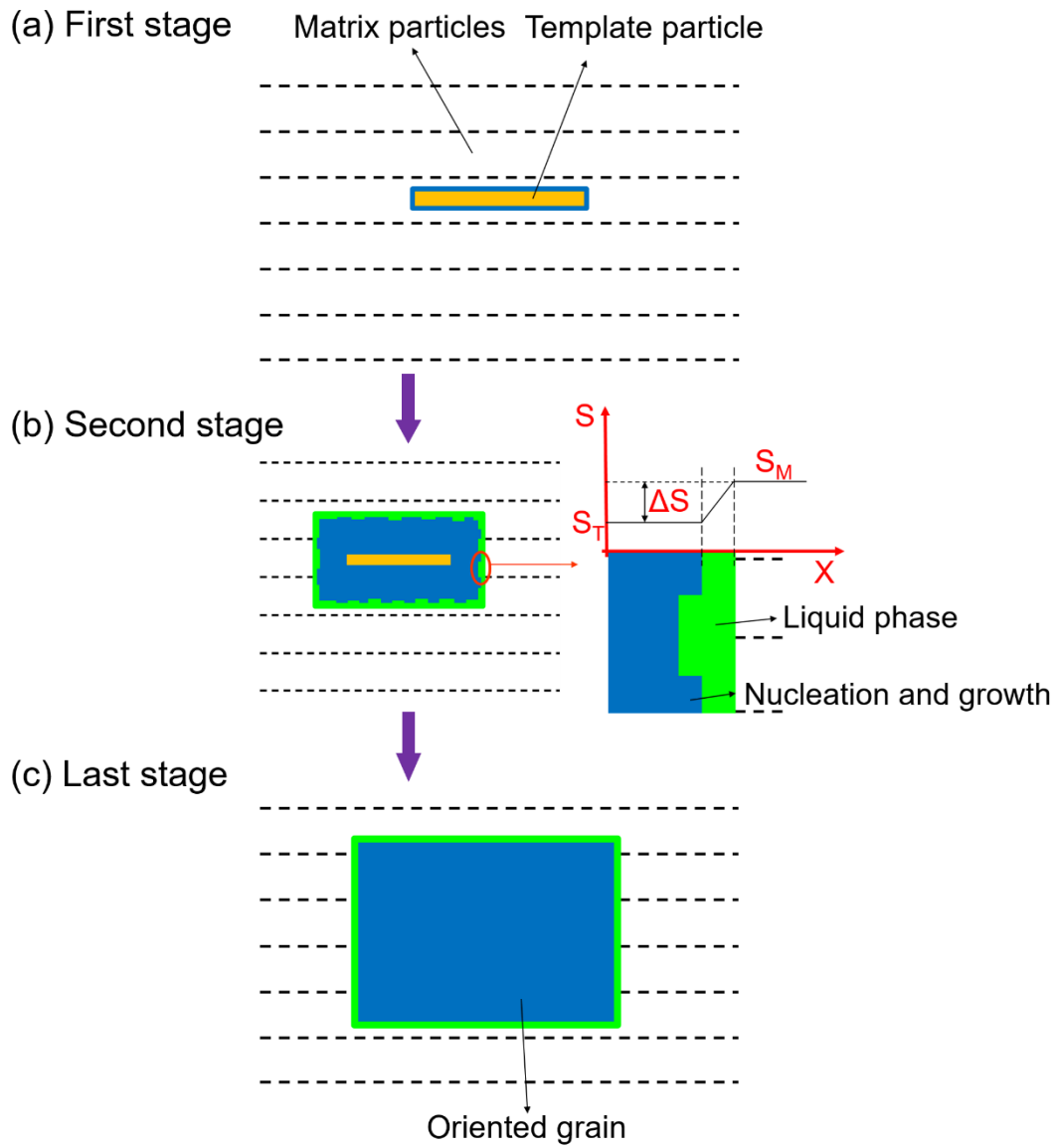
Fig. 6-6 Schematic diagram of the process of orient development of KNLN–BZ–BNT ceramics.
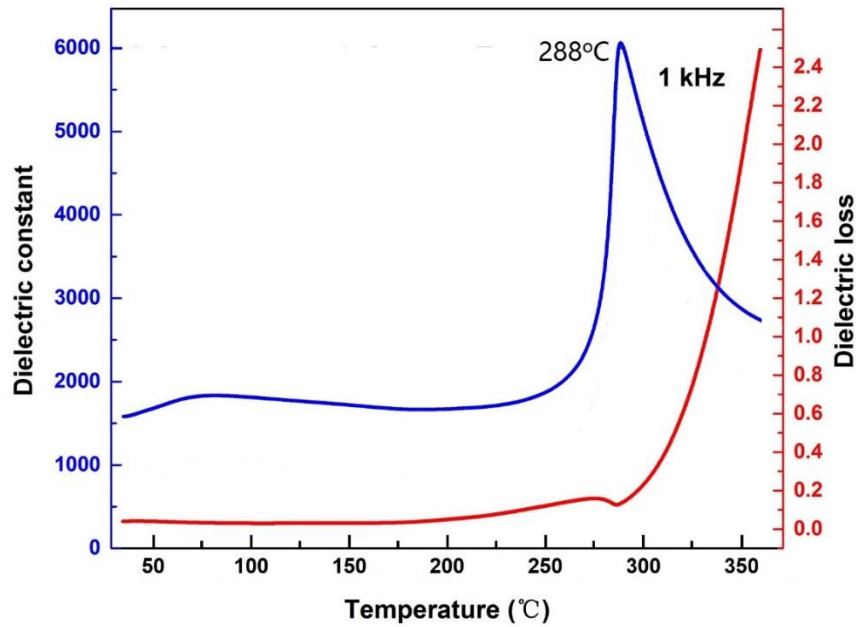
Fig. 6.7 Temperature dependence of dielectric constant and dielectric loss of the oriented (F=49%) KNLN–BZ–BNT ceramics measured at 1 kHz.

The temperature dependences of dielectric constants and dielectric loss at 1 kHz of the oriented (*F*=49%) KNLN−BZ−BNT ceramics are shown in Fig. 6-7. The Curie temperature (T_c) is 288 °C. It has no evident differences compared with non-oriented ceramics mentioned in chapter 3. Other electric properties parameters of oriented KNLN−BZ−BNT and non-oriented ceramics are shown in table 6-2. The d_{33} of oriented ceramics improved 22% compared with non-oriented ceramics. Although the performance has been increased by 22%, there is still much room for improvement by using thinner template particles and optimizing tape-casting process.

Table 6-2 Performance parameters

	ρ (g/cm^3)	ε_r	Tanδ (%)	k_p (%)	T_c (°C)	d_{33} (pC/N)
Oriented (49%)	4.48	1540	3.2	-	288	347
Non-oriented	4.37	1600	3.5	42	279	285

6.4 Summary

In this chapter, firstly, the slurry formulations suitable for KNLN–BZ–BNT ceramics was studied, and high quality tape-casting thick films were obtained. The process of the preparation of oriented ceramics was optimized. Secondly, the oriented KNLN–BZ–BNT ceramics with an orientation of 49% were fabricated. The d_{33} of oriented ceramics improved 22% compared with non-oriented ceramics. In the end, the principle of orient development process was investigated and it can be divided into 3 stages: (1) ceramics densification followed with in situ reaction between template particles and matrix particles; (2) rapid growth of individual oriented grain; (3) slow growth of oriented grain. The results showed that the oriented grain growth follows the principle of 2-D nucleation and growth.

Reference

[1] Gao, F., Hong, R. Z., Liu, J. J., Yao, Y. H., & Tian, C. S. Grain growth kinetics of oriented $0.92Na_{0.5}Bi_{0.5}TiO_3$-$0.08BaTiO_3$ ceramics by tape casting with $Bi_{2.5}Na_{3.5}Nb_5O_{18}$ templates, J. Electroceram, 24, 145-152, 2010.

[2] N. Koga, J. Sestak, Kinetic modeling of advanced inorganic glassceramics formation by crystal growth from pre-existing nuclei, J. Therm. Anal. Calorim. 60, 667-674, 2000.

[3] H. Yilmaz, T.M. Susan, L.M. Gary, (Reactive) Templated grain growth of oriented sodium bismuth titanate ($Na_{1/2}Bi_{1/2}TiO_3$-$BaTiO_3$) ceramics—II dielectric and piezoelectric properties, J. Electroceram. 11, 217-226, 2003.

[4] K.H. Brosnan, S.F. Poterala, R.J. Meyer, S. Misture, G.L. Messing, Templated grain growth of <001> oriented PMN-28PT using SrTiO3 templates, J. Am. Ceram. Soc. 92, S133, 2009.

[5] T. Richter, S. Denneler, C. Schuh, Oriented PMN–PT and PMN–PZT, J. Am. Ceram. Soc. 91, 929, 2008.

[6] G.L. Messing, S. Trolier-McKinstry, E.M. Sabolsky. Templated grain growth of oriented piezoelectric ceramics, Crit. Rev. Solid State Mater. Sci. 29, 45, 2004.

[7] T. Tani. Crystalline-oriented piezoelectric bulk ceramics with a perovskite-type structure. Journal of the Korean Physical Society. 32, S1217-S1220, 1998.

[8] T. Sugawara, Y. Nomura, T. Kimura, T. Tani. Fabrication of (111) oriented $BaTiO_3$ bulk ceramic by reactive templated grain growth method. Journal of the Ceramic Society of Japan. 109, 897-900, 2001.

[9] F. Gao, C.S. Zhang, X.C. Liu, L.H. Cheng, C.S. Tian, Microstructure and piezoelectric properties of oriented $(Na_{0.84}K_{0.16})_{0.5}Bi_{0.5}TiO_3$ lead-free ceramics, J. Eur. Ceram. Soc. 27, 3453, 2007.

[10] J. E. Burke. Role of Grain Boundaries in Sintering. Journal of the American Ceramic Society, 40, 80-85, 1957.

[11] S. H. Hong, G. L. Messing. Anisotropic grain growth in diphasic-gel-derived titania-doped mullite. Journal of the American Ceramic Society. 81, 1269-1277, 1998.

[12] H. Takao, Y. Saito, Y. Aoki, K. Horibuchi. Microstructural evolution of crystalline-oriented $(K_{0.5}Na_{0.5})NbO_3$ piezoelectric ceramics with a sintering aid of CuO. Journal of

the American Ceramic Society. 89, 1951-1956, 2006.

[13] G. Tutuncu, Y. Chang, S. Poterala, G. L. Messing, J. L. Jones. In situ observations of templated grain growth in $(Na_{0.5}K_{0.5})_{0.98}Li_{0.02}NbO_3$ Piezoceramics: texture development and template-matrix interactions. Journal of the American Ceramic Society. 95, 2653-2659, 2012.

Chapter 7

Conclusion

With the improvement of healthy and environmental protection requirements, the development of lead-free piezoelectric ceramics has become a requirement. In our research, KNN-based ceramics were studied as the most promising substitute for lead-based ceramics due to the high piezoelectric coefficient and high Curie temperature.

To improve the temperature-stability of KNN-based ceramic. Rhombohedral perovskite component BNT was employed as the third component to adjust the MPB slope of BZ–KNN system. MPB slope of KNLN–BZ system was adjusted from negative to positive by adding a small amount of the third component, BNT. A vertical MPB was formed when the addition amount of BNT was 1%. The vertical MPB composition, 0.075BZ–0.915KNLN–0.01BNT, with temperature-independent behavior has important practical value. The research method, using a stable rhombohedral perovskite component to adjust the negative MPB slope, indicates the possibility that the positive slope of MPBs could be made perpendicular to the composition axis by adding a stable tetragonal perovskite component as the third component in lead-free piezoceramic systems. The method provides a route for improving the performance with temperature stability of lead-free piezoceramics.

In the synthesis of template particles by hydrothermal method, $NaNbO_3$ particles with different morphology were synthesized. Plate-like morphology particles with a width of 35 µm and a thickness of 3 µm and fibrous morphology particles with an aspect ratio were obtained as expected morphology. Through investigating the hydrothermal conditions such as reaction time, temperature and NaOH concentration on the phase and morphology of the particles, process of crystal growth was conjectured. The plate-like NN particles were grown form the strip-like $Na_8Nb_6O_{19} \cdot 13H_2O$ through dehydration and rearrangement with the increase of temperature. The optimal hydrothermal conditions for preparing plate-like morphology were confirmed as 140 ºC, 3 h and 12 mol/L of NaOH. Fibers NN particles with an aspect ratio could be

obtained with further increase of temperature to 180 °C. After annealing treatment at 600 °C, the plate-like NN and fiber NN both turned in to perovskite structure without morphology change. However, the melting point of the plate-like particles confirmed by TG-DTA analysis was around 1000 °C, therefore the particles could only be used in low temperature sintering below 1000 °C.

To improve the application temperature of template particles, hexagonal $NaNbO_3$ particles with plate-like morphology were synthesized by hydrothermal method. Hydrothermal conditions such as reaction time, temperature, mineralizer concentration, surfactant, $K^+:Na^+$ ratio were discussed. Particles with plate-like morphology could be obtained in a $K^+:Na^+$ ratio of 1:1 to 3:1. The mineralizer concentration in the hydrothermal reaction was able to control the particle morphology. Plate-like particles with a diameter of 10–60 μm and a thickness of 1–10 μm were obtained at mineralizer concentrations between 0.7–1.4 M. This ilmenite type structure $NaNbO_3$ could completely transform into perovskite structure by annealing treatment at 600 °C. The irreversible phase transition process was confirmed as atomic compact. The atomic compact during phase transformation caused some lattice defect, and further resulted in the change of surface orientation. The thickness of the particles was positively correlated with the disorientation of the top surface. More defects accumulated in the thickness direction as the particles became thicker, and the surface orientation changed from ordered to completely disordered. These results indicate that thinner particles tend to have higher orientation in the (00l) crystal planes.

In the fabrication of oriented KNLN–BZ–BNT ceramics by tape-casting method, slurry formulations suitable for this system was studied, and high quality tape-casting thick films were obtained. The process of the preparation of oriented ceramics was optimized. On this basis, oriented KNLN–BZ–BNT ceramics with an orientation of 49% were fabricated. The d_{33} of oriented ceramics improved 22% compared with non-oriented ceramics. The principle of orient development process was also investigated and it can be divided into 3 stages: (1) ceramics densification followed with in situ reaction between template particles and matrix particles; (2) rapid growth of individual oriented grain; (3) slow growth of oriented grain. The results showed that the oriented

grain growth follows the principle of 2-D nucleation and growth.

Acknowledgements

First of all, I would like to express my gratitude to all those who helped me during the writing of this thesis. I gratefully acknowledge the help of my supervisor, Professor Tomoaki Karaki, who has offered me valuable suggestions in the academic studies. In the preparation of this thesis, he has spent much time reading through each draft and provided me with inspiring advice. Without his patient instruction, insightful criticism and expert guidance, the completion of this thesis would not have been possible.

Second, I also owe a special debt of gratitude to Professor Toshihiro Matsuda, Professor Kazuhide Kamiya, Professor Tadashi Fukuhara, and Dr. Yuichi Sakai for their serious review and sincere suggestions in my thesis. I aslo gratefully acknowledge Professor Tadashi Fujii for his continuous support in my study. I am also greatly indebted to Dr. Shan bai, Dr. Liqiang Liu, as well as other members of the laboratory, who have instructed and helped me a lot during the doctoral research.

Last, I should finally like to express my gratitude to my beloved parents who have always been helping me out of difficulties and supporting without a word of complaint.

List of Publications

Yao Lu, Tomoaki Karaki and Tadashi Fujii, Preparation of Morphology-Controlled Plate-Like Sodium Niobate Particles by Hydrothermal Synthesis. **J. Am. Ceram. Soc., 98**, 1668-1672, 2015.

Yao Lu, Tomoaki Karaki and Tadashi Fujii, Hydrothermal Synthesis of Plate-like Sodium Niobate Particles. **Ceramics International, 41**, S174-S179, 2015.

Yao Lu, Tomoaki Karaki, Tadashi Fujii, Yoshiaki Ido, Yongxiang Li, and Yuichi Sakai, Morphology Control and Phase Transition of Hexagonal Sodium Niobate Particles, **Ceramics International**, doi.org/10.1016/j.ceramint.2017.04.060.

Shan Bai, **Yao Lu**, Tomoaki Karaki, Preparation of Plate-Like Sodium Niobate Particles by Hydrothermal Method, **J. Am. Ceram. Soc., 98**, 654-658, 2015.